Master thesis and internship[BR]- Master's thesis : Infrared thermography and theoretical methods for hypersonic aerodynamic heating predictions[BR]- Integration internship

Auteur : Joisten, Sophie
Promoteur(s) : Terrapon, Vincent
Faculté : Faculté des Sciences appliquées
Diplôme : Master en ingénieur civil en aérospatiale, à finalité spécialisée en "aerospace engineering"
Année académique : 2020-2021
URI/URL : http://hdl.handle.net/2268.2/11561

University of Liège
Faculty of Applied Sciences

von Karman Institute for Fluid Dynamics
Aeronautics & Aerospace Department

Academic year 2020-2021

Infrared thermography and theoretical methods for hypersonic aerodynamic heating predictions

Master thesis presented in partial fulfillment of the requirements for the degree of Master in Aerospace Engineering

Sophie Joisten

Supervisor: Dr. G. Grossir
Promoter: Prof. V.E. Terrapon
Jury members: Prof. G. Dimitriadis & Prof. K. Hillewaert

Abstract

Aerodynamic heating is one of the most critical problems encountered by vehicles flying at hypersonic speeds. Tools to predict these extreme wall heating rates with different levels of fidelity are required at each stage of the design process. This Master thesis presents a methodology for the prediction of heating rates over two-dimensional and axisymmetric geometries through theoretical correlations and experimental measurements, complemented with numerical simulations.

A literature review is conducted which uncovers useful and rapid approximate methods for the prediction of both stagnation-point and off-stagnation-point surface heat fluxes. The predictions rely on the integration of estimated boundary-layer edge properties along wall streamlines. These engineering formulations are gathered in a MATLAB code that yields results in good accordance with higher-fidelity data for the centerline heating. The approach can potentially be extended to more arbitrary three-dimensional configurations.

Numerical modeling is also handled for the two-dimensional perfect-gas Navier–Stokes calculations over a hemispherical cylinder and a blunt cone at Mach 6. The engineering predictions for the stagnation-point heating compare well with numerical results. Computed heat fluxes along the body surface serve as validation for the theoretical methods.

Emphasis is mostly placed on the preparation of an experimental setup for the application of infrared thermography as a powerful thermal sensor in short-duration facilities. A new high-resolution infrared camera carefully calibrated is employed for measurements in the H3 Mach 6 blow-down facility of the von Karman Institute for Fluid Dynamics. The heat-transfer rebuilding procedure based on one-dimensional conduction in a semi-infinite solid is presented and applied.

Measurements are then carried out on a 7.4°-half-angle cone model at zero angle of attack and different free-stream unit Reynolds numbers. The observed laminar heating rates increase with Reynolds number. The centerline heat-flux magnitudes are in good agreement with numerical and theoretical results, but the measured profiles follow a different trend along the body surface. A more complete experimental study is required to examine the potential practical causes for these mismatches. The present experimental approach is validated and can be used for future infrared heat-transfer studies in hypersonic facilities. Several recommendations are finally issued for further improvements of the experimental method.

Résumé

L'échauffement aérodynamique est un des problèmes les plus critiques rencontrés par les véhicules volant à des vitesses hypersoniques. Des outils permettant de prédire ces extrêmes taux de transfert de chaleur à la paroi avec différents niveaux de fidélité sont nécessaires à chaque étape du processus de conception. Cette thèse de Master présente une méthodologie pour estimer les taux de transfert de chaleur sur des géométries bidimensionnelles et axisymétriques à l'aide de méthodes théoriques et de mesures expérimentales, le tout complété par des simulations numériques.

Une revue bibliographique est menée et permet de découvrir des méthodes approximatives utiles et rapides pour la prédiction des flux de chaleur au point de stagnation et le long de la surface du corps. Les prédictions reposent sur l'intégration des propriétés estimées en bordure de couche limite le long des lignes de courant à la paroi. Ces formulations théoriques simplifiées sont rassemblées et implémentées dans un code MATLAB qui fournit des résultats en accord avec des données haute fidélité pour l'échauffement le long de la ligne centrale. Ces méthodes pourront potentiellement être appliquées à des géométries arbitraires plus complexes.

Une modélisation numérique est également mise en place en vue d'effectuer des calculs Navier–Stokes bidimensionnels avec un modèle de gaz parfait sur un cylindre hémisphérique et un cône émoussé à Mach 6. Les prédictions théoriques pour le flux de chaleur au point de stagnation correspondent aux résultats numériques. Les flux de chaleur calculés numériquement le long de la surface du corps servent à valider les méthodes théoriques.

L'accent est mis sur la préparation d'un dispositif expérimental pour l'application de la thermographie infrarouge en tant que capteur thermique à exploiter dans les installations hypersoniques à courte durée de test. Une nouvelle caméra infrarouge à haute résolution soigneusement calibrée est utilisée pour des mesures dans la soufflerie H3 Mach 6 de l'Institut von Karman pour la Dynamique des Fluides. La procédure de reconstruction du transfert de chaleur basée sur un modèle de conduction unidimensionnelle dans un solide semi-infini est présentée et appliquée.

Des mesures sont alors effectuées sur un modèle conique de demi-angle d'ouverture de 7.4°, à angle d'attaque nul et à différents nombres de Reynolds unitaires. Les taux de transfert de chaleur laminaires observés augmentent avec le nombre de Reynolds. Les amplitudes du flux de chaleur sur la ligne centrale s'accordent avec les résultats numériques et théoriques, mais les profils mesurés suivent une tendance différente le long du corps. Une étude expérimentale plus poussée est nécessaire pour examiner les causes pratiques potentielles de ces désaccords. La présente approche expérimentale est validée et peut être utilisée dans de futures études de transfert de chaleur exploitant la thermographie infrarouge dans les souffleries hypersoniques. Plusieurs recommandations sont enfin émises afin d'améliorer davantage la procédure expérimentale.

Acknowledgments

First of all, I would like to express my sincere gratitude to Dr. G. Grossir, my supervisor at VKI, for his daily support and his great patience. Despite the partial remote work and the technical problem of the wind tunnel, I have been very well supervised throughout the internship and the writing of this thesis. His open-mindedness and his willingness to do things properly and thoroughly have really motivated me to give my best for this project.

I would like to thank my promoter in Liège, Prof. V.E. Terrapon, for his support, his useful advice and his availability whenever I had a question or a doubt. Prof. K. Hillewaert also deserves my thanks for giving me the opportunity to do my internship at VKI.

I am grateful to several VKI members such as the technical team of the H3 facility and Prof. O. Chazot. I have really enjoyed the atmosphere at VKI during my short stay. I also thank the other students and trainees newly met for their encouragements and the good times we spend together.

Finally, I want to thank my friends for their kind support throughout our studies and my family for always believing in me.

Contents

Nomenclature

Roman symbols

a	m/s	Speed of sound
c	$\mathrm{J/(kg \cdot K)}$	Specific heat
c_p	$\mathrm{J/(kg \cdot K)}$	Specific heat at constant pressure
c_v	$\mathrm{J/(kg \cdot K)}$	Specific heat at constant volume
C		Constant in generalized heating equation
C	–	Chapman–Rubesin factor
C_1	$\mathrm{W \cdot m^2}$	First universal radiation constant
C_2	$\mathrm{m \cdot K}$	Second universal radiation constant
e	J/kg	Specific internal energy
E	$\mathrm{W/m^2}$	Emissive power
G	$\mathrm{W/m^2}$	Irradiation
h	J/kg	Specific enthalpy
h_D	J/kg	Dissociation enthalpy
i	–	Iteration index
I	–	Infrared camera intensity signal
k	–	Exponent set to 0 for planar bodies and 1 for bodies of revolution
k	$\mathrm{W/(m \cdot K)}$	Thermal conductivity
K	$\mathrm{kg^{1/2}/m}$	Heat-transfer coefficient in Sutton–Graves equation
L	m	Characteristic length
L_t	m	Total model length
m		Exponent on velocity in generalized heating equation
n		Exponent on density in generalized heating equation
n	–	Iteration index
N	–	Transition-onset N-factor
N	–	Number of cells in numerical computations
p	Pa	Pressure
$\dot{q}$	$\mathrm{W/m^2}$	Heat flux
r	–	Recovery factor
r		Test result in uncertainty analysis
r_b	m	Radius of cross section of body of revolution
R	$\mathrm{J/(kg \cdot K)}$	Specific gas constant
R_f	–	Reynolds analogy factor

R_n	m	Nose radius
R^2	–	Coefficient of determination to evaluate goodness of fit
s	m	Distance along body surface measured from stagnation point of blunt body or from leading edge of flat plate and sharp cone
s'	m	Distance along body surface measured from theoretical sharp tip of blunt cone
S	K	Constant used in Sutherland's law
t	s	Time
T	K	Temperature
u	m/s	Streamwise velocity
x, y, z	m	Streamwise, wall-normal and spanwise Cartesian coordinates
X		Measured variable in uncertainty analysis
X	m	Transformed distance used by Crabtree at al.
y^+	–	Non-dimensional wall distance

Greek symbols

α	–	Absorptivity coefficient
α	$\mathrm{m^2/s}$	Thermal diffusivity
γ	–	Specific heat ratio
Δ	m	Shock stand-off distance
Δ_{FR}	%	Error of stagnation-point heat flux with respect to Fay–Riddell prediction
Δx	m	Cell size in numerical computations
ε	–	Emissivity coefficient
η, ξ		Similarity variables, wall-normal and body-tangent coordinates
θ	°	Angle between flight direction and radius vector from center of curvature of the nose of a blunt body
θ	°	Viewing angle in infrared thermography
θ	m	Boundary-layer momentum thickness
θ_c	°	Cone half-angle
λ	m	Wavelength
μ	°	Mach angle
μ	$\mathrm{kg/(m \cdot s)}$	Dynamic viscosity
ρ	–	Reflectivity coefficient
ρ	$\mathrm{kg/m^3}$	Density
σ		Standard deviation
σ	$\mathrm{W/(m^2 \cdot K^4)}$	Stefan–Boltzmann constant
τ	–	Transmissivity coefficient
χ		Variable used in Sutherland's law, either viscosity or thermal conductivity
ω	$\mathrm{kg \cdot s/m^3}$	Ratio of viscosity to gas constant and temperature used by Lees

Non-dimensional numbers

C_f	Skin-friction coefficient
C_p	Pressure coefficient
Le	Lewis number
M	Mach number
Pr	Prandtl number
Re	Reynolds number
St	Stanton number

Subscripts

abs	Absorbed
atm	Refers to the atmosphere
aw	Adiabatic wall
e	At the edge of the boundary layer
obj	Refers to the object
ref	At reference condition
ref	Reflected
s	Stagnation condition at the edge of the boundary layer
SP	At the stagnation point
sur	Refers to the surroundings
t	Stagnation / total condition
tr	Refers to the boundary-layer transition
tr	Transmitted
w	Refers to the (germanium) window
w	At the wall
λ	Denotes a spectral dependence
0	At time instant $t = 0$
0	Stagnation condition in the reservoir
1	Condition upstream of a normal shock
2	Condition downstream of a normal shock
∞	Free-stream quantity

Superscripts

b	Refers to a black body
$*$	Condition determined by reference enthalpy

Acronyms and abbreviations

ANTARES	Application of Newonian Theory for ARbitrary Entry Shapes
BC	Boundary Conditions
CBAERO	Configuration Based Aerodynamics
CFD	Computational Fluid Dynamics
CFL	Courant–Friedrichs–Lewy
IR	Infrared
IRDA	InfraRed thermography Data Analysis
MNT	Modified Newtonian Theory
TC	Thermocouple
TM	(Mercury) Thermometer
TM	Taylor–Maccoll
TVD	Total Variation Diminushing
VKI	von Karman Institute for Fluid Dynamics

1. Introduction

1.1. Framework

Hypersonic aerodynamics has driven growing interest since the 1950s with the advent of atmospheric entry vehicles. The numerous hypersonic projects developed over the past decades have resulted in great achievements, but have also revealed the hypersonic environment to be harsh and non-forgiving. Hypersonic flight represents a serious technological and economical challenge at the heart of the 21st century (Bertin and Cummings, 2003).

The hypersonic flow regime is commonly defined as the realm of speeds exceeding Mach 5:

$$\mathrm{M}_\infty = \frac{u_\infty}{a_\infty} > 5, \tag{1.1}$$

where M_∞ is the free-stream Mach number, u_∞ and a_∞ are respectively the free-stream velocity and speed of sound. The basic assumption is thus that the kinetic energy of the free stream is large compared to the internal thermal energy of the free-stream fluid particles. As pointed by Anderson (2006), this theoretical limit of 5 is just a convention and hypersonics is best defined as the regime which embodies several physical gas dynamics and high-temperature flow phenomena that become more and more important as the Mach number increases. The physics associated with hypersonic flows is very different from that of low-speed flows, but also supersonic flows, which makes hypersonics an important and interesting topic of research.

The flow around a hypersonic vehicle experiences a strong density and pressure increase through a shock wave. The high-density flow field behind the shock is condensed into a thin volume called a shock layer. As the Mach number increases, so does the density rise and the shock is pulled closer to the body, creating a thin shock layer, characteristic of hypersonic flows. As a consequence, the Mach cone (defined by the Mach angle $\sin\mu_\infty = 1/\mathrm{M}_\infty$) is very slender compared to the supersonic case.

In the nose region, the shock wave is strongest and nearly normal just in front of the stagnation point, while it curves further downstream and becomes weaker. The entropy increase being proportional to the shock strength, large entropy gradients are created and an entropy layer wets the body for large distances from the nose. This entropy layer can interact with the growing boundary layer developing along the surface in a phenomenon called vorticity interaction.

The main characteristic of the hypersonic regime is certainly the high dissipation of kinetic energy of the flow as it is slowed down by viscous effects in the boundary layer. Part of the large kinetic energy is transformed into thermal energy, leading to very high temperatures. If high enough, they may cause gas-molecules dissociation and even ionization. Since viscosity increases with temperature, the hot boundary layer is thicker and may greatly affect the outer inviscid flow, whose changes in turn feed back to affect the growth of the boundary layer. This mechanism is called viscous interaction. The shock layer is also a region of high temperatures, as the flow loses its kinetic energy by passing through the strong shock wave. For a hypersonic re-entry vehicle such as the Space Shuttle, shock-layer temperatures exceeding 6,000 K are encountered.

1.2. Motivation

By far, the most critical consequence of high temperatures in hypersonics is the extreme heat-transfer rates to the body surface. This *aerodynamic heating* directly arises from the hot gas in the flow field around the body (in the boundary layer and the shock layer) transferring part of its heat energy to the body. At moderate speeds and temperatures (usually below 10,000 K), convection is the primary means by which this heat transfer occurs and the convective heating is denoted $\dot{q}_c$.

From Bertin (1994), the stagnation-point convective heat transfer is roughly proportional to

$$\dot{q}_c \propto \rho_\infty^{0.5} u_\infty^3 R_n^{-0.5}, \tag{1.2}$$

where R_n is the nose radius and ρ_∞ is the free-stream density. The cubic dependence on the velocity emphasizes how aerodynamic heating is dominant at hypersonic speeds. The aerodynamic drag, following the classical u_∞^2 dependence, usually becomes a less critical consideration. The design of hypersonic machinery is driven by the need to reduce this heat transfer to the body. From Eq. 1.2, it is clear that all hypersonic-flying objects, such as a space vehicle making entry through a dense atmosphere, must be blunt-nosed to some extent (Allen and Eggers, 1953). As R_n increases, most of the heat energy in the gas is convected into the vehicle wake rather than transported to the surface. Besides, thermal protection systems are often necessary to shield the aerospace vehicle from the massive heat accumulation during atmospheric entry. Their design is one of the most critical steps of the overall space vehicle design, as the choice of their type, size and weight results from a complex optimization between many physical and economical restrictions, of which aerodynamic heating (Asma et al., 2008).

These considerations motivate the need to study and quantify such aerothermodynamic phenomena. The accurate characterization and prediction of the severe heating environment encountered by high-speed vehicles is the prerequisite for the successful and safe development of any hypersonic mission. The different predictive tools can be classified into numerical methods, experimental methods and theoretical methods. Each approach has its advantages and drawbacks, which eventually reflect the traditional trade-off between cost and accuracy. They can all bring valuable results for a specific and different stage of the design process. Significant efforts are still ongoing in the aerothermodynamic community to develop and enhance such heat-flux predictive tools, with, for instance, the works of Brandis and Johnston (2014) for theoretical methods, Knight et al. (2017) for numerical capabilities and Juliano et al. (2019) for wind-tunnel experiments.

1.3. Objectives and structure

The present work aims to develop a methodology for the prediction of convective heating on arbitrary axisymmetric and two-dimensional geometries, relying on a comparative approach combining experimental measurements, theoretical methods and numerical simulations.

The theoretical tools are first investigated in Chapter 2. This part is aimed to perform a broad literature review of the different theories that have been developed to provide simple approximate correlations for heat-flux estimations. The purpose is to work out how and to what

extent they can be implemented in the context of this study to provide efficient aerodynamic heating predictions. It is desired to remain very general so that both slender- and blunt-bodies heating rates are examined, for both laminar and turbulent boundary-layer cases.

Numerical simulations, handled in Chapter 3, are the second means of obtaining heat-flux estimations. The flows around two canonical blunt bodies exhibiting laminar boundary layers are considered. In this study, solutions of the Navier-Stokes equations are mainly used as a complementary tool to support the experimental investigation and to validate the lower-fidelity approximate results of the first part.

Thirdly, what was supposed to be the main part of this thesis is the application of infrared thermography for quantitative heat-transfer measurements to be carried out in the H3 Mach 6 facility of the von Karman Institute for Fluid Dynamics (VKI). Unfortunately, a defective electrical valve made the wind tunnel inoperative after the single wind-tunnel testing sequence we could carry out. We were thus neither able to obtain the desired numerous results for various geometries and Reynolds numbers, nor to perform some flow visualizations using the schlieren optical system. The objectives of this work thus had to be slightly reformulated to account for this unexpected and regrettable incident. Rather than focusing on the ability of the infrared (IR) technique to accurately predict heating rates, Chapter 4 aims to present the methodology adopted to prepare a robust and reliable experimental setup to apply the IR technique in hypersonic facilities.

Finally, in Chapter 5, the results from the theoretical, numerical and experimental predictive methods are confronted to each other and discussed. The few experimental data obtained are exploited to validate the experimental approach developed and the uncertainty on the final results is assessed.

2. Theoretical background

In the preliminary design of hypersonic vehicles, it is required to calculate aerodynamic heating rates of simplified configurations efficiently and with reasonable accuracy. Experimental testing and numerical simulations appear unsuitable for this purpose because of their prohibitive cost. This need for rapid and reliable initial estimates has led to the development of what will be termed in this work theoretical or engineering or approximate methods. Such formulations are based on the actual flow physics and make several approximations to the true theory in order to achieve simple closed-form solutions.

The aim of this chapter is to perform a broad literature review of the theoretical tools available to study aerodynamic heating over axisymmetric geometries at zero incidence. The first section stands as a general introduction to define important concepts relevant to the analysis. Then, approximate methods derived for laminar boundary layers are presented. A brief discussion of the complex boundary-layer transition problem follows. The fourth section then handles turbulent heating rates. Lastly, a more advanced engineering-level tool is presented.

The approximate correlations have been implemented in a MATLAB code (MathWorks, Inc., 2021) for the purposes of this work. Throughout the sections, the implementations and the hypotheses made are briefly presented along with validations against higher-fidelity data.

2.1. Introduction and definitions

Chapter 1 emphasized the crucial role of heat transfer in hypersonic viscous flows. The present study does not address the problem of radiative heating because of the low hypersonic regime and, thus, the low temperature range considered. The focus is put on *convective aerodynamic heating*, termed $\dot{q}_w$ from now on to denote the local heat-transfer rates to the wall, expressed in $\mathrm{W/m^2}$. Although the term convection is used, it is thermal conduction that takes place when a temperature gradient in the gas at the wall $\left(\frac{\partial T}{\partial y}\right)_w$ exists. From Fourier's law,

$$\dot{q}_w = -k_w \left(\frac{\partial T}{\partial y}\right)_w, \tag{2.1}$$

where k_w is the thermal conductivity of the gas at the wall.

The Stanton number St is a key dimensionless number defined as ratio of the heat transferred by convection to the thermal capacity of the fluid flow. It is thus a measure of the actual heat flow to the body over the maximum possible heat flow, as expressed by

$$\mathrm{St} = \frac{\dot{q}_w}{\rho_e u_e (h_{aw} - h_w)}, \tag{2.2}$$

where h_{aw} is the recovery or adiabatic-wall enthalpy, i.e., the enthalpy at the wall when the local

heat transfer to the wall is zero. The subscripts e and w respectively denote flow properties evaluated at the edge of the boundary layer and at the wall. Eq. 2.2 highlights that the driving potential for aerodynamic heating is the enthalpy difference $(h_{aw} - h_w)$. The adiabatic-wall enthalpy is generally expressed in terms of the recovery factor r,

$$h_{aw} = h_e + r\frac{u_e^2}{2}, \qquad \text{with} \quad r = \frac{h_{aw} - h_e}{h_0 - h_e}, \tag{2.3}$$

where h_0 is the total enthalpy at the outer edge of the boundary layer. The recovery factor depends only weakly on flow conditions so that the following approximations are typically used (Koppenwallner, 1984):

$$\begin{aligned} r &= \mathrm{Pr}^{1/2} \quad \text{for laminar flow,} \\ r &= \mathrm{Pr}^{1/3} \quad \text{for turbulent flow,} \end{aligned} \tag{2.4}$$

where Pr, the Prandtl number, is defined in terms of c_p the specific heat capacity at constant pressure, μ the dynamic viscosity and k the thermal conductivity, as

$$\mathrm{Pr} = \frac{c_p \mu}{k}. \tag{2.5}$$

For most gases, it is reasonable to regard the Prandtl number as constant and to use $\mathrm{Pr} = 0.71$ for air (White, 2006, Lees, 1956).

Throughout this work, considering the operating conditions of the VKI H3 wind tunnel (see Chapter 4), the assumption of a thermally and calorically perfect gas is posed (Santarelli and Charbonnier, 1999). Its validity is insured by the moderate temperature and pressure involved (no dense-gas effects, no vibrational excitation). Thus, the enthalpy and internal energy respectively write $h = c_p T$ and $e = c_v T$, with constant specific heat capacities. The values $\gamma = \frac{c_p}{c_v} = 1.4$ and $R = 287$ J/(kg $\cdot$ K) are used for dry air. All high-temperature chemical effects (e.g., dissociation, ionization) can be conveniently neglected. Energy transport by diffusion (due to atomic recombination) is neglected and convective heating consists only of conduction.

Lastly, considering viscous flows, an essential non-dimensional parameter to define is the Reynolds number, ratio of inertia to viscous forces,

$$\mathrm{Re}_{L,\infty} = \frac{\rho_\infty u_\infty L}{\mu_\infty}, \tag{2.6}$$

based here on a characteristic length L and free-stream properties. Alternatives definitions of Re make use of boundary-layer edge flow properties and/or other reference lengths (e.g., a unitary length for the unit Reynolds number $\mathrm{Re}_{\mathrm{unit},\infty}$).

2.2. Laminar heat transfer

The objective of this section is to provide useful engineering formulations for the laminar boundary-layer heating of surfaces, without going into the details of the derivations. The theories presented found their basis in the compressible boundary-layer equations, recalled in Appendix A. In addition to the references specific to each theory, this research heavily relied on the detailed reviews of Hoshizaki et al. (1975), DeJarnette et al. (1987) and Tauber (1989).

2.2.1. Stagnation-point heating

The stagnation region of blunt-nosed hypersonic vehicles is of great practical and theoretical interest. On the one hand, the stagnation point is where the maximum heat rates are expected to occur. On the other hand, it is the first particular case for which the laminar boundary layer can be treated as self-similar. The governing boundary-layer equations, which are partial differential equations, can be reduced to a set of ordinary differential equations amenable for analytical treatment (see Appendix A for elementary derivations and the concept of self-similarity).

In 1958, Fay and Riddell developed a pioneer engineering theory for high-speed convective aerodynamic heating, based on the boundary-layer equations and similarity transformations. It relies on the following assumptions:

- the flow is uniform, laminar and there is no free-stream turbulence;
- the Reynolds number is sufficiently large so that the stagnation-point boundary-layer thickness is much less than the shock-detachment distance and has no influence on the pressure distribution;
- all the hypersonic incoming flow has passed through a normal shock wave;
- the flow at the edge of the boundary layer is in local thermodynamic and chemical equilibrium;
- the gas is a mixture of perfect gases;
- the wall can be catalytic and the chemical reactions in the boundary layer can be in equilibrium, non-equilibrium or frozen.

The equation of Fay and Riddell (1958) for the stagnation-point heat transfer in the case of an equilibrium boundary layer reads

$$(\dot{q}_w)_{\mathrm{SP}} = 0.763\,\mathrm{Pr}^{-0.6}\,(\rho_w\mu_w)^{0.1}\,(\rho_s\mu_s)^{0.4}\left[1+\left(\mathrm{Le}^{0.52}-1\right)\left(\frac{h_D}{h_s}\right)\right](h_s-h_w)\sqrt{\left(\frac{\mathrm{d}u}{\mathrm{d}s}\right)_s} \tag{2.7}$$

where the subscript s denotes stagnation conditions at the edge of the boundary layer, while the coordinate s is measured along the body surface with $s = 0$ at the stagnation point. In the square brackets, h_D is the dissociation enthalpy and Le is the Lewis number, ratio of thermal diffusivity to mass diffusivity. The dynamic viscosity μ is obtained from Sutherland's law. Inspecting Eq. 2.7, external flow properties (s) are more important than the wall values (w) and contribute to about 40% of the final uncertainty on the predicted heat transfer, as stated by the authors. Although experimental results have shown up to 20% deviations from the predictions, the Fay–Riddell equation is a widely-used reference in the field of aerodynamic heating and is deemed sufficiently accurate for engineering purposes.

Eq. 2.7 strongly depends on the tangential velocity gradient $(\mathrm{d}u/\mathrm{d}s)_s$. Different options exist for its estimation, depending on the assumptions made (Olivier, 1993, Boison and Curtiss, 1959). The most famous one, originally used by Fay and Riddell (1958), makes use of a pressure distribution from the Modified Newtonian Theory (MNT, discussed shortly later in § 2.2.3) and

Euler's equation applied at the boundary-layer edge, to yield

$$\left(\frac{\mathrm{d}u}{\mathrm{d}s}\right)_s = \frac{1}{R_n}\sqrt{\frac{2(p_s - p_\infty)}{\rho_s}}. \tag{2.8}$$

This velocity gradient depends on conditions behind the shock and thus also on the free-stream Mach number, but Eq. 2.8 neglects the influence of the shock stand-off distance Δ as well as high-temperature effects. According to Olivier (1993) and Boison and Curtiss (1959), this equation is a relatively good approximation when used in wind tunnels with perfect-gas conditions and as long as the body bluntness remains limited. For body configurations with high bluntness, using directly the nose radius of curvature R_n in Eq. 2.8 would lead to wrong stagnation-point velocity-gradient estimates, and an effective nose radius should be used instead (Sakraker, 2016).

In this study, all velocity gradients have been approximated using Eq. 2.8 solely. The reader is referred to Ilich et al. (2017) for a detailed summary of all methods available for the determination of the velocity gradient together with the phenomena accounted for.

The Fay–Riddell equation can be further simplified in the scope of this work where experiments are to be carried out in the VKI H3 facility. The stagnation temperatures are too low to cause air-molecules dissociation. There is no chemistry in the flow and the Lewis-number term is thus not relevant. The whole term in brackets can be dropped, reducing Eq. 2.7 to

$$(\dot{q}_w)_{\mathrm{SP}} = 0.763\,\mathrm{Pr}^{-0.6}\,(\rho_w\mu_w)^{0.1}\,(\rho_s\mu_s)^{0.4}\,(h_s - h_w)\sqrt{\left(\frac{\mathrm{d}u}{\mathrm{d}s}\right)_s}. \tag{2.9}$$

Besides, the perfect-gas equation holds in the shock layer so that $\rho_s = \frac{p_{t2}}{RT_{t2}}$, where the subscript $t2$ refers to stagnation condition just downstream of the normal shock.

Numerous correlations for the stagnation-point heat transfer were developed after the leading work of Fay and Riddell (1958). They were all inspired from this same theory, where simplifications have been made to only retain some basic parameters governing heat transfer.

Another commonly used correlation, very similar to that of Fay and Riddell, is due to Cohen (1961) and has proven to yield reliable heating rates:

$$(\dot{q}_w)_{\mathrm{SP}} = 0.767\ \mathrm{Pr}^{-0.6}(\rho_w\mu_w)^{0.07}(\rho_s\mu_s)^{0.43}(h_s - h_w)\sqrt{\left(\frac{\mathrm{d}u}{\mathrm{d}s}\right)_s}. \tag{2.10}$$

Again, Eq. 2.10 requires the evaluation of the stagnation-point tangential velocity gradient.

Later on, Sutton and Graves (1971) investigated the stagnation-point heat transfer to axisymmetric blunt bodies for a mixture of arbitrary gases in chemical equilibrium. Their study was aimed to develop a general relation for $(\dot{q}_w)_{\mathrm{SP}}$ for different atmospheric compositions encountered in planetary entry. They provided the following correlation, valid for pressures ranging from 0.001 to 100 atm and wall temperatures from 300 to 1,111 K:

$$(\dot{q}_w)_{\mathrm{SP}} = K\sqrt{\frac{p_{t2}}{R_n}}\,(h_s - h_w), \tag{2.11}$$

where K is the heat-transfer factor and is a function of the molecular weight, the mass fraction, and a transport parameter of the base gases of the mixture. Some typical values for base gases are given in Table 2.1.

Table 2.1: Typical values of heat-transfer coefficient K (Sutton and Graves, 1971).

Gas composition	K $\left[\text{kg s}^{-1}\ \text{m}^{-3/2}\ \text{atm}^{-1/2}\right]$
N_2	0.1112
O_2	0.1201
H_2	0.0395
air	0.1113

In their study about the flow characterization in the ONERA F4 hot-shot tunnel, Sagnier and Verant (1998) proposed the correlation

$$(\dot{q}_w)_{\text{SP}} = 23.79 \times \left[\frac{h_0 - h_w}{RT_{\text{ref}}}\right]^{1.069} \times \sqrt{\frac{p_{t2}}{R_n}} \quad \text{with } T_{\text{ref}} = 273.15 \text{ K}, \tag{2.12}$$

derived from a set of numerical computations on a hemispherical probe. The formulation was originally developed to determine the reservoir enthalpy h_0 based on heat-flux measurements. The authors assumed a catalytic wall and a perfect-gas flow. The constants in Eq. 2.12 were found using a least-square method. Results have an uncertainty of about ±12%.

Lastly, the simplest and crudest technique for estimating hypersonic aerodynamic heating at the stagnation point relies on the generalized heating equation of the form

$$(\dot{q}_w)_{\text{SP}} = \frac{C}{\sqrt{R_n}} (\rho_\infty)^n (u_\infty)^m \left[1 - \frac{h_w}{h_s}\right]. \tag{2.13}$$

Different empirical values of the parameters C, n, m have been suggested by several authors (Table 2.2).

Table 2.2: Parameters in the generalized heating equation, Eq. 2.13.

Reference	C	n	m
French and Griffin (1991)	$2.53 \cdot 10^{-5}$	0.5	3.25
Chapman (1959)	$1.63 \cdot 10^{-4}$	0.5	3
Tauber et al. (1987)	$1.83 \cdot 10^{-4}$	0.5	3

Implementation and results. The preceding approximate engineering correlations have been implemented in a MATLAB code. Fig. 2.1 shows the results of such an implementation for two different cases. The relative errors of the predictions with respect to the Fay–Riddell results are written on top of each bar. Fig. 2.1(a) has been established for typical H3 wind-tunnel conditions (air, $T_w = 300$ K, $M_\infty = 6$, $T_0 = 500$ K, $p_0 = 20$ bar) and a spherical nose of $R_n = 20$ mm. All theories roughly provide similar heating rates, with the largest error found for the correlation of Sutton and Graves (1971). The CFD results correspond to 2D laminar computations carried out in this study (Chapter 3). For the data presented in Fig. 2.1(b), the

test gas is nitrogen, the nose radius is 10 mm and the free-stream conditions are $p_\infty = 385$ Pa, $T_\infty = 96.4$ K and $u_\infty = 2081$ m/s. Such conditions are representative of another hypersonic facility in VKI, the Longshot wind tunnel (Grossir, 2015). The CFD results were internally provided. The agreement between the different theories is again rather good, with smaller relative errors than for Fig. 2.1(a). Overall, it can be concluded that Fig. 2.1 serves as validation for the stagnation-point heat transfer theories implemented in this work.

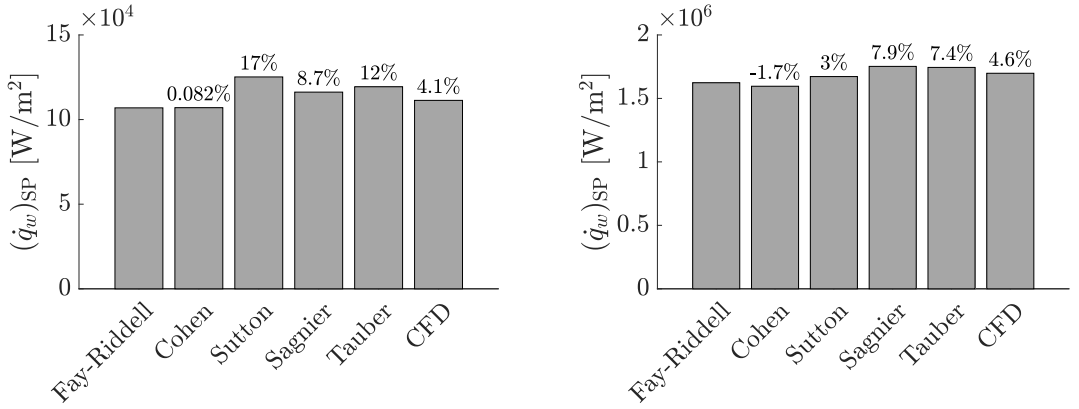

(a) Typical medium-Reynolds-number H3 conditions, $R_n = 20$ mm.

(b) Typical low-Reynolds-number Longshot conditions, $R_n = 10$ mm.

Figure 2.1: Comparison of stagnation-point heat fluxes yielded by engineering correlations and CFD and relative deviations from the Fay–Riddell prediction.

2.2.2. Slender-body heating-rate distribution

Sharp flat plates at angle of attack, wedges and cones constitute the second limiting case where the boundary-layer equations are self-similar. Compressible flows over such sharp-nosed bodies result in attached shock waves at the nose and flows without pressure gradient.

The most widely used approach to compute Stanton-number distributions over flat plates and cones relies on the reference temperature concept (White, 2006, Anderson, 2006). Reference temperature or reference enthalpy methods are approximate engineering methods for estimating skin-friction and heat-transfer coefficients for both laminar and turbulent hypersonic flows. The principle is to use the formulas obtained from the incompressible theory (e.g., the well-known Blasius solution for flat plates) and to evaluate the flow properties at some reference temperature T^* indicative of the temperature inside the boundary layer. In that sense, the incompressible formulas are corrected to account for compressible effects.

The skin-friction coefficient for the laminar compressible boundary layer over a flat plate is given by

$$C_f = \frac{0.664}{\sqrt{\mathrm{Re}_{s,e}}} \sqrt{\frac{T_e \mu^*}{T^* \mu_e}}, \tag{2.14}$$

where one directly recognizes the incompressible result $C_f = 0.664 \cdot \mathrm{Re}_{s,e}^{-1/2}$. The coordinate s is tangential to the body and is measured from the leading edge. The superscript $*$ denotes properties evaluated at the reference temperature. The most famous correlation for T^* is due

to Eckert (1956) and reads

$$T^* = 0.22T_{aw} + 0.28T_e + 0.5T_w, \tag{2.15}$$

with T_{aw} the adiabatic-wall temperature, computed using a recovery factor from Eq. 2.4. Although Eq. 2.15 has an empirical origin, it was shown later that the reference temperature concept is a direct consequence of the similarity relations.

The skin-friction coefficient is then related to the Stanton number through a Reynolds analogy

$$\mathrm{St} = \frac{C_f}{2R_f}, \tag{2.16}$$

where R_f is the Reynolds analogy factor. Numerical solutions for the evolution of R_f as a function of M_∞ are provided in Anderson (2006) and a reasonable approximation for the present hypersonic speeds ($\mathrm{M}_\infty = 6$) is $R_f = \mathrm{Pr}^{2/3}$.

These results for flat plates can be transposed to cones at zero incidence by simply applying the Mangler transform to account for the axisymmetric geometry, so that

$$C_{f,\mathrm{cone}} = \sqrt{3}C_{f,\mathrm{plate}}. \tag{2.17}$$

From Eq. 2.14, it appears that properties at the edge of the boundary layer must be known at each location s to obtain the heat-flux distribution. The classical approach in such heat-transfer problems is to solve the inviscid flow field and use the computed properties on the surface as edge conditions for a viscous solution. To do so, the use of theoretical inviscid solutions is of great interest, such as the Taylor–Maccoll (TM) differential equation for sharp conical bodies at zero incidence (Anderson, 2003). A MATLAB routine solving the equation has been used in the present study.

Implementation and results. The present implementation of Eckert's reference temperature is validated against internal VKI CFD data. The geometry is a 7°-half-angle cone with a 1.75-mm nose radius and is thus not perfectly sharp. The test gas is nitrogen and the conditions are $p_\infty = 276$ Pa, $T_\infty = 88.6$ K and $u_\infty = 1830$ m/s (typical low-Reynolds-number conditions in the Longshot tunnel). The wall temperature is set to $T_w = 300$ K. Boundary-layer edge properties are obtained from a Taylor–Maccoll solution. Results are presented in Fig. 2.2, where s' is the distance along the body surface measured from the theoretical sharp nose tip.

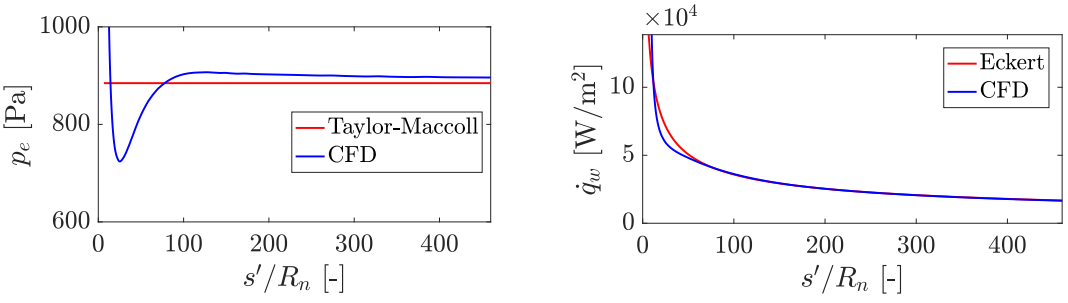

(a) Edge pressure. **(b)** Wall heat flux.

Figure 2.2: Comparison of pressure and heat flux from engineering correlation and internal CFD data over a 7° cone at low-Reynolds-number conditions in the Longshot tunnel.

As can be seen in Fig. 2.2(a), the pressure from numerical computations (which account for the slight nose bluntness and pressure gradient) is asymptotic to the Taylor–Maccoll solution, valid for a sharp nose. In Fig. 2.2(b), the heat fluxes computed by CFD and by Eckert's correlation are in good agreement, especially as s' increases. Note, however, that such an agreement would be lost for larger nose bluntness as the theory would be used beyond its limit of validity.

A detailed comparison of engineering correlations for the prediction of heat transfer in zero-pressure-gradient compressible boundary layers with CFD and experimental data has been provided by Higgins (2008). Eckert's method was shown to give reasonably accurate heating rates over flat plates, wedges and cones for engineering purposes.

2.2.3. Blunt-body heating-rate distribution

Although the stagnation point and the flat plate are the two important self-similar compressible-flow solutions, practical problems of interest involve flows over more complex body geometries, with pressure gradients in the flow and variable edge properties. As stressed in Chapter 1, all hypersonic vehicles must have blunt noses to reduce aerodynamic heating.

This section now handles the case of a high-speed flow over arbitrary blunt-nosed bodies, for which a detached bow shock forms in front of the nose. While it can be assumed that the boundary layer remains laminar for some distance away from the stagnation point, the self-similar assumption is no more valid. Nonetheless, most theories for the estimation of off-stagnation-point heat flux treat the flow as if it was *locally similar*. This procedure consists in neglecting the derivatives with respect to the independent variable ξ (see Appendix A), while the local values are used for the terms depending on ξ through the external flow or the wall conditions. This reasonable assumption allows to greatly simplify the set of equations to solve.

L. Lees. In his pioneering paper published in 1956, Lees applied the concept of local similarity to estimate the laminar heat-transfer distribution around blunt bodies in dissociating high-speed flows. The limiting case of thermodynamic equilibrium, where all of the heat transfer is accomplished by conduction, is considered in the present study. The theory assumes perfect-gas chemistry and makes use of the fact that the pressure-gradient effect is small for highly cooled walls, i.e., walls such that $T_w \ll T_{aw}$. The method is based on an equivalent flat-plate solution applied locally to obtain the following closed-form expression for the heating rate:

$$\frac{\dot{q}_w}{(\dot{q}_w)_{\mathrm{SP}}} = \frac{F(s)}{2^{k/2}\sqrt{\frac{1}{u_\infty}\left(\frac{\mathrm{d}u_e}{\mathrm{d}s}\right)_s}}, \tag{2.18}$$

where $k = 0$ for a planar body or $k = 1$ for a body of revolution and the function F reads

$$F(s) = \frac{1/\sqrt{2}\ (p/p_{t2})(\omega_e/\omega_s)(u_e/u_\infty)\ r_b^k}{\left[\int_0^s (p/p_{t2})(\omega_e/\omega_s)(u_e/u_\infty)\ r_b^{2k}\ \mathrm{d}s\right]^{1/2}}, \tag{2.19}$$

where $\omega = \mu/(RT)$ and r_b is the radius of cross section of the body of revolution. Eq. 2.19 involves the integration of flow properties at the edge of the boundary layer (subscript e) all along the body surface described by the arc length s measured from the stagnation point.

This non-dimensional heat-transfer formulation allows eliminating several parameters in the

correlation and also permits a better comparison of surface heating for different geometries and Mach numbers. The stagnation-point heat transfer $(\dot{q}_w)_{\mathrm{SP}}$ should be estimated as accurately as possible, using for instance the Fay–Riddell equation (Eq. 2.9), as suggested by White (2006).

In the original paper, Lees (1956) further simplified his correlation for two canonical geometries, (i) a hemisphere of radius R_n and (ii) a blunt cone of half-angle θ_c capped by a spherical segment of radius R_n. He established expressions for the normalized heat flux $\dot{q}_w/(\dot{q}_w)_{\mathrm{SP}}$ as a function of only three parameters: γ, M_∞ and θ, the angle between the flight direction and the radius vector from the center of curvature of the nose.

(i) For the hemisphere,

$$\frac{\dot{q}_w}{(\dot{q}_w)_{\mathrm{SP}}} = \frac{2\theta \sin\theta \left(\left[1 - \frac{1}{\gamma_\infty \mathrm{M}_\infty^2} \right] \cos^2\theta + \frac{1}{\gamma_\infty \mathrm{M}_\infty^2} \right)}{\sqrt{D(\theta)}}, \tag{2.20}$$

with

$$D(\theta) = \left(1 - \frac{1}{\gamma_\infty \mathrm{M}_\infty^2}\right) \left(\theta^2 - \frac{\theta \sin 4\theta}{2} + \frac{1 - \cos 4\theta}{8}\right) + \frac{4}{\gamma_\infty \mathrm{M}_\infty^2} \left(\theta^2 - \theta \sin 2\theta + \frac{1 - \cos 2\theta}{2}\right). \tag{2.21}$$

The non-dimensional heat flux follows essentially a cosine variation for angles θ up to 70°.

(ii) For the blunt cone, the heat-transfer distribution over the nose is identical to that of the hemisphere (Eq. 2.20 and 2.21). On the conical skirt,

$$\frac{\dot{q}_w}{(\dot{q}_w)_{\mathrm{SP}}} = A(\theta_c) \frac{s'/R_n}{[B(\theta_c) + (s'/R_n)^3]^{1/2}}, \tag{2.22}$$

which is valid for $s'/R_0 \geq \cot\theta_c$, where s' is the distance along the surface measured from the virtual sharp tip. A and B are functions of γ, M_∞, θ_c and θ, but for $\mathrm{M}_\infty \sin\theta_c \gg 1$ they can be approached by

$$A(\theta_c) \cong \sqrt{\frac{3}{2}} \sin\theta_c \sqrt{\frac{\pi}{2} - \theta_c} \quad \text{and} \quad B(\theta_c) \cong \frac{3}{16} \frac{1}{\sin^4\theta_c} \left[\frac{D(\theta)}{\theta} \right]_{\theta = \frac{\pi}{2} - \theta_c} - \cot^3\theta_c. \tag{2.23}$$

Boundary-layer edge properties. Unlike the sharp cone, the boundary-layer edge properties of blunt bodies evolve along the body surface and their determination is less straightforward. Because of the curved shock and of the multiple nature of the shock layer, the inviscid blunt-body flow is very complex to solve ("blunt-body problem", (Anderson, 2006)). Inviscid CFD solutions can provide the edge conditions with a high level of fidelity, but the complexity of this approach is not really consistent within the framework of these rapid and approximate predictive tools. Some approximate methods are required, albeit at the expense of accuracy. The simplest and most commonly employed approach is to infer a pressure distribution over the body of interest combined with the knowledge of the stagnation conditions behind a normal shock.

The pressure distribution along the body surface can be evaluated using local surface inclination methods (Anderson, 2006), where the pressure at a point on the surface depends solely on the inclination angle θ_b between the local surface tangent and the free-stream direction. The

most famous of these methods is the Newton's sine-squared law, reading

$$C_p = 2\sin^2\theta_b. \tag{2.24}$$

Lees (1955) was the first to propose a modification to Eq. 2.24, accounting for the true stagnation-point pressure p_{t2}. This improvement is widely known as the Modified Newtonian Theory (MNT) and is considerably more accurate for blunt-nosed bodies than the original version. The pressure coefficient reads

$$C_p = C_{p,\max}\sin^2\theta_b, \tag{2.25}$$

where $C_{p,\max} = \frac{p_{t2}-p_\infty}{\frac{1}{2}\rho_\infty u_\infty^2}$ corresponds to the pressure coefficient at the stagnation point downstream of a normal shock and is typically lower than 2. The MNT turns out to be a good approximation provided that $\mathrm{M}_\infty \sin\theta_b > 1$, which is the strong-shock assumption or equivalently the thin-shock-layer assumption. Hence, the accuracy of the estimation decreases downstream of the stagnation region. Riley et al. (1990) added that the method does not adequately predict the pressure on spherically blunted slender geometries.

Once the pressure is known, the other local flow parameters at the edge of the boundary layer are assumed to be the same as if the air had passed through a normal shock wave and had experienced an isentropic expansion from the post-shock stagnation condition to the local pressure, therefore assuming that the entropy remains constant at the value directly downstream of the normal shock wave. The flow properties downstream of a normal shock can be computed as a function of properties upstream of a normal shock using the relations from the NACA report 1135. The edge Mach number, from which all other flow properties can be inferred, is calculated using the isentropic pressure ratio

$$\mathrm{M_e} = \sqrt{\left(\left(\frac{p_{t2}}{p_\mathrm{e}}\right)^{\frac{\gamma-1}{\gamma}} - 1\right)\left(\frac{2}{\gamma-1}\right)}. \tag{2.26}$$

To sum up, the idea of this approach for heat-transfer calculations is to first solve the inviscid flow field and then use the properties on the surface as edge conditions for a boundary-layer solution. Although this method is satisfactory for high Reynolds numbers, its accuracy diminishes as the flow proceeds downstream. More and more of the inviscid mass flow rate is entrained into the boundary layer as the latter grows along the surface. The high-entropy streamlines which crossed the normal portion of the bow shock are swallowed by the boundary layer. The flow at the edge of the boundary layer on the rear parts of the body will have crossed an oblique part of the shock and the entropy at the outer edge will not be the normal-shock entropy. This phenomenon is referred to as entropy-layer swallowing and is represented in Fig. 2.3. Although the edge pressure is almost the same as the surface pressure, the other properties can differ from those corresponding to post-normal-shock entropy. The heating rates can thus be significantly affected. To account for such swallowing effects, the boundary-layer solution and the inviscid flow-field solution must be coupled. In the present study, however, constant-entropy conditions are assumed. In a comparison between heating rates over blunt cones, Zoby et al. (1981) showed that the constant-entropy heating rate was slightly under-predicted compared to the real variable-entropy heat flux, but with reasonably small differences for the laminar case. This analysis supports the present choice.

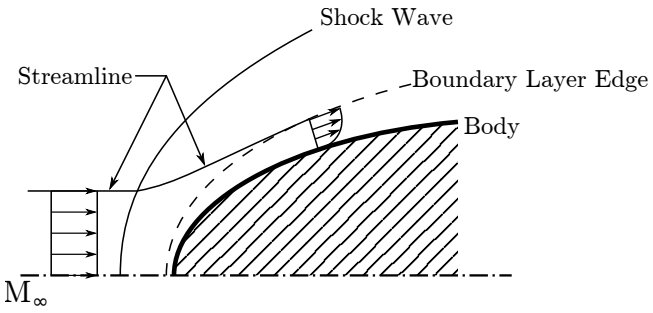

Figure 2.3: Entropy-layer swallowing for axisymmetric flow, redrawn from DeJarnette et al. (1987).

Zoby et al. Another notable engineering correlation for the prediction of convective heating rates around blunt vehicles is due to Zoby et al. (1981). The theory was developed for both non-reacting and reacting gas mixtures and is valid for both cold and non-cold walls. The laminar heat transfer is related to a skin-friction expression based on $\mathrm{Re}_{\theta,e}$ (momentum-thickness Reynolds number) through a modified Reynolds analogy. The method relies on an incompressible Blasius boundary-layer equation and makes use of the reference enthalpy concept presented earlier in § 2.2.2. The wall heat flux is given by

$$\dot{q}_w = 0.22\,(\mathrm{Re}_{\theta,e})^{-1}\left(\frac{\rho^*}{\rho_e}\right)\left(\frac{\mu^*}{\mu_e}\right)\rho_e u_e\,(h_{aw}-h_w)\,(\mathrm{Pr})^{-0.6}\,, \tag{2.27}$$

where θ is computed by

$$\theta = \frac{0.664\left[\int_0^s \rho^*\mu^* u_e r_b^2 \mathrm{d}s\right]^{1/2}}{\rho_e u_e r_b}. \tag{2.28}$$

Similarly to the method of Lees (1956), Eq. 2.27 and 2.28 require the knowledge of boundary-layer edge properties at each location s along the body. The edge conditions can be determined in the same way as explained above, that is, using the local pressure from the MNT and treating the boundary-layer edge as an isentropic surface. Other inviscid methods can be used (e.g., Taylor–Maccoll, though it corresponds to a sharp cone). Note that Zoby et al. (1981) proposed in their original publication a technique to account for variable-entropy effects, by "defining the boundary-layer edge properties as the inviscid values located at a distance equal to the boundary-layer thickness". It consists in an iterative process that must be coupled with an inviscid flow-field calculation.

Finally, this correlation should not be used to evaluate the stagnation-point heat flux because of a singularity in the formulation at $s = 0$. In their original paper, the authors recommend using Cohen's formulation (Eq. 2.10).

Other correlations. The methods of Lees (1956) and Zoby et al. (1981) are certainly the best-known correlations for blunt-body heating-rate predictions. They are still commonly employed several decades after their publication for research and industrial purposes (see for instance Martinelli and Braun (2010), Noori et al. (2012), Desai (2014) Liang et al. (2015)). These two approximate methods have been implemented in the present study. Yet, it is worth mentioning two other methods that have been developed following the work of Lees (1956). Shortly thereafter, Kemp et al. (1959) refined a bit the analysis by adding a correction involving a pressure-gradient parameter. It provided a 10% correction at most. Similarly, Crabtree et al. (1970) developed the original formulation to include a pressure-gradient parameter and a Lewis-number correction, in addition to evaluating fluid properties at some reference temperature.

Implementation and results. The present method to determine the boundary-layer edge conditions is compared to VKI internal numerical results in Fig. 2.4. The data correspond to inviscid CFD calculations of the flow over a sphere characterized by $T_\infty = 59.3$ K, $P_\infty = 340.6$ Pa and $\mathrm{M}_\infty = 11.3$. The coordinate x is the streamwise distance (on the centerline) with $x = 0$ at the stagnation point. It can be seen that the present method reasonably well predicts the pressure, Mach number and temperature at the edge of the boundary layer, but the accuracy decreases downstream as θ_b increases, especially for M_∞ and T_∞. The Modified Newtonian Theory is acceptably accurate as long as $\mathrm{M}_\infty \sin\theta_b > 1$.

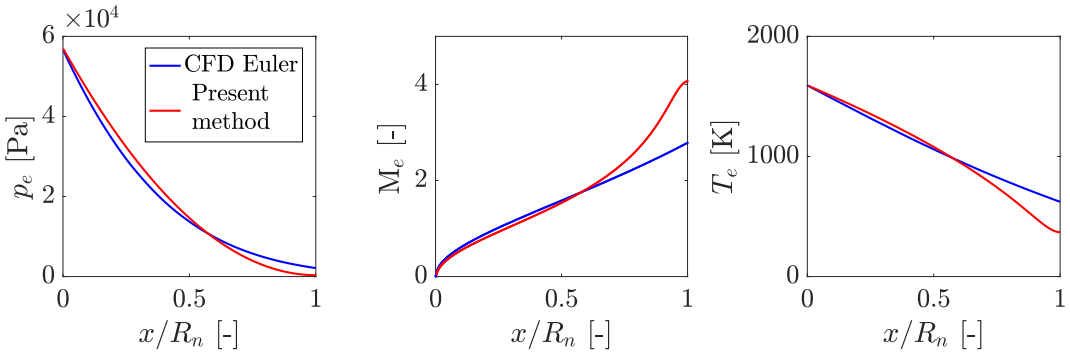

Figure 2.4: Comparison between boundary-layer edge pressure, Mach number and temperature over a sphere computed with the present method and obtained from internal VKI CFD computations, for $T_\infty = 59.3$ K, $P_\infty = 340.6$ Pa and $\mathrm{M}_\infty = 11.3$.

Boundary-layer edge conditions are also used in Eq. 2.3 to determine the adiabatic-wall temperature. In Fig. 2.5, the computed T_{aw} is compared to CFD results for the H3 Mach 6 flow over a 20-mm-nose-radius hemispherical cylinder (Fig. 2.5(a)) and 7.4°-half-angle cone (Fig. 2.5(b)). The numerical data result from the CFD analysis of Chapter 3 imposing a zero heat flux at the wall. The two considered shapes are actual wind-tunnel models of total length L_t. Despite the simplicity of the present approximate method, the latter yields distributions of T_{aw} not so far off the numerical results. The best agreement between the two approaches is found on the nose region of the bodies. Maximum differences of 1.8% and 2% are observed on the afterbodies of the sphere and the cone respectively.

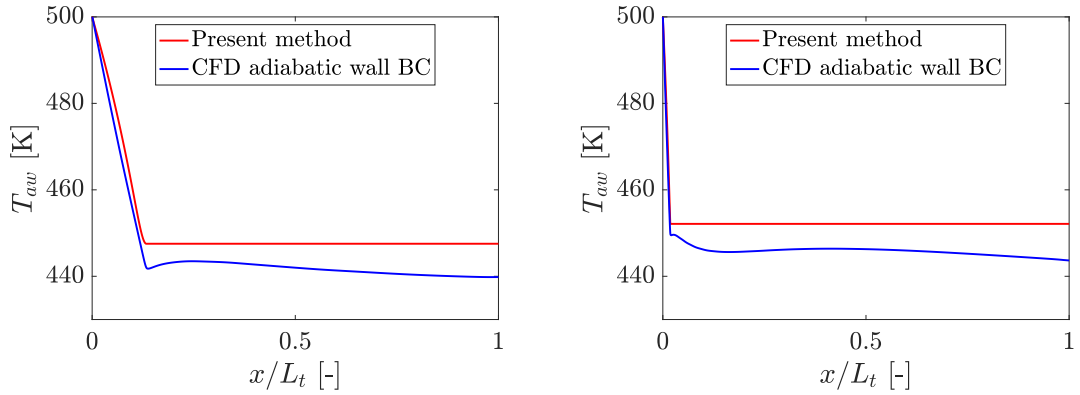

(a) Hemisphere-cylinder ($R_n = 20$ mm). **(b)** Blunt cone ($\theta_c = 7.4°$, $R_n = 3.5$ mm).

Figure 2.5: Comparison between adiabatic-wall temperature obtained with the present method and from CFD computations over a hemisphere-cylinder and over a blunt cone, for $T_0 = 500$ K, $p_0 = 20$ bar and $\mathrm{M}_\infty = 6$.

Finally, the results from the theoretical methods of Lees (1956) and Zoby et al. (1981) are confronted with external numerical and experimental data. Fig 2.6(a) corresponds to a Mach 6 flow of air over a sphere, while Fig. 2.6(b) considers the Mach 8 flow over a 25°-half-angle blunt cone. The coordinate θ is the polar angle of the sphere and s is the arc length measured from the stagnation point. The agreement between the two engineering correlations is overall very good. They compare relatively well with CFD and experimental results, especially in the case of the hemisphere. For the blunt-cone flow, the largest difference is observed near the junction between the spherical cap and the conical afterbody. This discrepancy originates from the fact that the modified Newtonian pressure distribution fails to predict the overexpansion around the shoulder of the blunt cone as well as the subsequent recompression on the conical afterbody, as stressed by Riley et al. (1990). Further downstream, the different results match again.

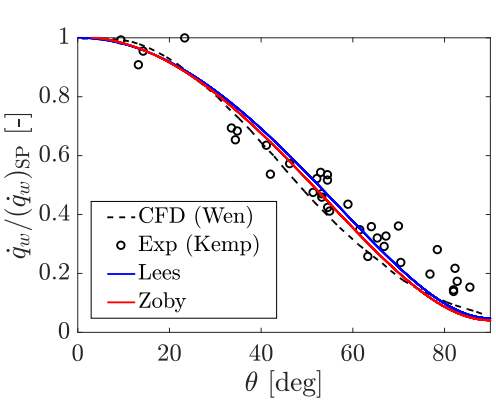

(a) Hemisphere ($M_\infty = 6$, air).

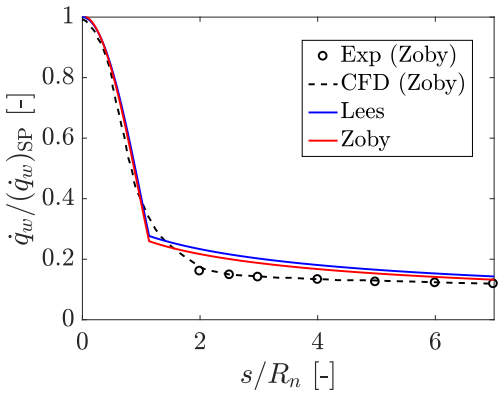

(b) Blunt cone ($M_\infty = 8$, $h_w/h_s = 0.42$, $\theta_c = 25°$).

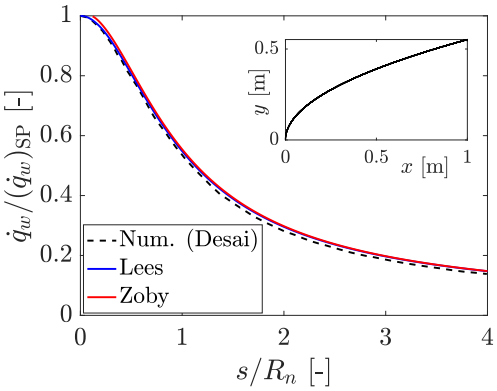

(c) Parabola ($M_\infty = 15$, $R_n = 0.15$ m, geometry in inset figure).

Figure 2.6: Comparison between heat-flux distributions yielded by the engineering correlations and by external CFD results and experiments, from Wen (1994), Kemp et al. (1959), Zoby et al. (1981) and Desai (2014).

The MATLAB code implemented in the present study is very general and can treat any axisymmetric geometry specified by its (x, y) coordinates. Other tested geometries include an ellipsoid, an Apollo-capsule-liked shape, and a paraboloid. For the latter case, comparison and validation have been made with the numerical results of Desai (2014) in Fig. 2.6(c).

2.3. Boundary-layer transition

This section briefly introduces the concept of boundary-layer transition and its crucial role in the framework of hypersonic convective aerodynamic heating. It is certainly not the purpose to go into the details of this complex flow phenomenon as it goes beyond the scope of this work. The reader is warned that only a global overview is given here.

The previous section discussed procedures for calculating convective heat transfer when the flow is laminar. However, a laminar boundary layer might transitions to a turbulent state because of the appearance and subsequent growth of disturbances within it. The former smooth, ordered and regular motion of the flow elements is then replaced by a chaotic, disordered turbulent flow. The transition process is schematically represented in Fig. 2.7.

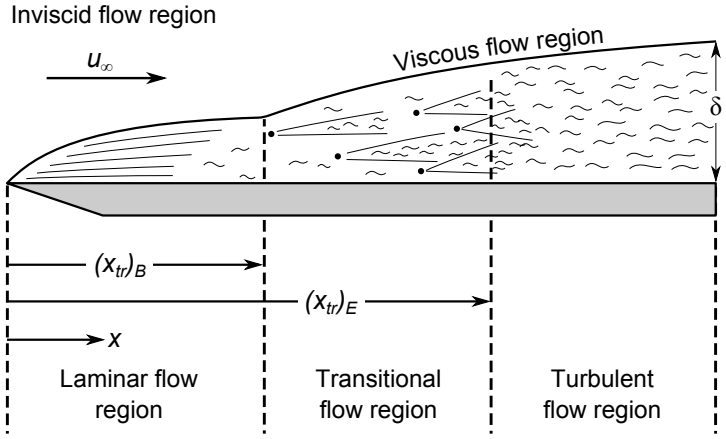

Figure 2.7: Schematic illustration of boundary-layer development and transition process, from Pate (1978) and redrawn by Grossir (2015).

The transition of the boundary layer from laminar to turbulent is one of the most complex problems in fluid mechanics that becomes even more difficult to apprehend when reaching the hypersonic regime. The strong mixing ability of turbulent motion leads to increased skin friction and heating rates which, at hypersonic speeds, might be up to one order of magnitude larger than the laminar heating rates, as shown in Fig. 2.8. This heat-flux rise associated with boundary-layer transition constitutes a serious threat to the survival of high-speed vehicles. The development of accurate and reliable methods for predicting transition thus appears essential for hypersonic machinery designers in order to avoid the penalties resulting from conservative design. However, despite the significant efforts that have been devoted to this task over the years, engineers are currently neither able to completely understand nor to predict such phenomenon. This imprecise knowledge mainly stems from the fact that boundary-layer transition is influenced by numerous and often interrelated parameters.

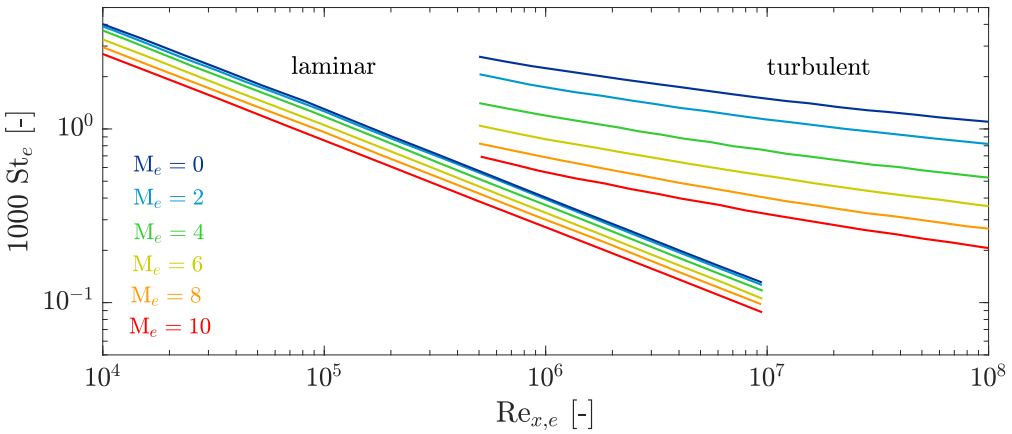

Figure 2.8: Stanton number as a function of Reynolds number for an insulated flat plate in free flight at different Mach numbers, replotted from van Driest (1956).

Among the most significant flow parameters affecting boundary-layer transition are Mach number, free-stream turbulence, surface roughness, wall cooling, pressure gradient, free-stream Reynolds number and nose bluntness (Anderson, 2006). For instance, blunting the nose of a hypersonic vehicle generally tends to stabilize the boundary layer. For moderate bluntness, the transition location moves further downstream. Yet, a too large increase in the nose bluntness might lead to the transition-reversal phenomenon (or blunt-body paradox), where the transition Reynolds number decreases dramatically and transition occurs upstream on the nose. In the present case, the bluntness of the test models has a pure stabilizing effect without transition-reversal regime. Regarding the Mach number influence, stability theory has shown that the laminar boundary layer is stabilized by an increasing local edge Mach number. Compressibility effects are thus beneficial as they delay the transition onset.

A variety of in-flight and wind-tunnel experiments has been conducted over the years in order to (try to) develop simple correlations for the prediction of transition onset at hypersonic speeds. For engineering analyses, it is frequently assumed that transition takes place at one point, the transition point, denoted x_{tr}. The transition Reynolds number is then defined as

$$\mathrm{Re}_{\mathrm{tr}} = \frac{\rho_e u_e x_{\mathrm{tr}}}{\mu_e}. \tag{2.29}$$

This definition is an over-simplification of the reality since, as shown in Fig. 2.7, the transition takes place over a finite length, which, for high-speed flows, can be of the same order as that over which the laminar boundary layer develops (Stetson, 1987). Many predictive correlations make use of $\mathrm{Re}_{\mathrm{tr}}$ or some variant, such as the popular $\mathrm{Re}_{\theta_{\mathrm{tr}}}/\mathrm{M}_e = \mathrm{cst}$ using a modified Reynolds number based on a momentum thickness θ. A large number of criteria also exists in the framework of roughness-induced transition, such as the Shuttle and PANT criteria. For wind-tunnel applications, Pate (1978) proposed a method to predict the *end* of transition on flat plates and sharp cones at zero angle of attack, relying on wind-tunnel characteristics (thus not applicable to flight). Masutti (2013) applied this method on a 7°-half-angle sharp cone in the VKI H3 facility and showed good agreement with experimental results. The transition locations obtained from Pate's correlation were 152 mm, 170 mm, 198 mm and 233 mm, respectively, for unit Reynolds numbers of $27.1 \cdot 10^6$ /m, $22.8 \cdot 10^6$ /m, $18 \cdot 10^6$ /m and $14.1 \cdot 10^6$ /m. Again, these results,

obtained for a sharp cone at Mach 6, support the fact that no transition was observed in the present H3 study, where models' lengths do not exceed 170 mm and models' noses are blunt.

Nevertheless, it should be reminded that such empirical models are limited to the particular geometries and the particular flow conditions for which they were developed. Hence, using these results beyond their range of validity can lead to completely wrong predictions. There is a general lack of physics involved in such transition-criterion methods because they are semi-empirical in nature (see for instance the word of caution of Reshotko (2007) about the popular $\mathrm{Re}_{\theta_{\mathrm{tr}}}/\mathrm{M}_e$ correlation). Besides, wind-tunnel measurements are not representative of in-flight conditions due to wind-tunnel inherent noise which causes earlier transition on models, stressing the need for quiet hypersonic facilities (Schneider, 2008).

The transition phenomenon has also been investigated theoretically through stability methods and perturbation theory (see Miró Miró (2020) for a detailed review of these approaches). The linear stability theory is one of the most famous linearized theories that studies the development of instabilities in transitioning flows. It is concerned with the typical natural transition where modal growth of disturbances dominates, though other paths to turbulence exist (Morkovin, 1994). The theory can be used to examine the frequency and growth rate of the most unstable dominant modes in the boundary layer. Important results were derived for compressible flows (Mack, 1984). In hypersonic boundary layers, beside the first-mode instability (counterpart of Tollmien–Schlichting waves in the low-speed boundary layer), there exist higher linear unstable modes (Mack modes), which correspond to inviscid instabilities. The so-called second mode dominates the transition process in hypersonic boundary layers developing over flat plates, sharp wedges and cones.

Notwithstanding the progress made in better understanding the complex transition phenomenon, the linear stability theory itself is not able predict the transition location x_{tr}. This is why an approximate method for transition prediction has been introduced independently but simultaneously by Smith and Gamberoni (1956) and van Ingen (1956): the e^N method. The latter states that transition occurs when the logarithm of the non-dimensional perturbation amplitude is increased by a critical amount, the so-called N-factor. Thus, it first requires to know the growth rate α_i obtained from linear stability theory. Besides, this method is still not very general since the N-factor has to be fed to the model (e.g., from experiments) if one desires to extract x_{tr}. In fact, the transition-onset N-factor depends on the disturbance environment and it is commonly assumed that wind tunnels with similar turbulence levels have similar N-factors. A value of $N = 5.5$ is typical of conventional noisy hypersonic wind tunnels (Masutti, 2013).

The accurate prediction of boundary-layer transition, whether by means of theories or empirical correlations, is still a leading state-of-the-art challenge, going well beyond the objectives of this work. The wind-tunnel models and test conditions presently considered are more prone to laminar boundary layers; no transition has been observed experimentally. If present, the transition process could have been detected by the infrared thermography, though. It is well established that hypersonic transition goes along with a gradual and rather linear rise in heat transfer over the body, joining the laminar value at the beginning of transition to the turbulent one at the end of the process (Richards, 1979). Hence, measurements of wall heat fluxes are recognized as one of the simplest and most reliable techniques to infer the transition location. In VKI, many efforts have been devoted to the experimental investigation of the transition to turbulence, with the notable contributions of Masutti (2013) and Grossir (2015).

2.4. Turbulent heat transfer

This section handles aerodynamic heating in hypersonic flows where transition has occurred and the boundary layer is fully turbulent. As warned by Anderson (2006), "the analysis of turbulent boundary layer is in the same category as predicting transition, that is, empirical data are required" to compensate for the lack of fundamental knowledge about the physical mechanisms involved. Turbulent heating methods are highly dependent upon experimental data for determining certain constants and there is always an uncertainty in the results. Similarly to boundary-layer transition, turbulent boundary layers are not the focus of this work which is mainly concerned with laminar viscous flows, but dedicated sections are still required for completeness of the analysis. Several approximate theories for off-stagnation-point turbulent heat transfer have been developed and only some of the most notable ones are presented hereafter (see Hopkins and Inouye (1971) for a thorough review).

All approximate methods for turbulent heating were established for zero-pressure-gradient boundary layers. These theories use some form of Reynolds analogy to relate skin-friction coefficient and Stanton number and are based on extending the well-known incompressible results to the compressible hypersonic case through compressibility transformations. The idea is the same as described in § 2.2.2. Among the most widely used engineering methods are the reference temperature of Eckert (1956) and the van Driest II method from van Driest (1956).

The reference temperature concept of Eckert, introduced in the laminar case in § 2.2.2, also applies for turbulent boundary layers. The compressible skin-friction coefficient, derived from the well-known incompressible result $C_f = 0.0592 \cdot \mathrm{Re}_{s,e}^{-0.2}$, is given by

$$C_f = \frac{0.0592}{(\mathrm{Re}_{s,e})^{0.2}} \left(\frac{T_e}{T^*}\right)^{0.6} \left(\frac{\mu^\star T_e}{\mu_e T^*}\right)^{0.2}, \tag{2.30}$$

where star quantities are evaluated at the reference temperature T^* of Eq. 2.15. The turbulent recovery factor is $r = \mathrm{Pr}^{1/3}$, from Eq. 2.4. As before, the flow properties at the edge of the boundary layer can be easily obtained from exact theories such as the Taylor–Maccoll solution for sharp cones, for instance. The Stanton number is then obtained through a Reynolds analogy. The Reynolds analogy factor appearing in Eq. 2.16 is subject to debate in the literature. Hopkins and Inouye (1971) recommended $R_f = 1.0$ (classical Reynolds analogy) for turbulent boundary layers with significant wall cooling, and $R_f = 0.83$ for adiabatic-wall conditions. Tauber (1989) stated that $R_f = \mathrm{Pr}^{2/3}$, as used for the laminar case, usually results in good agreement with test data. For reasonable values of R_f, refer to the graphs of van Driest (1956).

The supersonic flow past a sharp cone at zero incidence results in an attached shock wave and a vanishing pressure gradient, so that the boundary layer has properties similar to flat-plate flow. van Driest (1956) showed that the local Stanton number for a cone in axial flow is 1.15 times as great as for a flat plate under the same local conditions. White (2006) suggested a multiplicative factor of 1.176 to extend the flat-plate results to cones. Note the difference with the laminar case, where the Mangler transform resulted in a $\sqrt{3}$ factor (Eq. 2.17).

The method of van Driest (1956) is very popular for turbulent heat-rate estimations. According to DeJarnette et al. (1987) and White (2006), van Driest II is believed to be the most

accurate formula for compressible flat-plate skin-friction coefficient. It is based on the extension of von Karman's mixing-length incompressible-flow theory accounting for density and viscosity changes with temperature. The formula reads

$$\frac{0.242}{C_f^{1/2}\left(\frac{\gamma-1}{2}\mathrm{M}_e^2\right)^{1/2}}(\arcsin\alpha+\arcsin\beta)=0.41+\log_{10}\left(\mathrm{Re}_{s,e}\cdot C_f\cdot\frac{\mu_e}{\mu_w}\right), \tag{2.31}$$

where

$$\begin{aligned}\alpha&=\left(2A^2-B\right)/\left(B^2+4A^2\right)^{1/2},\\ \beta&=B/\left(B^2+4A^2\right)^{1/2},\\ A^2&=\left(\frac{\gamma-1}{2}\mathrm{M}_e^2\right)/\left(\frac{T_w}{T_e}\right),\\ B&=\left(1+\frac{\gamma-1}{2}\mathrm{M}_e^2\right)/\left(\frac{T_w}{T_e}\right)-1.\end{aligned} \tag{2.32}$$

Eq. 2.31 is implicit in C_f and can be solved with the Newton–Raphson method, for instance. As for Eckert, the heat transfer is finally obtained through the Reynolds analogy.

For practical applications, it is desired to predict the turbulent heat-transfer distribution over arbitrary blunt geometries. As noted by Crabtree et al. (1970), "the effect of pressure gradient on the characteristics of a turbulent boundary layer, especially heat-transfer, is much less than for a laminar boundary layer". He added that using the zero-pressure-gradient formulas evaluated at true local conditions and at a reference enthalpy have demonstrated to be reasonably accurate for flows with modest pressure gradients. These correlations remain commonly used approximations of sufficient accuracy for slender bodies. Properties at the edge of the boundary layer can be evaluated following the process explained in § 2.2.3, i.e., inferring a pressure distribution from the Modified Newtonian Theory and assuming an isentropic expansion from the conditions just behind a normal shock wave, therefore ignoring the effects of the entropy gradient produced by the curved shock wave.

The attempts to include the effect of pressure gradients in simple engineering methods have, in general, failed to give improvement compared to the equivalent flat-plate approaches. To account for pressure gradient, one should rely on more complex approaches going beyond the scope of these simple engineering calculations (White, 2006).

In the context of blunt-body heating, Crabtree et al. (1970) recommended a simple integral correlation where flow properties are evaluated at some reference temperature T^*:

$$\dot{q}_w=0.5\rho^* u_e \mathrm{Pr}^{-2/3}(h_{aw}-h_w)C_f^*, \tag{2.33}$$

with

$$C_f^*=\frac{0.288}{\left[\log_{10}\left(\frac{\rho^* u_e X}{\mu^*}\right)\right]^{2.45}} \tag{2.34}$$

and

$$X=\frac{\int_0^x \rho^*\mu^* u_e r_b^2 \mathrm{d}x}{\rho^*\mu^* u_e r_b^2}. \tag{2.35}$$

The errors associated with this approximation might be up to 15%, though, as noted by the authors.

The method of Zoby et al. (1981), previously presented for a laminar boundary layer over a blunt body, can be extended to the turbulent case, but with a strong basis of empiricism. The correlation allows to take into account, or not, variable edge conditions and is given by

$$\dot{q}_w = c_1 \left(\mathrm{Re}_{\theta,e}\right)^{-m} \left(\frac{\rho^*}{\rho_e}\right) \left(\frac{\mu^*}{\mu_e}\right)^m \rho_e u_e \left(h_{aw} - h_w\right) \left(\mathrm{Pr}\right)^{-0.4}, \tag{2.36}$$

with

$$\theta = \frac{\left(c_2 \int_0^s \rho^* {\mu^*}^m u_e r_b^{c_3} \mathrm{d}s\right)^{c_4}}{\rho_e u_e r_b}, \tag{2.37}$$

where m, c_1, c_2, c_3 and c_4 are constants empirically determined given in the paper.

Implementation and results. The turbulent heating engineering correlations have been implemented and some turbulent results are presented in Fig. 2.9. For Eckert's and van Driest's calculations, $R_f = 0.825$ was used. The turbulent heating over a 7°-half-angle blunt cone at Mach 9.5 is presented in Fig. 2.9(a), where the CFD results have been internally established in VKI. Only Eckert's and van Driest's correlations are presented since the body is considered as being a sharp cone. The two methods provide results in good agreement with the numerical data, especially for van Driest (1956). In Fig. 2.9(b), experimental data from Zoby et al. (1981) are compared with the turbulent heating predictions of Zoby et al. and Crabtree et al. for a hemispherical cylinder, which is a typical blunt body. The engineering predictions are rather close to the experimental data, even if few data points are available. Laminar heating predictions are also shown to emphasize the difference in the order of magnitude between laminar and turbulent heating.

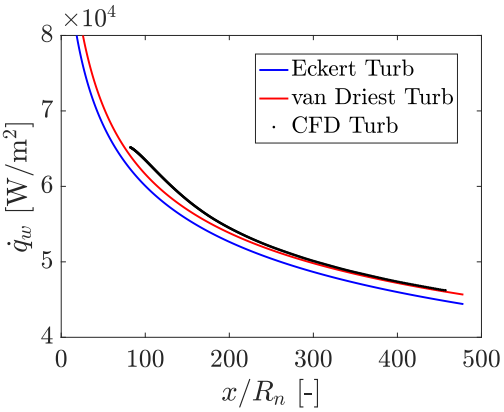

(a) Blunt cone ($\theta_c = 7°$, $R_n = 1.75$ mm, $\mathrm{M}_\infty = 9.5$, $P_\infty = 276$ Pa, $T_\infty = 88.6$ K, VKI internal data).

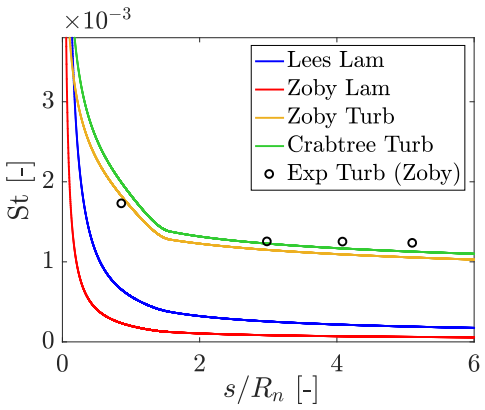

(b) Hemispherical cylinder ($R_n = 0.1$ m, $h_w/h_s = 0.6$, $\mathrm{M}_\infty = 2.15$, from Zoby et al. (1981)).

Figure 2.9: Comparison between turbulent heating rates of engineering correlations and internal/external higher-fidelity data.

2.5. Engineering-level predictive tools

So far, relatively simple approximate methods for the prediction of convective aerodynamic heating in both laminar and turbulent flows have been discussed. The attention was restricted to axisymmetric bodies at zero angle of attack, thus enabling a two-dimensional analysis along the body's centerline. In fact, these simple theoretical methods are at the basis of more advanced industry-standard codes used for heat-transfer studies at the preliminary design level. It is clear that such practical engineering codes must handle three-dimensional arbitrary configurations while remaining fast and efficient with far less computational efforts than more sophisticated CFD techniques. To end this chapter about theoretical tools, this section aims to present an example of such more advanced tools.

The work of Cooke (1961) on the axisymmetric analogue set the ground for further work in three-dimensional geometry analysis. Following this approach, the three-dimensional boundary-layer equations are expressed in a streamline coordinate system and the cross-flow velocity component is assumed to be null. Then the equations can be reduced to a form similar to those for axisymmetric flows. This allows to analyze complete geometries by covering multiple streamline paths. Most engineering codes are formulated around dividing the flow over the body into streamlines and then analyzing the flow properties along each streamline. These codes can then achieve 3D aerodynamic heating predictions by implementing the approximate methods presented throughout this chapter.

The Configuration Based Aerodynamics (CBAERO) software package is an example of engineering-level tool for aero- and aerothermo- dynamic predictions of general 3D hypersonic vehicle configurations (Kinney, 2004, Kinney et al., 2006). The different steps followed by the software to achieve heating predictions are summarized in Fig. 2.10.

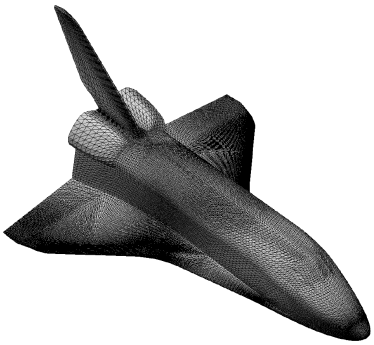

(a) Triangular surface mesh.

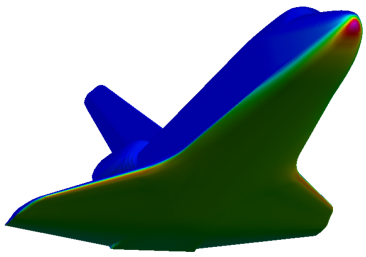

(b) Pressure distribution (MNT) and inviscid solution.

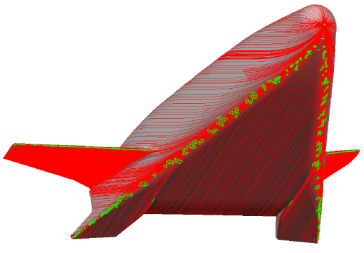

(c) Streamlines tracing and attachment-line detection.

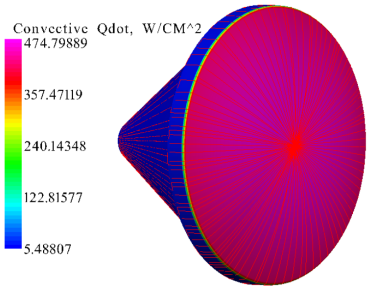

(d) Aerothermodynamic computations.

Figure 2.10: CBAERO computation process (Kinney, 2004).

The first step is the definition of the vehicle geometry using unstructured triangular meshes (Fig. 2.10(a)). Secondly, an inviscid solution is calculated using independent panel methods, such as the Modified Newtonian method (MNT) that provides the pressure at each surface triangle (Fig. 2.10(b)). Shadowed surfaces, i.e., surfaces not directly exposed to the incoming flow because of upstream surfaces, are detected and assigned a vanishing pressure coefficient. Assuming the entropy at each panel to be equal to the post-normal-shock entropy, the thermodynamic state at the edge of the boundary layer is fixed. Variable-entropy edge conditions can also be accounted for using a mass-balancing procedure. Then, given an inviscid flow field, a simple and robust algorithm integrates the 3D streamline ordinary differential equations and traces the streamline pattern over the entire vehicle (Fig. 2.10(c)). A specific method making use of topology considerations and eigenvector analysis of the velocity gradient tensor is used to detect the attachment lines.

Once the inviscid flow field, streamline patterns, stagnation point and attachment lines are defined, the viscous solution over the surface of the vehicle can be readily estimated (Fig. 2.10(d)). The correlation of Tauber et al. (1987) is used to predict the stagnation-point and attachment-lines heating. The off-stagnation heating model is based on either laminar or turbulent flat-plate reference enthalpy methods (typically Eckert (1956)). A Mangler correction is used to correct the two-dimensional estimates. The local Reynolds number is calculated using the running lengths based on the streamline patterns.

The software can be run fully laminar, fully turbulent or transitional, in which case a simple $\mathrm{Re}_{\theta_{\mathrm{tr}}}/\mathrm{M}_e$ criterion is used to determine the onset of boundary-layer transition. In addition to convective aerodynamic heating calculation, the software can also achieve radiative heating predictions (using again engineering correlations) and includes a partially catalytic-wall model. Aerodynamic loads are obtained by integrating the forces acting on all surfaces, following directly from the local pressure. The predictions from CBAERO, obtained within few seconds or minutes, have been compared favorably to high-fidelity CFD solutions and flight-test data. Typical test cases included the Space Shuttle Orbiter, the Apollo Command Module and the X-33.

Other examples of industry-standard codes include MINIVER (Hender, 1970), AEROHEAT (DeJarnette and Hamilton, 1973) and INCHES (Zoby and Simmonds, 1985), for instance. All have shown to compare well to higher-fidelity Navier–Stokes simulations. The inviscid flow-field solution, streamline calculation procedure and convective-heating formulation is specific to each code, with more or less flexibility in the user options.

The VKI in-house code ANTARES (Durbin et al., 2020), short for Application of Newtonian Theory for ARbitrary Entry Shapes, has the potential for similar development. The code is currently able to achieve hypersonic aerodynamic predictions with a good degree of accuracy and low computational cost over arbitrary 3D geometries (e.g., Apollo Command Module, Space Shuttle). It requires the definition of free-stream flow properties and a surface mesh representing the geometry. The main feature of ANTARES is the application of the Newtonian flow model for the determination of the pressure distribution along the whole body surface. For non-shadowed surfaces, the code uses the modified version proposed by Lees (1956) in Eq. 2.25. Upon integration of the local pressure and associated forces all over the object, the global aerodynamic forces (lift, drag and side forces) and moments can be extracted, as well as other

quantities of interest such as the center of pressure.

By relying on the Modified Newtonian Theory, the code already has the basic ingredients towards aerothermodynamic predictions. An interesting future extension of the tool would be to include a streamline-tracing procedure together with engineering correlations for convective (and radiative) aerodynamic heating, thus enlarging the capabilities and field of application of this VKI tool.

3. CFD analysis

Numerical simulations have been performed to support experimental measurements and theoretical predictions for the heating rates over axisymmetric geometries. The present numerical analysis focuses on the two canonical shapes that were available for wind-tunnel testing, i.e., a hemispherical cylinder and a blunt cone.

This chapter provides a detailed account of the numerical setup, including governing equations and solver parameters, computational domain and mesh. Some results are finally presented. Three main technical tools were used to address at best the requirements of this part. The mesh has been created thanks to GAMBIT, the former meshing tool of FLUENT (2021). It should be noted that it was Dr. G. Grossir who carried out the meshing-creation part of this work. The flow has been solved using the CFD++ commercial software, developed by Metacomp Technologies, Inc. (2021). Results have been post-processed and visualized using TECPLOT 360 (Tecplot, Inc., 2021).

3.1. Governing equations and solver settings

The governing equations solved are the two-dimensional axisymmetric compressible Navier–Stokes equations, using a perfect-gas flow model of air. The classical values $\gamma = 1.4$ and $R = 287\ \mathrm{J/(kg \cdot K)}$ are used. Sutherland's law is employed to model both viscosity and thermal conductivity as functions of temperature, according to

$$\chi = \chi_{\mathrm{ref}} \left(\frac{T}{T_{\mathrm{ref}}} \right)^{\frac{3}{2}} \frac{T_{\mathrm{ref}} + S}{T + S}. \tag{3.1}$$

The coefficients used for the viscosity law are $\mu_{\mathrm{ref}} = 1.716 \cdot 10^{-6}\ \mathrm{kg/(s \cdot m)}$, $T_{\mathrm{ref}} = 273.11\ \mathrm{K}$, $S = 111\ \mathrm{K}$, while those employed for the conductivity law are $k_{\mathrm{ref}} = 2.41 \cdot 10^{-2}\ \mathrm{W/(m \cdot K)}$, $T_{\mathrm{ref}} = 273.11\ \mathrm{K}$ and $S = 194\ \mathrm{K}$. The resulting Prandtl number is also a function of temperature, contrary to the theoretical investigation of Chapter 2 throughout which $\mathrm{Pr} = 0.71$ has been assumed. For the present effort, simulations were run fully laminar, as the studied flow fields are expected to exhibit laminar boundary layers. The computations have been performed at the typical H3 wind-tunnel test conditions (Mach 6 and low, medium and high Reynolds number, see Table 4.1) and more precisely at the actual experimental conditions to allow for better comparison of the results (Chapter 5).

An implicit backward Euler time-integration method with a W-cycle multi-grid acceleration scheme is selected to converge the solution towards steady-state. The point-implicit time-stepping option allows for a rather large Courant–Friedrichs–Lewy (CFL) number, which is controlled from the recommended CFL-ramping schedules for hypersonic flows (CFL number gradually ramps from 0.1 to 10). Regarding the tolerances, the residuals are required to drop

by more than 10 orders of magnitude to ensure convergence of the iterative scheme.

The basis of the spatial discretization in CFD++ is a multi-dimensional Total Variation Diminishing (TVD) polynomial interpolation. In this case, node-based polynomials and a continuous flux limiter are used, along with the approximate HLLC Riemann solver to solve a local Riemann problem at the cell interface. Equations are discretized with second-order accuracy.

3.2. Computational domain

3.2.1. Geometry

Two basic geometries are considered. The hemispherical cylinder model consists of a hemisphere of radius R_n attached to a cylindrical afterbody, for a total body length of $L_t = 7.5R_n$. The blunt-cone model is composed of a cone of semi-vertex angle θ_c, capped by a spherical segment of nose radius R_n. A total body length of $L_t = 50.4R_n$ was modeled for the present case. The only relevant parameter that must be fixed is the cone half-angle, set to $\theta_c = 7.4°$, since this corresponds to the actual wind-tunnel model for which the few experiments have been carried out.

The computation domain for the case of the hemispherical cylinder is depicted in Fig. 3.1. The domain for the blunt-cone model is essentially the same, with the only difference that, on the afterbody, the wall boundary is inclined by the cone half-angle θ_c with respect to the free-stream x-direction.

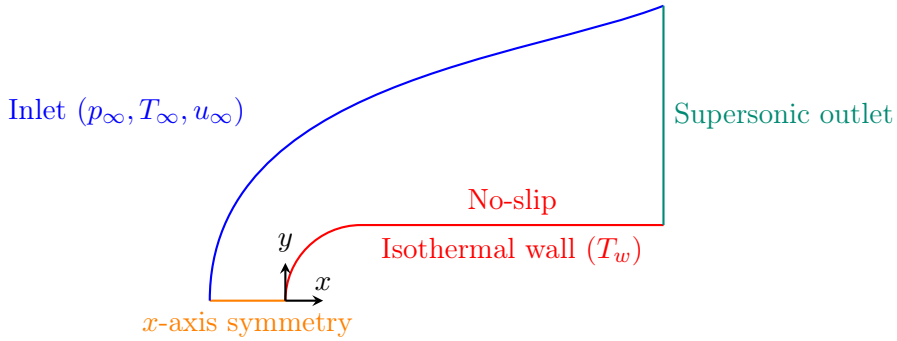

Figure 3.1: Computational domain geometry for the hemispherical cylinder (not to scale).

Only half of the model is considered thanks to the axisymmetry of the problem (axisymmetric geometry and zero angle of attack), thus saving computational cost. The dimensions of the computational domain are defined so as to include the shock wave forming in front of the nose and curving further downstream. Besides, contrary to the subsonic flow regime, the information (i.e., the presence of the body) cannot propagate upstream so that the flow domain before the shock wave does not have to be large. The correlations of van Dyke (1958) are used to estimate as a first guess the shock stand-off distance Δ/R_n and thus to scale the x-axis symmetry boundary. For $M_\infty = 6$, one gets $\Delta/R_n \approx 0.15$. Note that Δ/R_n could also have been approximated experimentally from available schlieren pictures. The shape of the shock wave,

constraining the shape of the inlet boundary, can be estimated from the results of Billig (1967) obtained from experimental data. The correlation for the shock coordinates depends on the nose radius, the shock stand-off distance, the Mach number and it is assumed that the wave is a hyperbola asymptotic to the free-stream Mach angle or, in the case of a conical afterbody, to the attached shock angle. Variations of the shock-wave angle with cone semi-vertex angle and free-stream Mach numbers are provided in the NACA report 1135.

3.2.2. Boundary conditions

In Fig. 3.1 the boundary conditions (BC) of the domain are also shown. BC should be consistent with the flow physics and are defined in this case as follows.

(i) At the inlet, from the theory of characteristics for hyperbolic problems (Hirsch, 2007), all relevant variables must be prescribed: free-stream temperature, free-stream pressure and free-stream velocity vector. The combination of T_∞, p_∞ and u_∞ ($v_\infty = 0$) is decided by the actual H3 conditions (for instance the low-, medium- and high-Reynolds-number cases) at $\mathrm{M}_\infty = 6$.

(ii) The outlet is supersonic and none of the characteristics enters the domain through this boundary. Hence, no physical condition has to be given and all variables are extrapolated at this boundary.

(iii) A flow symmetry is simply imposed at the x-axis symmetry boundary, which represents in fact the stagnation streamline.

(iv) At the wall, the classical no-slip condition is applied for the velocity, while the pressure is assigned a vanishing gradient. Besides, an isothermal-wall condition is imposed. The constant temperature T_w is set to best match the time instant at which the IR images are processed for the experimental analysis, but it is considered uniform all along the body surface, while it is not the case in practice. Note, however, that the exact setting of T_w is not important for the comparison of the results since heat fluxes will be normalized into Stanton numbers, where the increase in T_w and the decrease in $\dot{q}_w$ cancel each other out. For the numerical data presented in this chapter, $T_w = 293$ K was used.

The entire domain is initialized with flow properties defined at the inlet boundary. Initial conditions are quickly forgotten as the solution converges to steady-state so that their specification is less crucial than for BC.

3.3. Mesh

3.3.1. Requirements

The physical domain is discretized with a non-uniform structured quadrilateral grid in a two-dimensional axisymmetric setting. The grid has been defined to fulfill the following requirements.

On the one hand, refinement of the mesh at the wall in the wall-normal direction is necessary to accurately capture the gradients of the boundary layer and thus the wall heat fluxes. The mesh lines should thus be guided to obtain cells as normal as possible to the solid boundary. Because the boundary layer thickens with running length, the normal grid spacing at the end of the body is allowed to be larger.

On the other hand, well capturing the shock position with a fine mesh is not only important for the shock position itself but also for the solution quality of the flow field downstream of the shock, including the heat fluxes at the wall (Bonfiglioli et al., 2012). Misalignment of the grid with the bow shock wave can generate large errors that can become trapped in the stagnation region (Candler, 2018). The refinement should be normal to the shock since changes across a shock wave occur only in the shock-normal direction. The shock shape and position can be firstly estimated as explained in § 3.2. Then the grid is refined around the computed shock, in an iterative process.

Lastly, the resolution of the mesh before the shock can be lower since free-stream quantities do not vary there.

3.3.2. Mesh convergence study

A grid convergence study is performed for one representative flow condition (the medium-Re case, i.e., $\mathrm{Re}_{\mathrm{unit},\infty} = 17 \cdot 10^6$ m^{-1}), assuming conclusions to be valid for the others. An initial coarse mesh is successively refined into a medium and a fine mesh, by increasing the number of cells in the shock-layer region ($N_{\mathrm{aft-shock}}$) and decreasing the first grid size at the wall (normalized $\Delta x_{1_{\mathrm{SP}}}/R_n$ at the stagnation point and $\Delta x_{1_{\mathrm{base}}}/L_t$ at the base, with R_n the nose radius and L_t the total body length). The numbers of cells along the body (N_{body}) and upstream of the shock ($N_{\mathrm{up-shock}}$) are kept constant. These mesh specifications are summarized in Table 3.1. The blunt-cone mesh contains more cells along the body surface because of the longer length of the model with respect to its smaller nose tip.

Table 3.1: Mesh parameters for the grid independence study.

Mesh	N_{body}	$N_{\mathrm{up-shock}}$	$N_{\mathrm{aft-shock}}$	$\Delta x_{1_{\mathrm{SP}}}/R_n$	$\Delta x_{1_{\mathrm{base}}}/L_t$	Cells
Hemisph.-Cyl.						
Coarse	375	20	75	$1.5 \cdot 10^{-4}$	$2.8 \cdot 10^{-4}$	35,625
Medium	375	20	100	$5 \cdot 10^{-5}$	$9.5 \cdot 10^{-5}$	45,000
Fine	375	20	150	$1.5 \cdot 10^{-5}$	$3.1 \cdot 10^{-5}$	67,500
Blunt cone						
Coarse	620	25	70	$8.5 \cdot 10^{-4}$	$5.7 \cdot 10^{-4}$	58,900
Medium	620	25	90	$2.8 \cdot 10^{-4}$	$3.3 \cdot 10^{-4}$	71,300
Fine	620	35	120	$8.6 \cdot 10^{-5}$	$5.7 \cdot 10^{-5}$	96,100

The wall heat flux, of greatest interest for the present study, is a gradient-based quantity inherently more difficult to predict than, for instance, the pressure (Candler, 2018). It is thus a suitable diagnostic quantity for the mesh validation. The results of the grid independence study carried out for the hemisphere-cylinder mesh are presented in Fig. 3.2. The relative errors

between the computed heat fluxes and the results of the finest mesh are shown in Fig. 3.2(a). It can be seen that the relative error is everywhere below 0.5% when going from the medium to the fine mesh. With all meshes, as shown in Fig. 3.2(b), the normal wall unit y^+ is everywhere below 1 so that the flow in the vicinity of the wall is well resolved. Even if the $y^+ < 1$ condition is not as critical as for turbulent simulations which require proper resolution of the viscous sublayer, it is achieved here at moderate computational cost and also enable to carry out computations for higher Reynolds number without changing the mesh. The results for the blunt-cone mesh are presented in Fig. 3.3 and similar conclusions can be drawn.

From this analysis, the medium mesh is considered to give sufficient grid resolution for a reasonable computational time and is thus kept for further computations in this study.

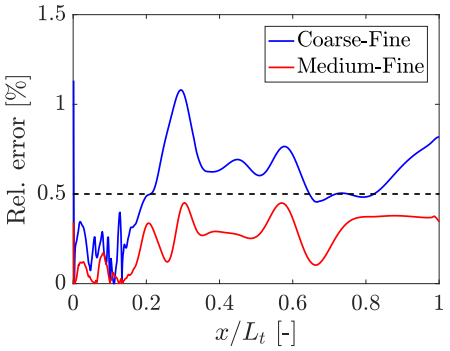

(a) Relative error of heat-flux distributions along the body surface with respect to the finest mesh.

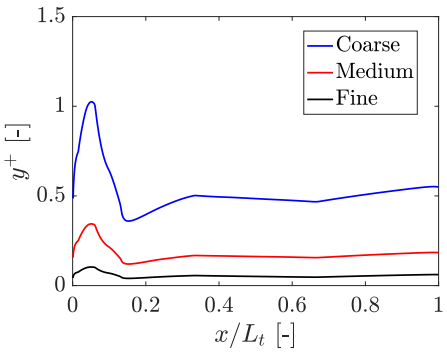

(b) First cell y^+ evolution along the body surface.

Figure 3.2: Results for the grid independence study of the hemisphere-cylinder mesh.

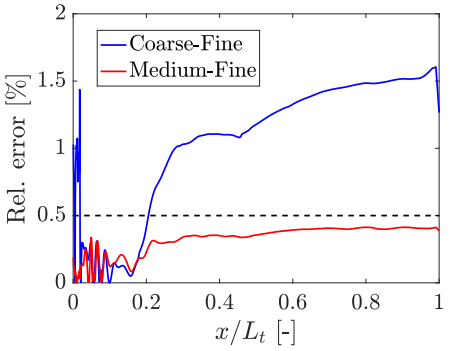

(a) Relative error of heat-flux distributions along the body surface with respect to the finest mesh.

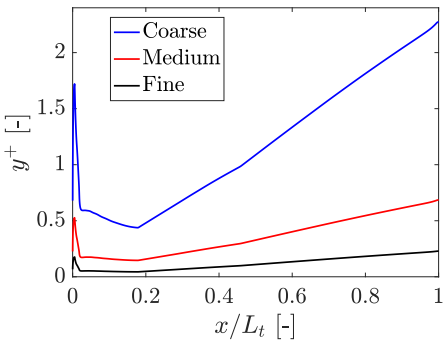

(b) First cell y^+ evolution along the body surface.

Figure 3.3: Results for the grid independence study of the blunt-cone mesh.

3.3.3. Final meshes

The selected structured meshes for the hemispherical cylinder and the 7.4° blunt cone respectively consist of 45,000 and 71,300 quadrilateral cells. A close-up of these meshes on the

nose region is shown in Fig. 3.4(a) and Fig. 3.4(b). It can be seen that the requirements listed in § 3.3.1 have been respected. Fig. 3.4 well illustrates the refinement of the meshes near the shock wave and at the wall.

The good quality of the final meshes has also been checked in Tecplot 360. Maximum cell aspect ratios of respectively 200 and 60 for the hemisphere-cylinder and the blunt cone are found at the solid boundary due to the meshing requirements of the boundary layer. The minimum face areas are respectively $5.9 \cdot 10^{-11}$ m^2 and $2.9 \cdot 10^{-11}$ m^2.

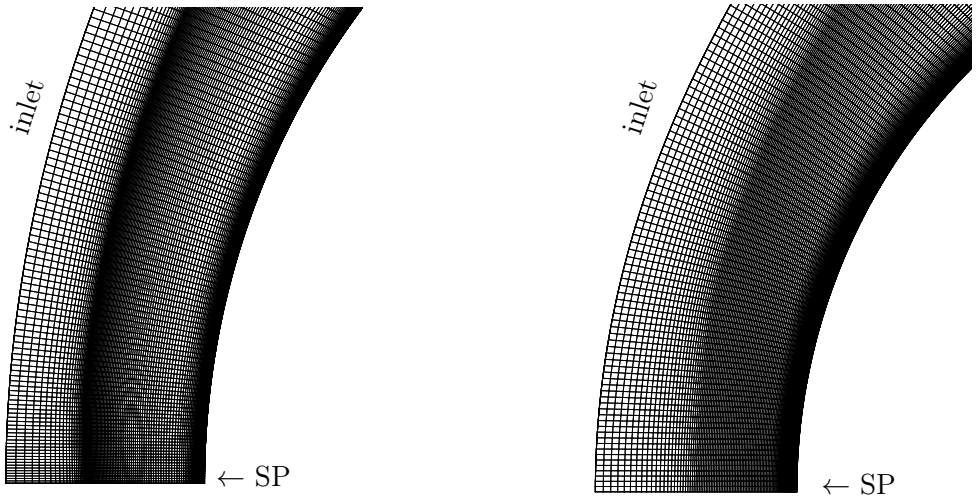

(a) Hemispherical cylinder ($R_n = 20$ mm). **(b)** Blunt cone ($R_n = 3.5$ mm).

Figure 3.4: Computational mesh: close-up near the stagnation point (SP).

3.4. Numerical results

To end up this numerical chapter, this section presents some standalone results from the CFD computations. The heat-transfer results will be compared with theoretical and experimental values in Chapter 5. Note that it was not possible to find in the literature higher-fidelity data for the same test conditions and numerical setup that would have allowed to perform a rigorous validation of the numerical results. Nonetheless, CFD++ is a robust commercial software widely used in VKI and has proven to efficiently solve compressible flows.

The typical flow fields around the two geometries for the medium-Reynolds-number regime ($\mathrm{Re}_{\mathrm{unit},\infty} = 17 \cdot 10^6$ m^{-1}) are shown in Fig. 3.5 and 3.6 with iso-Mach contours. In both cases, the detached shock wave is well recognizable by the strong change in Mach number from its free-stream value ($\mathrm{M}_\infty = 6$) to lower post-shock values. The typical regimes behind the bow shock are well marked: strong normal shock at the stagnation point with subsonic region extending to some portion of the nose and weakening shock as flowing away from the stagnation point.

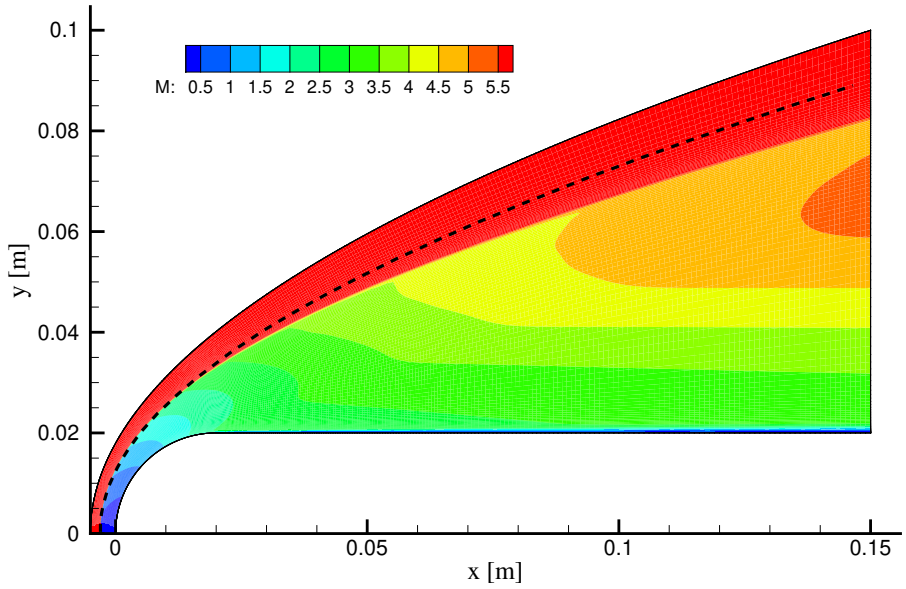

Figure 3.5: Computed flow field around the hemispherical cylinder with Mach-number isolines for the medium-Reynolds-number regime. The dashed line is the shock-shape estimation from Billig (1967).

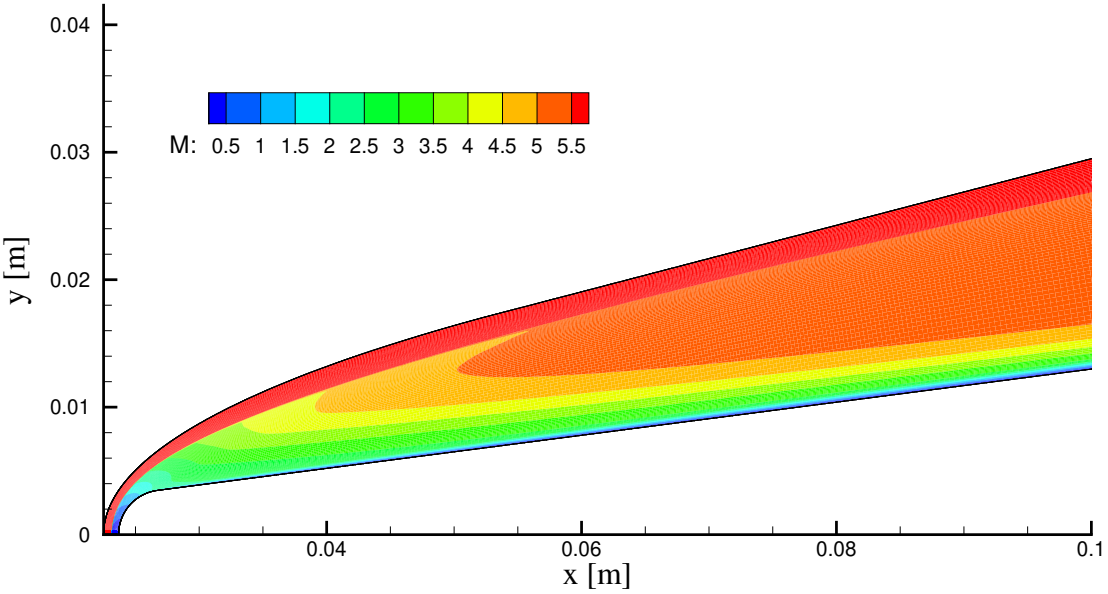

Figure 3.6: Computed flow field around the blunt cone with Mach-number isolines for the medium-Reynolds-number regime (domain extending further downstream not entirely shown).

In Fig. 3.5 is also shown in dashed line the position of the shock wave as estimated by Billig (1967). The latter provided an initial rough estimate comparing well with the final computed shock position in the nose region, but with a lesser agreement on the aft part.

In the case of the blunt cone, the entropy-layer swallowing distance (distance along the body where the entropy layer has been completely swallowed by the thickening boundary layer, see Fig. 2.3) can be estimated from the paper of Rotta (1966). The proposed correlation expresses that this distance increases with increasing free-stream unit Reynolds number and nose radius and decreasing cone half-angle. For the present 7.4° cone of 3.5 mm in nose radius at Mach 6 and at $\mathrm{Re}_{\mathrm{unit},\infty} = 17 \cdot 10^6$ m^{-1}, $s_{\mathrm{swallow}} \approx 888$ mm is obtained. This large value means that the bluntness effects are felt far downstream of the nose, well beyond the end of the cone. It is approximately at this distance that the boundary-layer edge properties approach the theoretical sharp-cone values.

The pressure profiles along the stagnation streamline are presented in Fig. 3.7 for the two geometries. The profiles show an evolution from constant free-stream values p_∞ to the values at the wall, through the nearly discontinuous jumps corresponding to the detached shock waves. The latter are not perfect discontinuities and are distributed over few cells that have been refined on purpose. The non-dimensional shock stand-off distance Δ/R_n can be estimated from these pressure rise and the agreement between the hemispherical cylinder and the cone is very good. The first guess $\Delta/R_n \approx 0.15$ from van Dyke (1958) was rather close. As expected, the shock stand-off distance is independent of the Reynolds number. However, the pressure plateau after the shock wave is naturally proportional to $\mathrm{Re}_{\mathrm{unit},\infty}$. It would have been interesting to compare the computed shock stand-off distance and shock shape with estimations from schlieren pictures. This is another goal that could not be achieved due to the H3 technical problem.

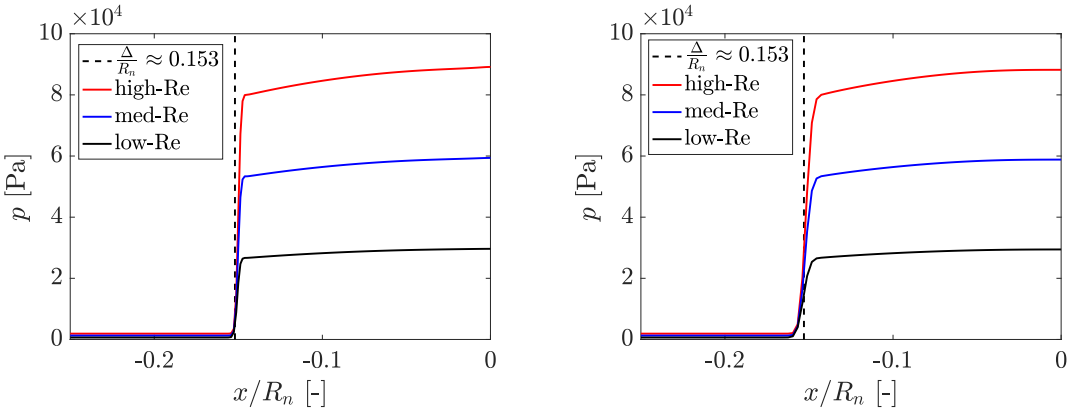

(a) Hemispherical cylinder. **(b)** Blunt cone.

Figure 3.7: Pressure profiles along the stagnation streamline for different Reynolds-number regimes ($8 \cdot 10^6$ /m, $17 \cdot 10^6$ /m, $25 \cdot 10^6$ /m). The stagnation point is located at $x = 0$.

4. Experimental setup

This chapter is the core part of this work and is dedicated to the experimental setup for the investigation of heat transfer over hypersonic vehicles using infrared thermography. It provides a detailed description of the experimental methodology put in place to prepare a successful wind-tunnel testing campaign. The technical issue that made the wind tunnel inoperable does not call into question the relevance and importance of this chapter for the development of a rigorous experimental approach that could be exploited and consolidated for future heat-transfer studies in hypersonic facilities.

In the first section, the wind tunnel in which experiments have been carried out is introduced. Secondly, the infrared measurement technique and its application for the present work is investigated in details. Then, the third section explains how the infrared data can be processed to yield heat-transfer maps. The test models are finally presented.

4.1. The VKI H3 facility

Experiments have been performed in the H3 hypersonic wind tunnel of the von Karman Institute for Fluid Dynamics (VKI). A general description of the facility is firstly given (the interested reader can find further details about the facility, its components and operation in Vanhée (1989), Simeonides (1990), and Masutti (2013)). Secondly, several aspects of the characterization of the hypersonic flow are presented.

4.1.1. General description

The VKI H3 wind tunnel (Fig. 4.1) is a blow-down facility equipped with an axisymmetric contoured nozzle producing a uniform Mach 6 free jet of 120 mm in diameter. Dry air is supplied from a 40-bar reservoir at stagnation pressures ranging from 6 to 35 bar. To avoid condensation in the test section, the supply air is heated in a storage heat exchanger before entering the settling chamber, with a maximum stagnation temperature of 550 K. The resulting free-stream unit Reynolds number of the flow typically varies within 6×10^6 to 30×10^6 m^{-1}. A supersonic ejector exhausting into the atmosphere is used to provide the suction at the downstream end of the diffuser required for starting and running the tunnel at Mach 6. The test chamber is vacuumed prior to each test, whereupon the fast-acting valve opens to allow the high-pressure air to flow through the heat exchanger into the tunnel settling chamber and to expand through the nozzle into the test section. A fast-injection mechanism is then used to place the models in the flow once the free jet is fully established, in order to avoid blockage and excessive heating of the model during start-up. Typical injection time is of the order of 0.1 sec. The facility is

also equipped with a three-degree-of-freedom traversing mechanism for model or probe support allowing the angle of attack to vary between ±5°.

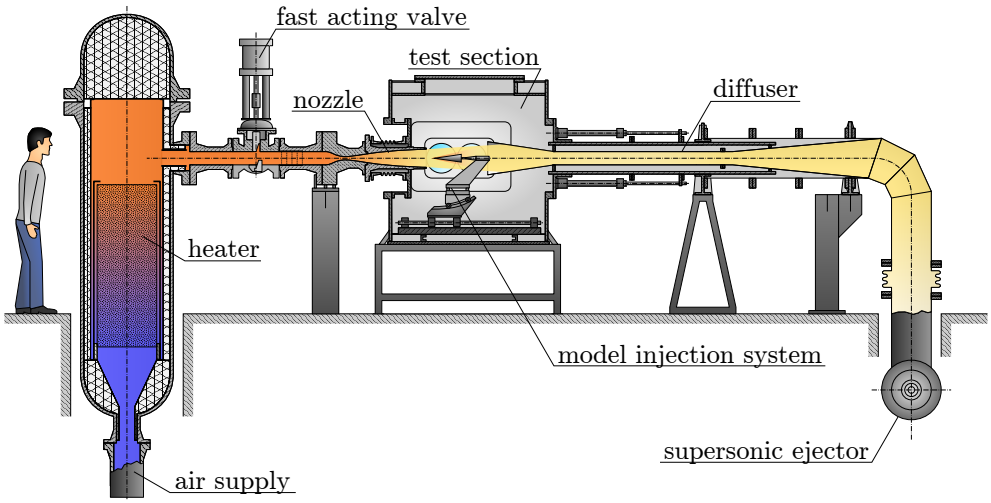

Figure 4.1: Sketch of the VKI H3 Mach 6 wind tunnel.

Among the various experimental techniques available in the H3 wind tunnel, infrared thermography is of interest to the present study. Infrared measurements are rendered possible thanks to an 80-mm-diameter germanium window installed in the side wall of the tunnel test chamber at a distance of 0.6 m of the flow axis. This optical window is coated on both sides with an anti-reflection film to improve its infrared transmission factor.

4.1.2. Flow characterization

Hypersonic nozzle flow characterization is a fundamental task in wind-tunnel testing to obtain high-fidelity measurements. It encompasses the measurement of stagnation temperature and pressure, the determination of free-stream properties, the study of the flow uniformity and the disturbance levels. The experimental procedure followed to measure reservoir conditions and to infer free-stream properties is first explained. Then, the main results of past studies about Mach number uniformity and disturbances levels in the H3 tunnel are presented.

Reservoir conditions

The test conditions in every run are determined from the nominal test-section Mach number used in conjunction with the measurement of the pressure and temperature in the settling chamber. p_0 and T_0 are respectively measured with a WIKA S-20 pressure transmitter and a type K (chromel-alumel) thermocouple. Since any error on p_0 and T_0 will propagate through the whole measurement and computation chain (see § 5.3), it is crucial to correctly relate the output voltages of these instruments to the actual reservoir pressure and temperature.

The calibration law for the pressure transducer is provided by the manufacturer (WIKA, 2014), with an uncertainty of ±0.125% at full scale ($p_{\max} = 40$ bar).

It was not possible to calibrate in-situ the thermocouple with an oil bath and a mercury thermometer, as done in § 4.2, because of the high measured temperatures and the boiling limit of oil. It would be incorrect to extrapolate the calibration established in § 4.2 for the different temperature range related to T_0. Thus, the present measurements rely on the standard calibration relation for type K thermocouples, as implemented in the NI 9211 acquisition module that records the thermocouple output during the test. The type K is the most common type of thermocouple, measuring temperatures up to +1250°C with a sensitivity of 40 µV/°C at room temperature (see NIST web page). For $T_0 \approx 227$°C (500 K), a typical measurement error of ±1.2°C is given by the thermocouple input module (NI 9211 data sheet).

As remarked by Agostinelli (2018), despite some small fluctuations, a more or less constant p_0 can be maintained for about 30 seconds, which is well above the test duration for infrared thermography. In contrast to the total pressure, which is controlled by the operator, the total temperature cannot be set directly to a prescribed value. The exchanger is pre-heated a few hours before the experimental sequence, but cools down during each tunnel run and thus has to be re-heated after some tests. This limitation emphasizes the importance of accurately measuring the instantaneous stagnation quantities during the test with the aforementioned sensors.

Free-stream conditions

The free-stream conditions are determined by the measurement of p_0 and T_0 along with the assumption of an isentropic expansion through the nozzle up to a uniform Mach 6 flow ($\mathrm{M}_\infty = 6$). The isentropic relations are gathered in the NACA report 1135. As said in § 2.1, in the H3 tunnel, the assumption of a thermally and calorically perfect gas is used. Thus, $h = c_p T$, $\gamma = c_p/c_v = 1.4$ and $R = 287$ J/(kg · K) for dry air can be used in H3 test-section conditions.

The free-stream temperature and pressure are respectively given by

$$T_\infty = \frac{T_0}{1 + \frac{\gamma-1}{2}\mathrm{M}_\infty^2} \tag{4.1}$$

and

$$p_\infty = \frac{p_0}{\left(1 + \frac{\gamma-1}{2}\mathrm{M}_\infty^2,\right)^{\frac{\gamma}{\gamma-1}}}, \tag{4.2}$$

while the density is inferred from the ideal gas law

$$\rho_\infty = \frac{p_\infty}{R\, T_\infty}. \tag{4.3}$$

Once T_∞ is known, the dynamic viscosity can be calculated using Sutherland's law, written in a general form for the variable χ as

$$\chi = \chi_{\mathrm{ref}} \left(\frac{T}{T_{\mathrm{ref}}}\right)^{\frac{3}{2}} \frac{T_{\mathrm{ref}} + S}{T + S}. \tag{4.4}$$

Here, the variable $\chi = \mu$ and the coefficients of Eq. 4.4 are $\chi_{\mathrm{ref}} = \mu_{\mathrm{ref}} = 1.716 \cdot 10^{-5}$ kg/(s · m), $T_{\mathrm{ref}} = 273.15$ K and $S = 110.4$ K. This law is a curve fit designed for temperatures above 100 K. Below this value, other viscosity laws, such as Keyes' one, might be better suited, though no significant difference was observed and judged valuable for this study.

The velocity can be obtained using the definitions of Mach number and speed of sound,

$$u_\infty = \mathrm{M}_\infty a_\infty = \mathrm{M}_\infty \sqrt{\gamma R T_\infty}. \tag{4.5}$$

The Reynolds number at infinity based on a unitary length is thus

$$\mathrm{Re}_{\mathrm{unit},\infty} = \frac{\rho_\infty u_\infty}{\mu_\infty}. \tag{4.6}$$

Three typical H3 operating conditions are defined in Table 4.1. Assuming a reservoir temperature $T_0 \approx 500$ K, different unit Reynolds numbers can be achieved by varying the reservoir pressure. These theoretical conditions are referred to in this study as low-Re, medium-Re and high-Re conditions.

Table 4.1: Typical VKI H3 operating conditions.

p_0 [bar]	$\mathrm{Re}_{\mathrm{unit},\infty}$ [m^{-1}]	condition
10	$\approx 8 \times 10^6$	low
20	$\approx 17 \times 10^6$	medium
30	$\approx 25 \times 10^6$	high

A better representation of the true H3 operating conditions is given in Fig. 4.2, which displays contours of $\mathrm{Re}_{\mathrm{unit},\infty}$ for a given (p_0, T_0) combination. The three typical test conditions of Table 4.1 are highlighted by the three colored dots. The total temperature is limited to the left by the condensation boundary. The white hatched region corresponds to liquefied air and is to reject from the H3 operating conditions. The saturation line for air in terms of free-stream static temperature and pressure was taken from the data set compiled by Daum and Gyarmathy (1968). As an example, operating the VKI H3 Mach 6 at $p_0 = 35$ bar, a minimum total temperature of 483 K is required, which justifies the need for the heat exchanger.

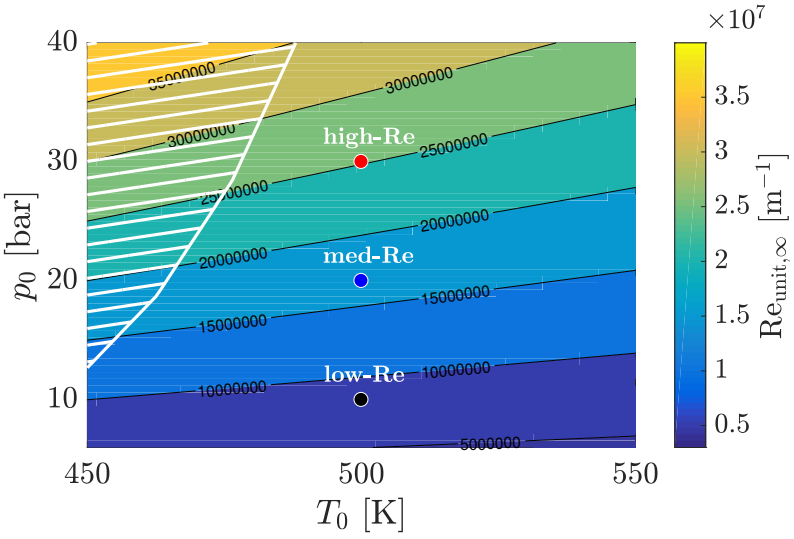

Figure 4.2: Map of the VKI H3 operating conditions with three typical test conditions and air-liquefaction boundary highlighted.

Flow uniformity

Although the VKI H3 nozzle has been designed to provide a uniform Mach 6 jet, the free-stream Mach number in the test section shows some spatial variations. The flow-field non-uniformities in the test section may come from the settling chamber, the model, the surroundings and the tunnel walls (Silvestri, 2003, van den Abbeele, 1996). Calibration of the wind tunnel thus needs to be regularly performed to assess the flow uniformity, which is the first major concern of any experiment. Several calibrations of the VKI H3 have been reported in the past, with main contributions of Kordulla (1970), Vanhée (1989), Boerrigter (1993), Masutti (2013) and Agostinelli (2018).

Boerrigter (1993) showed that the flows in the horizontal and vertical plane are almost the same and the tunnel is rather axisymmetric close to the centerline, but this axisymmetry vanishes at some distance away from it. Some typical iso-Mach lines from his work are shown in Fig. 4.3. His calibration results were overall very close to those of Vanhée (1989). Both authors highlighted the tendency of non-uniformities to concentrate along the nozzle axis. At a distance of 100 mm from the nozzle exit, the Mach number was found to vary between 5.92 and 6.07 in the outer region away from the center of the jet.

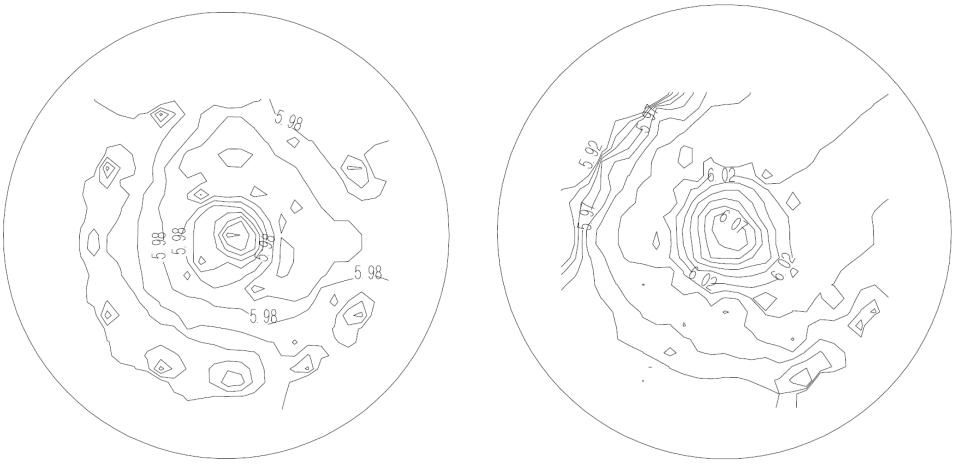

(a) At 10 mm behind nozzle exit. **(b)** At 100 mm behind nozzle exit.

Figure 4.3: Mach-number isolines at different locations from nozzle exit (Boerrigter, 1993).

In their review of the flow characterization of the VKI H3, Grossir et al. (2015) showed that the Mach number diminished at the sides of the jet core from 80 mm downstream of the nozzle exit, sign of an overexpanded jet. The Mach number uniformity in the horizontal plane is shown in Fig. 4.4(a), from the work of Masutti (2013). The boundaries of the free jet are closing in with distance from the nozzle exit. The consequent shrinkage in the uniform flow diameter, illustrated in Fig. 4.4(b), constrains the length of the models to be injected in the flow. This uniform flow diameter is in accordance with the other calibrations of the wind tunnel.

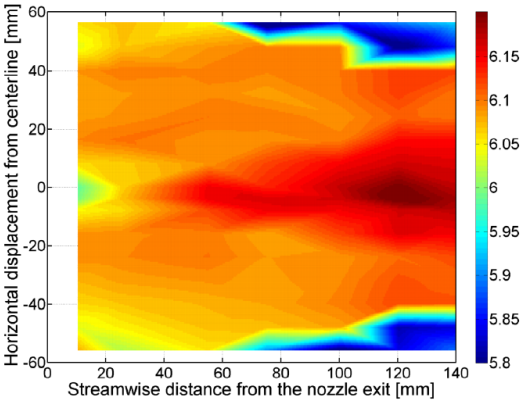

(a) Mach-number uniformity in the horizontal plane, $\mathrm{Re}_{\mathrm{unit},\infty} = 18 \cdot 10^6$ /m (Masutti, 2013).

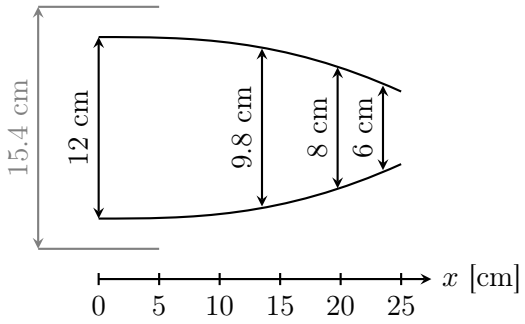

(b) Evolution of uniform test core in the H3 section, redrawn from Simeonides (1990).

Figure 4.4: Mach-number uniformity and jet-core dimensions.

More recently, Agostinelli (2018) carried out a detailed study of the facility characterization and determined the variation of Mach number throughout the test chamber by varying total flow conditions (T_0, p_0). His results were in fair agreement with previous calibrations, showing a good flow uniformity no matter the Reynolds number, with a maximum deviation from the nominal Mach number of 2% localized along the centerline, where strong gradients in the streamwise direction were most observed. Hence, to avoid this non-uniformity, it is recommended to place models 10 to 20 mm away from the centerline, as far as possible and provided the models are small. Agostinelli also discouraged placing models just behind the nozzle and for 20 mm away from it. He advised mounting the models at least 40 mm behind the nozzle exit to obtain more uniform flow conditions.

Moreover, in its investigation about the blockage effect, Agostinelli concluded that the closer the model is to the catch cone of the diffuser, the better the efficiency of the latter. The analysis also revealed that a free-jet length of 240 mm (distance between nozzle exit and diffuser inlet) seemed to be the best trade-off between the necessity of having enough space for the models and the diffuser efficiency requirements.

Calibrations of the H3 have been performed for different sets of flow conditions in order to examine the variation of Mach number over the complete operating range of the tunnel, i.e., from the lowest Reynolds number to the largest one. Boerrigter (1993) noted that the measurements at 10 bar (resp. 30 bar) showed the same flow-field behavior as those at 20 bar, but with an overall Mach number slightly lower (resp. higher). The most likely reason for this is the fact that the boundary-layer displacement thickness in the nozzle exit is larger for lower stagnation pressures, thus creating a smaller effective nozzle area and smaller Mach number. However, the differences are about $\mathrm{M}_\infty \pm 0.02$, which is of the same order as the uncertainty on the Mach number. Boerrigter thus concluded that the measurements at 20 bar could be considered as representative for the general flow field in the tunnel. Later on, Agostinelli (2018) observed the same behavior, founding only a weak correlation between average Mach number and total flow conditions. It was also found that the boundaries of the free jet close more rapidly for lower stagnation pressures.

To sum up, a comparison of these different calibration-campaign results is presented in Fig. 4.5. The concentration of non-uniformities along the centerline is clearly visible, as well as the closing boundaries of the free jet. The data of Agostinelli (2018) are close to those of Kordulla (1970) and both are shifted downward compared to ones reported by Masutti (2013) and Vanhée (1989), which are in fair agreement with each other. Since the test conditions (p_0 and T_0) were similar between the different studies, Agostinelli attributed these shifts to different free-jet lengths and Pitot rakes used. The free-jet length affects the diffuser operation, while different models cause different blockage effects, both leading to different test-chamber pressures. Nonetheless, the shape and the symmetry of all curves are consistent.

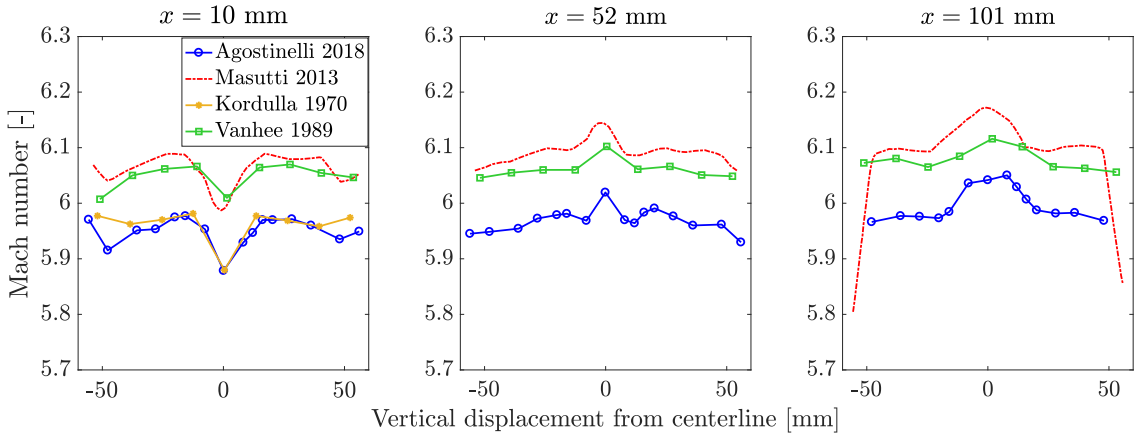

Figure 4.5: Comparison of free-stream Mach-number vertical profiles in the VKI H3 at different locations x from the nozzle exit with previous calibration data from Agostinelli (2018), Masutti (2013), Vanhée (1989) and Kordulla (1970).

Free-stream disturbance levels

In addition to Mach number non-uniformity, free-stream disturbance levels can affect the flow quality and are of great interest for boundary-layer transition studies. The characterization of the free-stream disturbance environment in the H3 hypersonic tunnel has been the subject of several investigations over past years (Grünberg, 2008, Spinosa, 2010, Masutti et al., 2012, Grossir et al., 2015). In the work of Grossir et al. (2015), the attention was placed on the characterization of the free-stream noise levels with double hot wires and stagnation pressure probes. The measured disturbance levels indicated normalized fluctuating values of 0.8% and 1.7% respectively for the total temperature and Pitot pressure, while the normalized mass-flow fluctuations were about 5%. These disturbance levels remain one order of magnitude larger than the so-called quiet wind tunnels or real flight conditions (Schneider, 2008). The study of Grossir et al. (2015) also concentrated on modal analysis and a N-factor of about 5.5 was inferred for the VKI H3, as for similar conventional hypersonic wind tunnels. The larger the N-factor, the better the flow quality. Masutti et al. (2012) concluded that the VKI H3 is a conventional noisy wind tunnel (dominant role of sound-wave mode) with a low turbulence intensity. Disturbances in the free-stream of a hypersonic wind tunnel indeed mainly arise from sound waves radiated from the turbulent boundary layer developing on the nozzle walls (Laufer, 1961).

4.2. Infrared thermography

Infrared (IR) thermography represents a powerful optical tool to observe the temperature history of a test article. This technique has been successfully employed in blow-down facilities such as the VKI H3 wind tunnel to provide quantitative heat-transfer measurement and qualitative flow visualization. The use of an infrared camera as a temperature transducer for heat-transfer studies appears very valuable compared to standard techniques, since it is non-intrusive and provides two-dimensional thermal maps with high sensitivity and a fast response time. It offers a wide variety of experimental opportunities to aerothermodynamic researchers, especially in the field of atmospheric entry problems (Asma et al., 2008).

4.2.1. Basic Principles

Radiative heat transfer

The foundation for IR thermography is that all bodies with a temperature above 0 K emit thermal radiation due to molecular agitation. The energy of the radiation field is transported by electromagnetic waves without requiring the presence of a material medium. The body which emits and absorbs the greatest amount of radiation at an absolute temperature T is called a black body. The rate at which this energy of wavelength λ is released in all directions per unit area and per unit wavelength is termed the spectral hemispherical emissive power E^b_λ [W/m$^2\mu$m] and is given by Planck's law

$$E^b_\lambda(\lambda, T) = \frac{C_1}{\lambda^5(e^{C_2/\lambda T} - 1)}, \tag{4.7}$$

where $C_1 = 3.7418 \times 10^{-16}$ W $\cdot$ m^2 and $C_2 = 1.4388 \times 10^{-2}$ m $\cdot$ K are the universal radiation constants. Curves described by Eq. 4.7 exhibit a distinct maximum at a certain wavelength. This maximum is function of the black-body absolute temperature and can be calculated from Wien's displacement law

$$\lambda_{\max} = 2898/T \ [\mu\text{m}]. \tag{4.8}$$

For ambient temperatures, the maximum of spectral emissive power is in the range $8 - 12$ µm, which corresponds to the operating spectral range of the infrared camera used in VKI. The integration of Eq. 4.7 over all wavelengths yields Stefan–Boltzmann law for the total hemispherical emissive power E^b [W/m^2],

$$E^b(T) = \sigma T^4 \quad \text{with } \sigma = 5.67 \cdot 10^{-8} \text{ W}/(\text{m}^2 \cdot \text{K}^4), \tag{4.9}$$

σ being the Stefan–Boltzmann constant. Since camera detectors only capture a limited band of the whole electromagnetic spectrum, the measurements basically follow Planck's law. The infrared band, of interest for the present study, ranges approximately from 0.75 to 1000 µm and is further sub-divided into four lesser bands: the near infrared ($0.75 - 3$ µm), the middle infrared ($3 - 6$ µm), the long infrared ($6 - 15$ µm) and the extreme infrared ($15 - 1000$ µm).

The black body represents a theoretical and ideal surface behavior that imposes an upper limit to the radiation of real objects, which emit only a fraction of the black-body radiation,

according to

$$E_\lambda(\lambda, T) = \varepsilon_\lambda(\lambda, T) E^b_\lambda(\lambda, T), \tag{4.10}$$

where $\varepsilon_\lambda \leq 1$ is the spectral hemispherical emissivity coefficient. It is a key parameter for radiative heat-transfer evaluation. A body having its emissivity independent of wavelength is called a gray body.

In addition to emitting radiation, an object reacts to incident radiation by different manners. The spectral irradiation G_λ [W/m^{2}µm], the rate at which radiation of wavelength λ is incident upon the surface per unit area and wavelength, in all directions, can be decomposed into a reflected flux, an absorbed flux and a transmitted flux. Conservation of energy requires

$$\begin{aligned} G_{\lambda,\mathrm{ref}}(\lambda) + G_{\lambda,\mathrm{abs}}(\lambda) + G_{\lambda,\mathrm{tr}}(\lambda) &= G_\lambda(\lambda) \\ \rho_\lambda(\lambda) + \alpha_\lambda(\lambda) + \tau_\lambda(\lambda) &= 1 \end{aligned} \tag{4.11}$$

with ρ_λ, α_λ and τ_λ respectively the spectral hemispherical reflectivity, absorptivity and transmissivity. Kirchoff's law states that, at thermal equilibrium, the power radiated by an object must be equal to the power absorbed, that is $\varepsilon_\lambda = \alpha_\lambda$. For non-transparent (opaque) bodies, generally used in IR thermography, $\tau_\lambda \approx 0$. Hence, from Kirchoff's law and Eq. 4.11, materials with low emissivity, such as metallic ones, not only emit less radiation, but also reflect a significant amount of the radiation impinging on them. Thus, they should not be used in IR thermography.

Besides the spectral nature of thermal radiation, real objects do not emit in a pure isotropic way. In practice, the emissivity coefficient depends on both radiation wavelength and propagation direction. For infrared thermography, the spectral dependence of ε is typically removed because of the limited wavelength band captured by the camera detector. For the directional emissivity, conducting and non-conducting materials exhibit two different behaviors, as shown in Fig. 4.6, where θ is the angle between the direction of emission and the normal to the surface (viewing angle). The emissivity of non-conductors, preferred for IR thermography, is practically constant for viewing angles up to 70°, beyond which it falls off sharply with increasing θ. This variation of surface emissivity with viewing angle is one major optical limitation of the IR technique. This issue is typically encountered for measurements on curved bodies such as cones and cylinders. The interpretation of the thermal maps thus needs proper corrections according to the angle θ which has to be accurately known. Nonetheless, in the scope of this work, directional emissivity effects can be ignored since main quantitative data will be extracted along the centerline of the model where viewing angles remain very small (Elbay, 1993, Running et al., 2019).

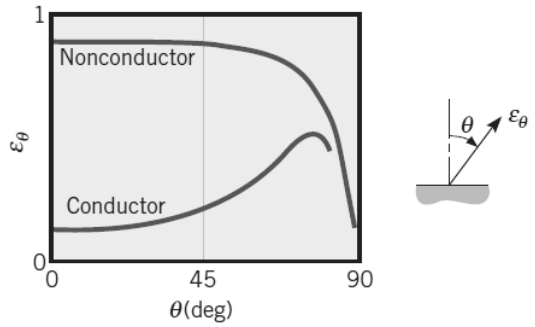

Figure 4.6: Representative variations of the directional emissivity of non-conducting and conducting materials as a function of viewing angle, from Incropera et al. (2012).

Application to IR thermography

The infrared thermograph detects the thermal energy radiated from the object in the IR spectral band and converts it into an electric signal containing the thermal images (thermograms). The output is not directly a temperature, but an intensity proportional to the heat flux radiated from the target. The total incident radiation onto the camera detector can be written as

$$E_i = \left(\varepsilon\tau_{\text{atm}}E^b_{\text{obj}} + (1-\tau_{\text{atm}})\,E^b_{\text{atm}} + \tau_{\text{atm}}(1-\varepsilon)E^b_{\text{sur}}\right)\cdot\tau_{\text{w}}, \tag{4.12}$$

where E^b_{obj} is the radiation emitted by a black body at the object's temperature T_{obj}, E^b_{atm} is the radiation intensity corresponding to a black body at the temperature of the atmosphere T_{atm} between the object and the camera, τ_{atm} is the transmission factor of this atmosphere, and E^b_{sur} is the black-body radiation intensity corresponding to the surroundings inside the test section at temperature T_{sur}. In Eq. 4.12, $\varepsilon\tau_{\text{atm}}E^b_{\text{obj}}$ is the emission from the object, $(1-\tau_{\text{atm}})\,E^b_{\text{atm}}$ is the emission from the atmosphere and $\tau_{\text{atm}}(1-\varepsilon)E^b_{\text{sur}}$ is the radiation emitted by the surroundings and reflected by the object. For the present setup, the presence of the optical window in front of the detector causes all fluxes to be multiplied by the transmission factor of the germanium window τ_{w}. The latter has been estimated in VKI to be approximately 0.85 for the $8-12$ µm spectral range (Simeonides et al., 1993). The overall energy balance is represented in Fig. 4.7.

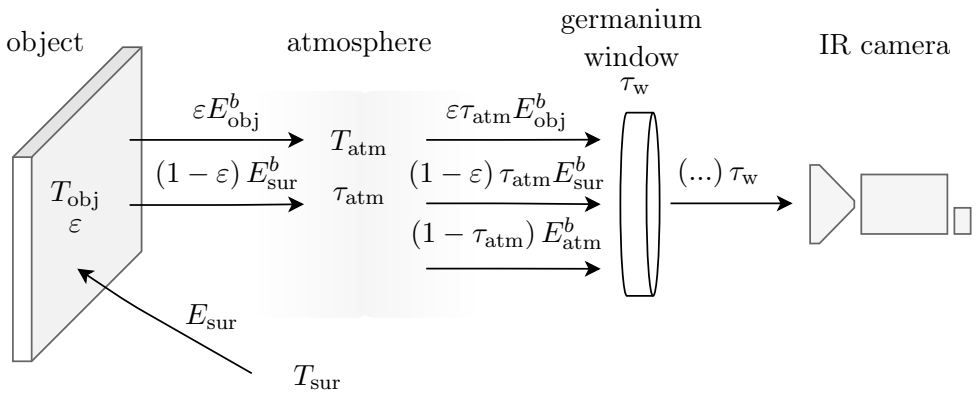

Figure 4.7: Schematic representation of the general thermographic measurement situation, adapted from FLIR (2016).

The energy actually received by the thermograph is thus not only function of the target object and its emissivity, but also depends on environmental conditions. Generally, the transmissivity of the atmosphere τ_{atm} is assumed to be equal to one, since the detector is located at less than one meter from the object and the air is dry (Santarelli and Charbonnier, 1999), therefore greatly simplifying Eq. 4.12.

4.2.2. Present thermograph and calibration

IR camera used in this work

The infrared camera used to capture the wall temperature evolution on the models' surfaces in the present investigation is the FLIR A655sc thermograph (FLIR, 2016). This camera is

equipped with an un-cooled Vanadium Oxide microbolometer detector producing thermal images of 640×480 pixels. The device is able to detect temperature differences as small as 50 mK with measurements accuracy of $\pm 2\%$ of reading. It records 16-bit data at an acquisition frequency of up to 50 Hz at full resolution and has a high-speed windowing function that increases the frame rate up to 200 Hz at a reduced 640×120 pixel window. The FLIR A655sc operates in the $7.5 - 14$ µm spectral range. This long infrared band is characterized by a very low coefficient of atmospheric absorption and higher thermal contrast, thus allowing for high-accuracy measurements (Carlomagno and Cardone, 2010). Further documentation about the FLIR A655sc camera can be found in Appendix B.

Calibration procedure

The calibration procedure of the instruments used in the measurement chain is critical to obtain reliable and accurate thermographic data. The calibration of the IR camera consists in relating the measured flux intensity radiated by the model to a surface temperature distribution. The present calibration follows a two-step process. Firstly, two thermocouples are calibrated with a mercury thermometer of known accuracy. Secondly, the IR camera is calibrated using the two previously calibrated thermocouples.

Thermocouples act as temperature sensors thanks to the thermoelectric effect occurring between their two junctions. Two thermocouples are used for the calibration of the IR camera: one type E (chromel-constantan) and one type K (chromel-alumel) thermocouples, with respective sensitivities of approximately 60 µV/°C and 40 µV/°C (see NIST web page). The calibration setup is presented in Fig. 4.8.

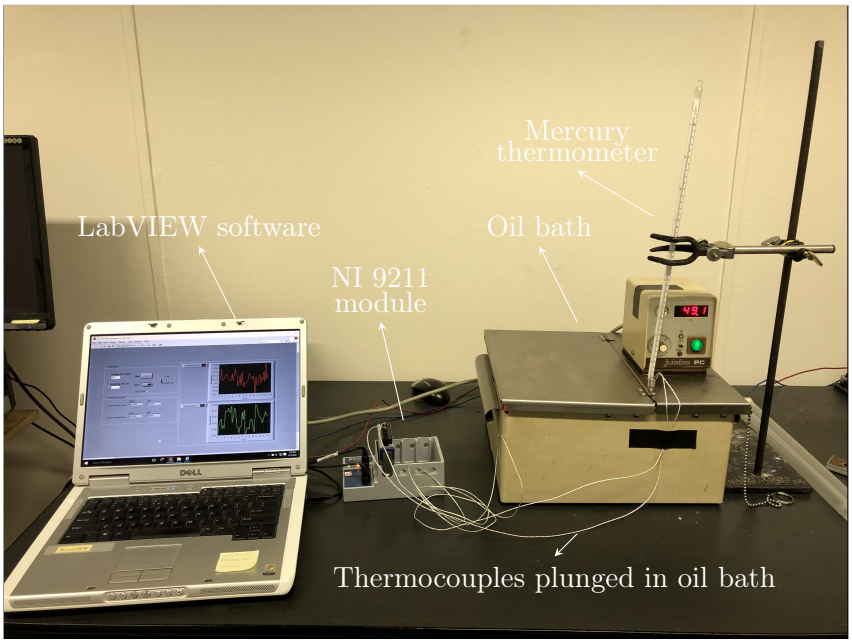

Figure 4.8: Setup for the calibration of the thermocouples.

One junction of each thermocouple is put into a thermo-regulated oil bath whose temperature is measured using a reference mercury thermometer, more reliable than the oil-bath control

unit. The accuracy of the temperature measurements by mercury thermometer corresponds to a half scale, that is 0.05°C. The two immersed junctions are placed very close to the thermometer, while the other junctions are connected to the terminals of the NI 9211 thermocouple input module, which acts as a reference junction of very well-known temperature (NI 9211 data sheet). The data are acquired using LabVIEW (National Instruments, Inc., 2021). The temperature of the bath is successively increased and the outputs of the two thermocouples are recorded once steady conditions are achieved. Due to the lack of an operational cooling system on the oil bath that would require extensive cooling times, only the heating phase is considered, with at least 20 measurement points encompassing the temperature range of interest for the present wind-tunnel investigations (starting from ambient temperature, a typical maximum temperature variation of $\Delta T = 50$ K is expected (Masutti, 2013)).

The thermocouples temperatures (T_{TC}) provided by the acquisition module can thus be linked to the thermometer temperature (T_{TM}), as shown in Fig. 4.9(a) and 4.9(b). Second-order polynomial regressions appear to best fit the data points of each thermocouple, with coefficients of determination R^2 indicating a satisfactory goodness of fit. The repeatability of the measurements has been checked by carrying out the calibration procedure a second time with few measurements encompassing the same temperature range (run 2). The absolute errors with respect to the calibration curves are displayed in Fig. 4.9(c) and 4.9(d) and are of the order of 0.1°C at most.

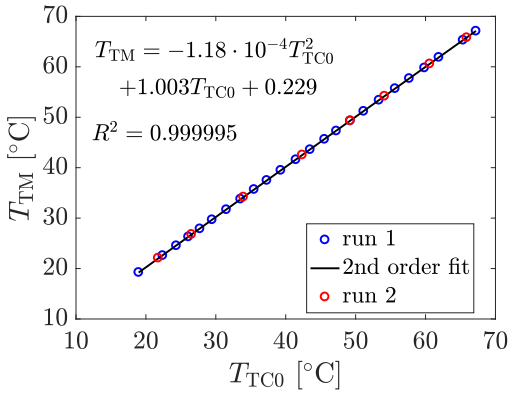

(a) Results for TC0 - type K.

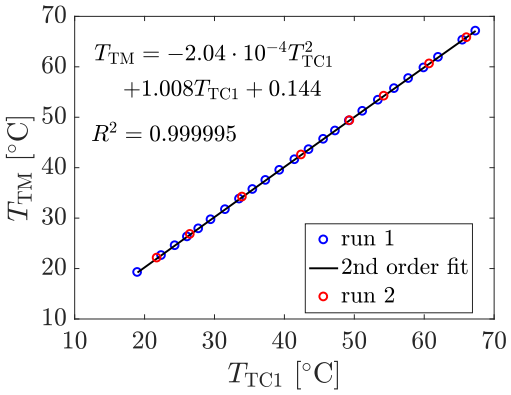

(b) Results for TC1 - type E.

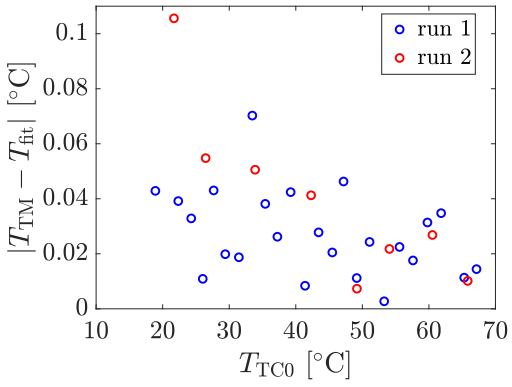

(c) Errors for TC0 - type K.

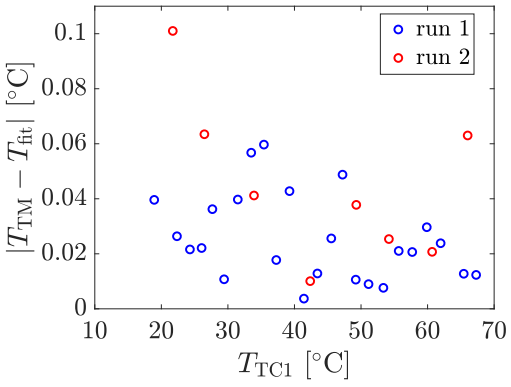

(d) Errors for TC1 - type E.

Figure 4.9: Thermocouples calibration results and absolute errors.

The typical calibration function of an IR camera can be expressed in the following form, derived from Planck's law (Eq. 4.7), where I is the output signal of the camera (proportional to the radiation flux collected by the detector):

$$I(T) = \varepsilon \frac{R}{e^{B/T_{\text{obj}}} - F} + (1 - \varepsilon) \frac{R}{e^{B/T_{\text{sur}}} - F}, \tag{4.13}$$

where R, B, F are constants depending on the complete infrared system, given by the manufacturer. Infrared camera software typically implement this non-linear relation and apply corrections according to Eq. 4.12 to finally obtain T_{obj}. However, this process requires the operator to supply a number of parameters that cannot be easily determined precisely in practice, such as surface emissivity, humidity of air, ambient and surroundings temperatures.

A more suitable approach adopted for the present study is to perform an in-situ calibration using a body with similar properties that will be used during the experiments and in an environment similar to experimental conditions. The calibration thus yields a one-to-one relation between changes in temperature and changes in measured intensity, valid over the studied range of temperature (Boerrigter et al., 1993, Simeonides et al., 1993). The body used for the calibration of the A655sc camera is an electrically heated plate covered with the same[1] black paint as used for the test models. The variable temperature source provided by the plate is measured by the two previously calibrated thermocouples, attached in a region where the heating is the most uniform and separated by few centimeters. The IR camera looks at the small area in between the two thermocouples. The plate is placed in the test chamber so that the camera can look through the germanium window, in order to include its transmissivity and reflectivity losses. The distance between the camera lens and the target object is 98 cm. The calibration setup is presented in Fig. 4.10.

(a) Heated plate with thermocouples.

(b) IR camera looking through the germanium window of the H3 tunnel.

Figure 4.10: Setup for the calibration of the IR camera.

[1] It has been reasonably assumed that the paints are the same.

For each voltage level applied on the plate's electrical resistances, once steady conditions are established, the thermocouples outputs and the average intensity level measured by the IR camera over the small area are recorded. The heat energy collected by the camera detector is transformed into a signal voltage that results in a digital count through the system's A/D converter. For the present IR camera having a 16-bit dynamic range in its A/D converter, count values ranging from 0–65,535 are created over the operating temperature interval of the thermograph (−40°C to +150°C here). The more IR energy incident on the camera's detector, the higher the digital count. The term "IR intensity" is thus used in this study to denote these raw digital data. The calibration laws of each thermocouple are applied, and the average of the two resulting temperatures (mercury thermometer temperature) is considered.

With sufficient data points, the relation between camera intensity and average thermocouple temperature can finally be established. A second-order calibration curve is used to fit the data, as presented in Fig. 4.11. The repeatability of the procedure is demonstrated with complementary data points (run 2) obtained for a different distance between plate and detector (85 cm). The latter parameter is thus shown to have barely any influence on the calibration trend. The independence of the results with respect to the size of the area chosen to average the pixels intensities in between the two thermocouples has also been verified. The area width and height were both varied and the resulting calibration coefficients appeared to vary at most by 0.5% with respect to the original coefficients.

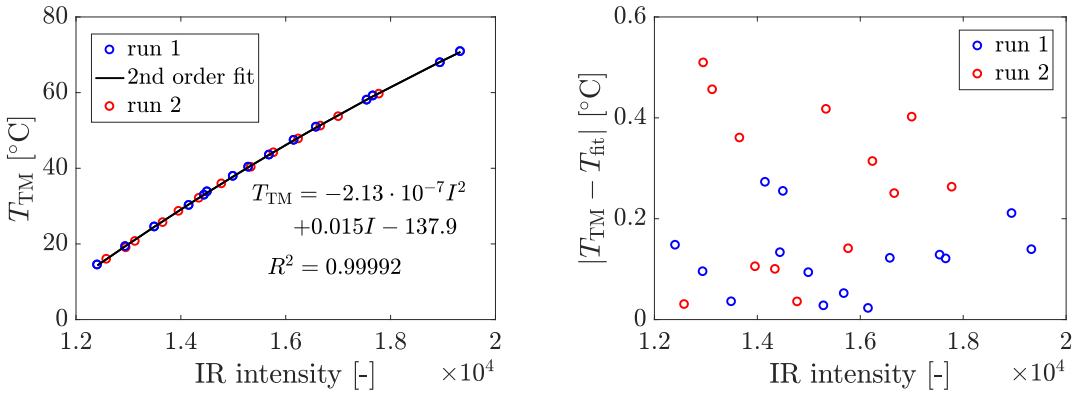

(a) Results and curve fitting. **(b)** Absolute errors with fit.

Figure 4.11: IR camera calibration results and absolute errors.

4.3. Heat-transfer measurement

4.3.1. Data-reduction model

Aerodynamic heating in short-duration hypersonic facilities is not measured directly. Instead, it is extracted after processing of the time-resolved surface temperature measurements through a suitable heat-conduction model. The standard data-reduction model employed for heat-transfer

measurements in the VKI facilities is based on the semi-infinite slab principle. The model relies on the following hypotheses:

- the wall into which heat is conducted is semi-infinite in thickness;
- the heat conduction into the slab is one-dimensional;
- the thermal properties of the slab are uniform and do not depend on temperature.

The data reduction is based on the general differential equation for heat conduction in an isotropic solid (Incropera et al., 2012):

$$\frac{\partial^2 T}{\partial x^2}+\frac{\partial^2 T}{\partial y^2}+\frac{\partial^2 T}{\partial z^2}-\frac{1}{\alpha}\frac{\partial T}{\partial t}=0 \qquad \text{with} \quad \alpha=\frac{k}{\rho c} \quad \text{the thermal diffusivity } [\mathrm{m^2/s}], \tag{4.14}$$

where k is the thermal conductivity $[\mathrm{W/m\cdot K}]$, ρ the density $[\mathrm{kg/m^3}]$ and c the specific heat $[\mathrm{J/kg\cdot K}]$ of the solid model. Under the 1D assumption (along the wall-normal direction y), Eq. 4.14 simplifies to

$$\frac{\partial^2 T}{\partial y^2}=\frac{1}{\alpha}\frac{\partial T}{\partial t}. \tag{4.15}$$

To solve Eq. 4.15 for $T(y,t)$, it is necessary to specify one initial condition and two boundary conditions. The initial condition corresponds to a uniform temperature distribution at time $t=0$:

$$T_w(y,t=0)=T_{w0} \tag{4.16}$$

and the boundary conditions are

$$-k\frac{\partial T(y,t)}{\partial y}\bigg|_{y=0}=\dot{q}_w(t) \quad \text{and} \quad T_w(\infty,t)=T_{w0}, \tag{4.17}$$

the former prescribing the heat flux at the model surface by Fourier's law and the latter assuming that the back surface temperature remains constant with time (there should not be any temperature change far below the surface). Eq. 4.15 can be solved analytically by means of Laplace transforms. The detailed derivation can be found in Schultz and Jones (1973). The solution is

$$\dot{q}_w(t)=\sqrt{\frac{\rho c k}{\pi}}\left[\frac{T_w(t)}{\sqrt{t}}+\frac{1}{2}\int_0^t\frac{T_w(t)-T_s(\tau)}{(t-\tau)^{3/2}}\mathrm{d}\tau\right]. \tag{4.18}$$

Eq. 4.18 involves the numerical integration of the second term in the square brackets. Schultz and Jones (1973) have presented several methods to deal with the singularity at $\tau=t$. Among them, the technique of Cook and Felderman (1966) is employed at VKI. It assumes that $T_s(\tau)$ can be approximated by a piecewise linear function. Finally, after some calculations not reported here, the following expression for the convective heat flux into the model surface is obtained for a discrete time step n:

$$\dot{q}_w\left(t_n\right)=2\sqrt{\frac{\rho c k}{\pi}}\sum_{i=1}^{n}\frac{T_w\left(t_i\right)-T_w\left(t_{i-1}\right)}{\left(t_n-t_i\right)^{1/2}+\left(t_n-t_{i-1}\right)^{1/2}}. \tag{4.19}$$

The Stanton-number distribution on the model can then be inferred from the computed heat fluxes. However, the definition given in Eq. 2.2 is not very convenient for experimental investigations since boundary-layer edge conditions and adiabatic-wall enthalpy are usually not measured. Therefore, Santarelli and Charbonnier (1999) recommended an alternative definition

of the Stanton number which uses free-stream values instead of edge quantities and substitutes the stagnation temperature T_0 to T_{aw}. The expression reads

$$\mathrm{St}_{\mathrm{mod}} = \frac{\dot{q}_w}{\rho_\infty u_\infty c_p (T_0 - T_w)}. \tag{4.20}$$

4.3.2. Limitations

The validity of the three basic assumptions of this data-reduction model is now discussed.

- **Semi-infinite thickness.** Firstly, this ideal behavior can be approached in practice by using an insulating material for the test model, such as Plexiglas in the present study. Secondly, this hypothesis implies that test duration should be limited so that the heat on the surface of the model has no time to be conducted through the whole thickness and reach the other side of the body. The penetration depth, at which the local temperature and heat rates are 1% of their values at the front surface, can be approximated by $y = 4\sqrt{\alpha t}$ according to Schultz and Jones (1973). The authors provided the following rule of thumb for the thickness requirements:

$$\begin{aligned} y\ [\mathrm{cm}] &= 4.0\sqrt{t(s)} \quad \text{for most metals,} \\ &= 0.3\sqrt{t(s)} \quad \text{for insulators.} \end{aligned} \tag{4.21}$$

  Hence, for a 6-mm-thick Plexiglas layer, Eq. 4.21 imposes the heat fluxes to be evaluated within 4 sec after the injection of the model in the wind tunnel.

- **1D heat conduction.** Some transversal/lateral conduction may occur for measurements along curved surfaces and in the neighborhood of the edges of the model. Again, the use of a good insulating material can mitigate these effects and helps meet the 1D hypothesis (Masutti, 2013). Vanhée (1988) even suggested that the transverse-conduction effects can be neglected, except at the junction between the insulating part and the conducting part of the model (see § 4.4.2), where large gradients of temperature may exist.

  Simeonides (1990) proposed simplified forms of the 2D heat equation for heat-flux calculation in regions with large lateral temperature gradients. The latter may arise from specific flow situations, such as reattaching flows and shock-wave boundary-layer interaction. In VKI, Playez (1997) developed a finite-element code for 3D transient heat conduction, but the technique was strongly limited by computational time and was very sensitive to boundary conditions. The study was not advanced enough to draw firm conclusions about the practical use of the procedure which has been left behind since then. Yet, the approach ought to be re-investigated for future IR studies.

  In this work, no effort was made to account for potential transverse-conduction effects.

- **Constant thermal properties** The thermal product $\sqrt{\rho c k}$ may vary due to aerodynamic heating. Simeonides (1990) proposed approximate correction factors to account for temperature changes in $\sqrt{\rho c k}$ for pyrex, quartz and macor. However, since measurements are performed shortly after model injection and since the surface temperature variation range is limited ($\Delta T = 50$ K), Masutti (2013) stated that this third assumption can safely be applied. No reliable data about the variation of Plexiglas' thermal properties with temperature could be found for the present study, though.

The initial condition (Eq. 4.16) also imposes an experimental constraint. The data-reduction model assumes that the heat flux is instantaneously applied from uniform conditions at $t = 0$. This initial condition is represented practically by a reference image taken before the test, with the model injected inside the vacuumed test section without flow. It is thus the change in intensity level (or surface temperature) due to the heating of the model from this reference condition before the actual beginning of the test that is processed by the data-reduction model. The drawbacks of this procedure are that a reference image has to be taken before each test and that two successive tests must be sufficiently distant in time so that the model can cool down and recover a uniform temperature distribution for the initial condition of the next test.

4.3.3. Data processing: IRDA

Under the assumption of 1D heat conduction into a semi-infinite slab, the temperature history of each pixel on the IR images can be processed to calculate the time-resolved surface heat flux and Stanton number, according to Eq. 4.19 and Eq. 4.20. This heat-flux rebuilding procedure has been automated in a MATLAB program named IRDA (InfraRed thermography Data Analysis). This VKI code was initially developed by Strub (2006) for infrared data processing and has been successfully used for several wind-tunnel experiments. However, it has been left behind for some years. Only an incomplete version of IRDA was available for the present study. Hence, the updating and streamlining of the program was also an important task of this work.

The program is composed of several routines and is basically divided into three main parts. Only a brief overview is presented here.

The first part concerns the setting of the test parameters. The inputs required are the infrared images information, the calibration laws, the definition of the computation domain, the model-wall properties and the wind-tunnel test conditions. Regarding the latter input, an improvement of the old code was to account for the true instantaneous total pressure and temperature recorded during the test, instead of assuming a constant p_0 and T_0 for the overall computation. While p_0 remains mostly constant, the variations of T_0 during the test are more significant, as shown in Fig. 4.12.

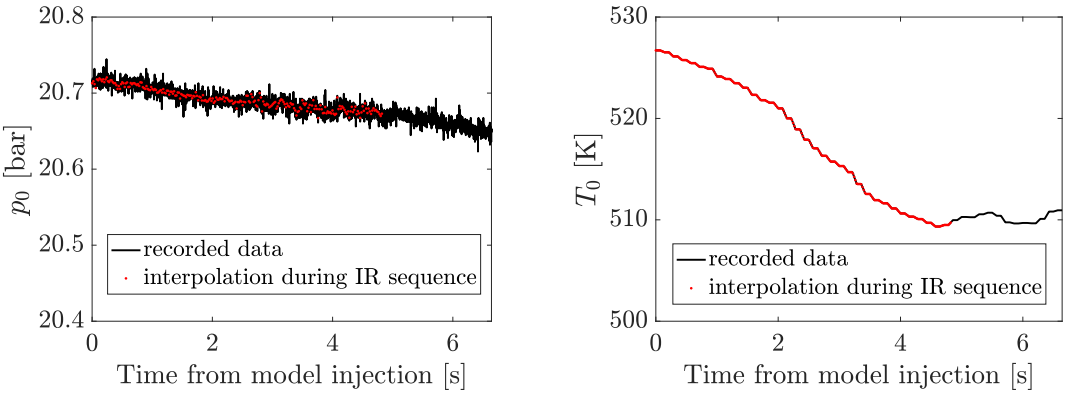

(a) Total pressure. **(b)** Total temperature.

Figure 4.12: Evolution of total-temperature and total-pressure recordings during a typical test at medium-Reynolds-number condition.

For the test case presented in Fig. 4.12, the maximum p_0 difference during the overall recording is 0.6%, while the T_0 exhibits a 3.4% maximum variation. However, a much larger dataset would be required to draw further conclusions. The total temperature is involved in several terms in the expressions of the Stanton number (Eq. 4.20) and Reynolds number (Eq. 4.6). These non-dimensional quantities will be used for results analysis and comparison and thus need to be correctly evaluated.

The second part of the program loads the previous settings and implements Eq. 4.19 for the heat-flux maps over all time steps. The image at which the model is fully injected and stabilized is the first image for which the computation starts. However, the time of this image is not an appropriate starting time for the calculation. The model has already been exposed to heat transfer while crossing the shear layer of the free jet, whereas the heat-conduction model assumes that the heat flux is instantaneously applied. Therefore, it is necessary to define a virtual time origin of the test, from whereon the model would have been instantaneously heated under uniform flow conditions (Strub, 2006, Boerrigter et al., 1993). To do so, the transient intensity at some location on the model is evaluated and the resulting curve is extrapolated to zero intensity. This root is the virtual time origin and the effective time of each thermal image can thus be calculated.

The third and last part of IRDA deals with results plotting. The user can choose the quantity to display (temperature, heat flux, Stanton number), over time or at a particular time instant. Various plotting options are available (line plots, contours, streamwise and spanwise profiles). Of interest in the present investigation is mainly the Stanton-number distribution along the model's centerline, where pixels must be converted into mm. Spatial and temporal filtering can be applied to obtain smoother profiles.

4.3.4. Validation of IRDA code

Besides the intrinsic limitations of the model used for data reduction, one should ensure that the newly updated IRDA code does not contain any error in the calculation of the heat flux. A validation is thus performed by comparing computed results with available exact results. There exists closed-form analytical solutions for the heat-transfer problem into a semi-infinite solid for three limiting cases, where conditions are instantaneously applied at $t = 0$: (i) application of a constant surface temperature, (ii) application of a constant surface heat flux and (iii) exposure of the surface to a fluid a known temperature and convection coefficient (Incropera et al., 2012). The present validation is performed for the first two cases.

Let us first consider case (i) where a constant temperature $T_w \neq T_{w0}$ is instantaneously applied at $t = 0$. The resulting heat flux is given by

$$\dot{q}_w(t) = \sqrt{\frac{\rho c k}{\pi}} \frac{T_w - T_{w0}}{\sqrt{t}}. \tag{4.22}$$

As presented in Fig. 4.13, the computed heat flux well matches the expected analytical result, with better agreement for decreasing time step Δt (inverse of sampling frequency).

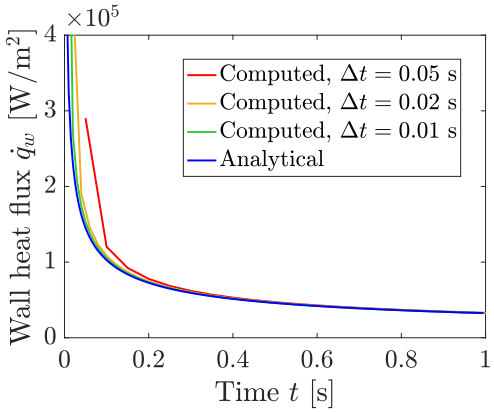

(a) Heat-flux evolution (computed and analytical).

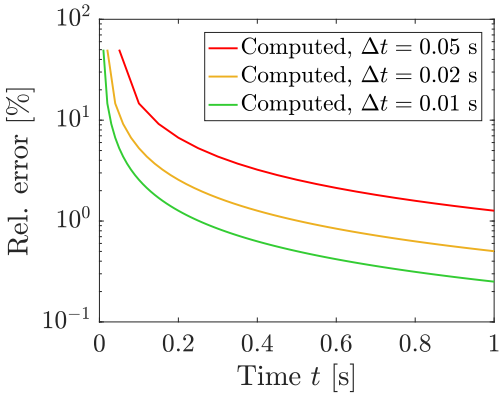

(b) Deviation of computed solution with respect to analytical result.

Figure 4.13: Comparison of computed and analytical heat fluxes for the case of a constant surface temperature instantaneously applied on the semi-infinite solid surface, with $T_{w0} = 300$ K, $T_w = 400$ K and $\sqrt{\rho c k} = 575.4$ kg $\cdot$ K^{-1}s$^{-5/2}$.

For case (ii), where a constant heat flux $\dot{q}_w$ is applied, the surface temperature distribution has the following analytical expression:

$$T_w(t) = T_{w0} + \frac{2}{\sqrt{\pi}} \frac{\sqrt{t}}{\sqrt{\rho c k}} \, \dot{q}_w. \tag{4.23}$$

Hence, imposing such a temperature distribution for some constant $\dot{q}_w$ value and applying the data-reduction algorithm, this constant heat flux should be obtained in output. This is what is observed in Fig. 4.14. Once again, the convergence is faster for small time steps. Interesting information regarding the sampling frequency of the IR camera acquiring the thermal images can be inferred. One can observe that, for a 20-Hz camera, it takes 0.3 sec for the computed heat flux to be less than 1% off from the analytical result. If the camera acquires at 50 Hz, this time drops to less than 0.15 sec. The algorithm thus converges very fast and the results obtained with the present A655sc camera can safely be analyzed shortly after model injection.

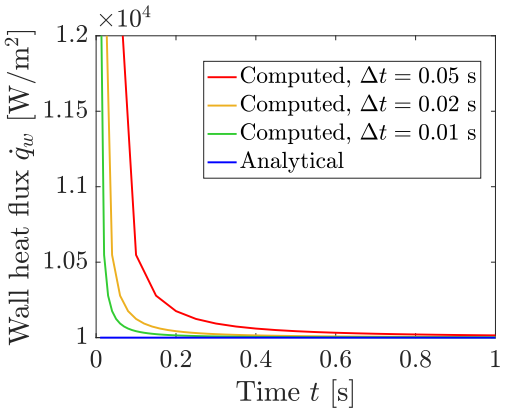

(a) Heat-flux evolution (computed and analytical).

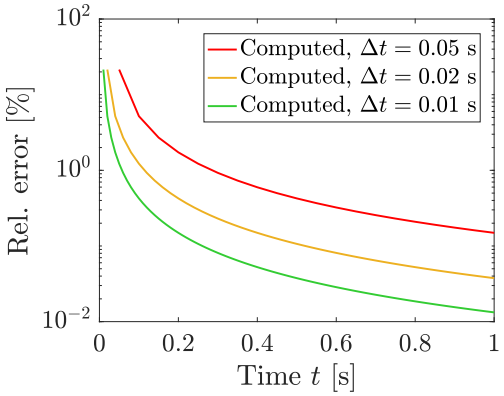

(b) Deviation of computed solution with respect to analytical result.

Figure 4.14: Comparison of computed and analytical heat fluxes for the case of a constant heat flux instantaneously applied on the semi-infinite solid surface, with $T_{w0} = 300$ K, $\dot{q}_w = 10^4$ W/m^2 and $\sqrt{\rho c k} = 575.4$ kg $\cdot$ K^{-1}s$^{-5/2}$.

4.4. Test models

Experiments were planned to be carried out using already existing models available in the H3 laboratory. Besides the time savings associated with the manufacture of new models, the purpose was to assess the ability of the different methods (theoretical, numerical and experimental) to predict the heat-flux distributions on several arbitrary shapes, without restricting the analysis to a specific model.

4.4.1. Geometry

The models that were planned to be tested consist of two simple academic geometries: a hemispherical cylinder and a blunt cone. The hemispherical cylinder is available in one model, while there exist several prototypes for the blunt-cone geometry, with different cone half-angles, nose radii and lengths with respect to the theoretical apex, as illustrated in Fig. 4.15.

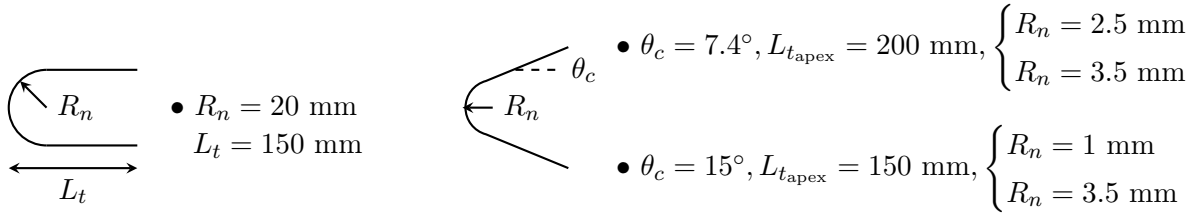

(1) Hemispherical cylinder (2) Blunt cone

Figure 4.15: Test models sketches and geometrical specifications.

These axisymmetric geometries enable two-dimensional analyses, much more suitable from the numerical, theoretical and experimental points of view. The hypersonic flow around such blunt bodies is characterized by a detached bow shock forming in front of the nose, spreading the heat over a larger volume compared to a shock attached to slender bodies (sharp cones, wedges, flat plates). The pioneer theories of Fay and Riddell (1958) and other authors presented in Chapter 2 can thus be applied. Moreover, the boundary layer over these objects is expected to remain laminar, due to the large nose bluntness having a stabilizing effect (see § 2.3). It is not desired to trigger transition to turbulence, hence only the smooth versions (i.e., without roughness elements) of the models are tested. Finally, there have been several studies reported in the literature over such spherical and conical geometries, so that a wealth of useful information is available.

4.4.2. Material

Heat-transfer measurements based on the semi-infinite slab principle and relying on infrared thermography require the careful choice of models material. Hence, there are several good reasons for which the present VKI models have been manufactured in Plexiglas.

Firstly, the selected material should be insulating (low thermal conductivity k) so as to respect the semi-infinite slab assumption and provide high-temperature signals for enhanced accuracy of the measurements. Plexiglas is a very good insulating material (considerably better than quartz or macor (Simeonides, 1990)). Its thermal properties are summarized in Table 4.2.

Table 4.2: Plexiglas properties, from Grossir et al. (2015).

ρ [kg/m^3]	c [J/(kg · K)]	k [W/(m · K)]
1190	1464.4	0.19

Secondly, the model material should have a very low transmittance τ so that the emitted infrared radiation is only generated at the wall. Masutti (2013) showed that the Plexiglas is almost opaque in the $8 - 9$ μm spectral band, which is included in the operating range of the present FLIR A655sc camera. Similarly, a high emissivity in the IR spectrum is desirable to provide the camera with a strong signal and minimize reflections of IR radiation from extraneous sources in the environment. This is why the surface of all models is covered with a special black matte paint that permits to achieve an emissivity close to 1.

However, Plexiglas cannot withstand the high temperatures occurring at the stagnation point (hot shock layer), where the aerodynamic heating is maximum (see § 2.2.1). Therefore, the leading edges of all models are made of steel. With its high thermal conductivity, this metal will limit the temperature rise so that the model can resist the test. Since infrared measurements are only valid over the highly insulating Plexiglas part of the models, it will not be possible to assess experimentally the stagnation-point heat flux. Moreover, the interface between Plexiglas and steel is expected to create side effects (breakdown of the second hypothesis of the data-reduction model) so that heat-transfer measurements in this region should be interpreted carefully.

4.4.3. Interface with wind tunnel

The test models are mounted on the support of the pneumatic injection system, without any angle of attack or yaw. The good alignment of the models with the incoming flow must be ensured. Dieudonne et al. (1997) have shown that the effects of flow misalignment are important, especially on heat transfer. This condition can be qualitatively verified during post-processing by checking the axisymmetry of the temperature maps. Some photographs of the models mounted and injected inside the test section are provided in Fig. 4.16.

(a) 7.4°-half-angle cone. **(b)** 15°-half-angle cone. **(c)** Hemispherical cylinder.

Figure 4.16: Test models mounted and injected inside the test section.

The lateral and vertical positioning of the models inside the test section also deserves some special attention. It has already been noted in § 4.1.2 that streamwise non-uniformities in the flow concentrate along the nozzle axis. The recommendation is therefore to place the model 10 to 20 mm off the centerline with the centerline on the backside of the model (Simeonides, 1990, Boerrigter, 1993, Agostinelli, 2018). Regarding the distance behind the nozzle exit, the current convention is to put the nose of the models 5 mm off, but this practice seems to go against the recommendations of Agostinelli (2018). Unfortunately, due to the H3 technical issue, we were not able to investigate the effects of model positioning as it was intended. Only one sequence of measurement has been achieved, with the 7.4°-half-angle cone equipped with a 3.5-mm-radius nose and located 5 mm behind the nozzle exit, slightly off centerline (4 mm) in the horizontal plane.

The flow field around the model in unconfined conditions is different from the actual flow field inside the closed test section. In the latter conditions, the blockage phenomenon might be encountered when too large models are injected into the flow. The pressure losses due to the model might be too high for the diffuser pressure recovery and this component might become blocked. As noted by Vanhée (1989), "there is no theory to predict the blockage of hypersonic wind tunnels". Nonetheless, from experience in the H3, and as recently confirmed by Agostinelli (2018), blockage is very sensitive to the relative position between the model and the diffuser. Agostinelli (2018) recommended a free jet length of 240 mm for optimal performance of the diffuser and also concluded that the efficiency of the diffuser is better the closer the model is to it. Besides, his results showed that a blockage ratio of 7.7% (ratio between the projected model area and the nozzle exit area) was the maximum permitted to avoid blockage, for capsule-shaped models only. This ratio corresponds to a model diameter of 4.3 cm. In the present study, the free jet length was 240 mm and no blockage phenomenon was encountered for the conical model.

5. Results and discussion

This chapter is dedicated to the analysis and discussion of the heat-transfer results obtained by means of theoretical methods (Chapter 2), Navier–Stokes simulations (Chapter 3) and infrared thermography (Chapter 4). The reader is reminded that a technical issue in the VKI H3 facility prevented us from performing a proper complete experimental campaign.

Section 5.1 first presents stagnation-point heating results from engineering correlations and numerical solutions. Then, off-stagnation conditions are considered in § 5.2. The few experimental Stanton numbers are compared to the theoretical and numerical predictions. Finally, in § 5.3, the uncertainty on the experimental results is assessed.

5.1. Stagnation-point heating

No experimental measurement is available in the stagnation region due to the material constraint explained in § 4.4.2 (nose made of steel). Numerical computations and approximate methods are the available tools to provide estimates of the peak heat fluxes experienced on the noses of the test articles in the H3 facility.

First of all, some heating predictions yielded by the famous Fay–Riddell reference equation (Eq. 2.9) are shown in Fig. 5.1.

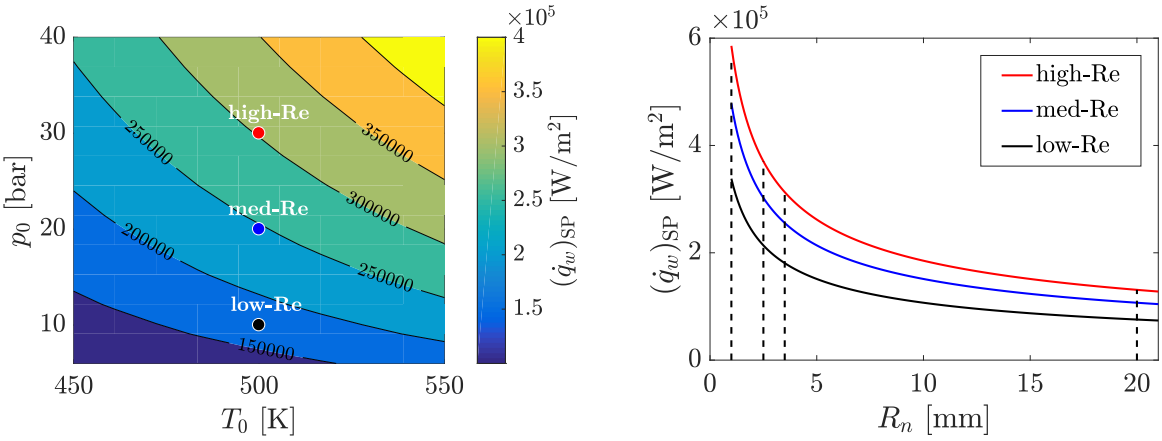

(a) Stagnation-point heating over H3 operating range for $R_n = 3.5$ mm and $T_w = 300$ K.

(b) Effect of R_n and $\mathrm{Re}_{\mathrm{unit},\infty}$ on stagnation-point heating.

Figure 5.1: Fay–Riddell stagnation-point heating results.

Fig. 5.1(a) shows contours of the stagnation-point heat flux $(\dot{q}_w)_{\mathrm{SP}}$ for different T_0 and p_0 and for a spherical nose of 3.5 mm radius (which is the nose radius of the single model experimentally tested). The three typical H3 conditions (low-, medium- and high-Re) are represented by the

three colored dots. It can be observed that it is mainly the stagnation pressure variation over the H3 operating range that dictates the amount of $(\dot{q}_w)_{\mathrm{SP}}$. From the low- to the high-Reynolds-number conditions, the heating rates are twice as large. Peak heating rates of several hundreds of $\mathrm{kW/m^2}$ are encountered.

In Fig. 5.1(b), the dependence of the stagnation-point heat flux with nose radius is clearly shown: $(\dot{q}_w)_{\mathrm{SP}} \propto R_n^{-1/2}$. It directly arises from the definition of the tangential velocity gradient (Eq. 2.8) that appears under a square root in the original equation. The nose radii of the models that were supposed to be tested in this work (Fig. 4.15) are highlighted by dashed dark lines. Peak heating rates are significantly reduced by blunting the nose of the vehicle.

In Fig. 5.2, a comparison between numerical and theoretical stagnation-point heating predictions is made. The stagnation-point heat flux is multiplied by $\sqrt{R_n}$ in order to remove the nose radius dependence. Different free-stream unit Reynolds number are considered. The solid blue line (Fay–Riddell equation) shows the functional relationship between the normalized heat flux and Reynolds number: it is of type $(\dot{q}_w)_{\mathrm{SP}}\sqrt{R_n} = \mathrm{cst} \times \sqrt{\mathrm{Re}_{\mathrm{unit},\infty}}$. The other theoretical correlations (Tauber et al. (1987), Sutton and Graves (1971) and Sagnier and Verant (1998)[1]) are all overestimating the Fay–Riddell prediction. The differences between such correlations has already been quantified in § 2.2.1 and are re-expressed here through relative errors Δ_{FR} with respect to the Fay–Riddell result. The deviations are of the order of 10%. Laminar CFD solutions on the hemispherical cylinder and the 7.4° blunt cone are also displayed. The agreement with the reference Fay–Riddell result is rather good, with deviations of only few percents. The functional dependence of the heat flux with free-stream unit Reynolds number seems to be well respected too. Different nose radii R_n were considered in the numerical simulations to examine if the results would all collapse on a single value $(\dot{q}_w)_{\mathrm{SP}}\sqrt{R_n}$. As can be seen in the graph, the agreement is not perfect. In fact, the numerical heat fluxes seem to be proportional to a power of R_n slightly below $-1/2$.

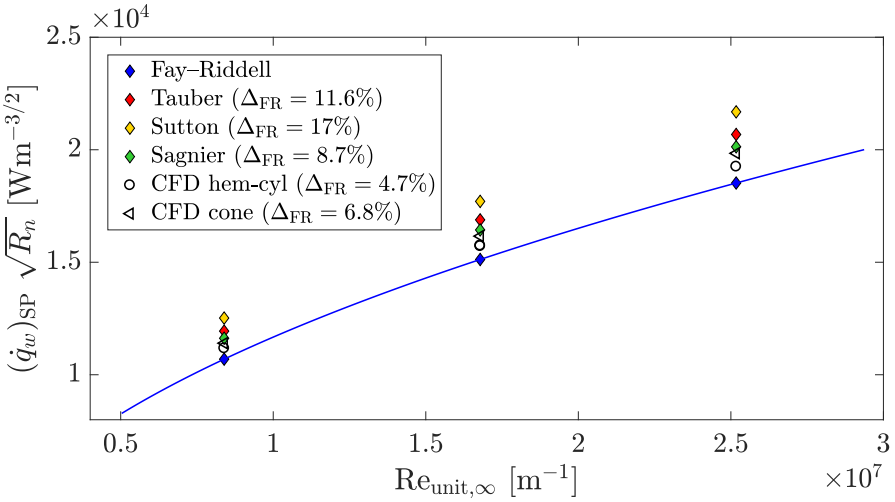

Figure 5.2: Comparison of normalized stagnation-heating predictions by engineering correlations and numerical simulations as a function of unit Reynolds number.

[1]The correlation of Cohen (1961) is not shown as it provides the same result as Fay and Riddell (1958) to within 0.1%.

5.2. Off-stagnation heating

The infrared thermography has been used to characterize the transient surface temperature distribution along the Plexiglas part of the body from which wall heat fluxes have been extracted. These experimental heating distributions can now be analyzed along with theoretical and numerical predictions.

A summary of the experimental test performed is given in Table 5.1.

Table 5.1: Experimental test matrix.

Name	Test conditions				Model	
	p_0 [bar]	T_0 [K]	$\mathrm{Re}_{\mathrm{unit},\infty}$ [m^{-1}]	T_{w0} [K]	θ_c [°]	R_n [mm]
10 bar	10.8	505	$8.9 \cdot 10^6$	295.7	7.4	3.5
15 bar	15.9	520	$12.3 \cdot 10^6$	294.8	7.4	3.5
20 bar	20.7	522	$16.2 \cdot 10^6$	295.1	7.4	3.5

All infrared data presented in this section correspond to a test time of 1 sec after model injection. For enhanced visualization, temporal filtering over 15 frames (i.e., averaging over 0.3 sec) has been performed. Note that, apart from the time restrictions associated with the semi-infinite slab hypotheses[2], the point in time for which the results are presented does not appreciably alter the results. Since $\dot{q}_w$ decreases over time while T_w increases, from Eq. 4.20, these two effects compensate and the Stanton number remains more or less constant during the test. This statement is graphically illustrated in Fig. 5.3, showing the evolution of T_w, $\dot{q}_w$ and $\mathrm{St}_{\mathrm{mod}}$ over time (relative to model injection) at a particular 9-pixel region located in the center of the test model. This graph clearly illustrates the IRDA time-integration procedure and indicates the typical thermal amplitude that can be expected during such a wind-tunnel test.

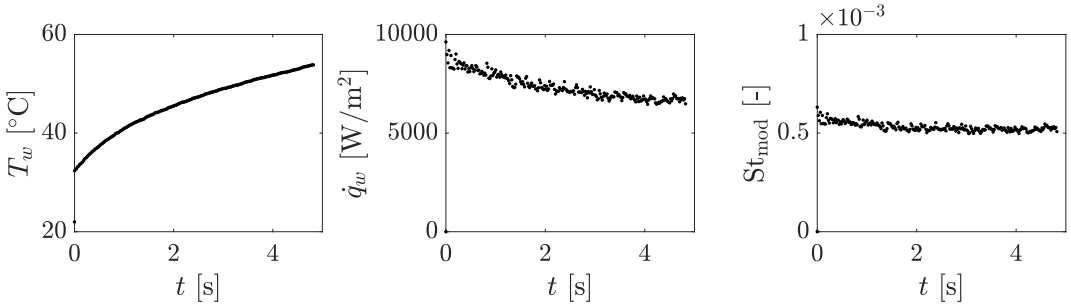

Figure 5.3: Time evolution of temperature, heat flux and Stanton number of a localized pixel in the middle of the 7.4° half-angle conical model, for a test at 20 bar.

[2]From Eq. 4.21, $t = 1$ sec corresponds to a minimum allowable thickness of 3 mm. All models present larger thicknesses, or equal thickness just at the steel-Plexiglas junction, where lateral conduction effects are expected to invalidate the results anyway.

5.2.1. Contour maps

Heat-flux and Stanton-number maps obtained from the IR measurements over the 7.4°-half-angle cone with a 3.5-mm spherical nose are given in Fig. 5.4 and 5.5.

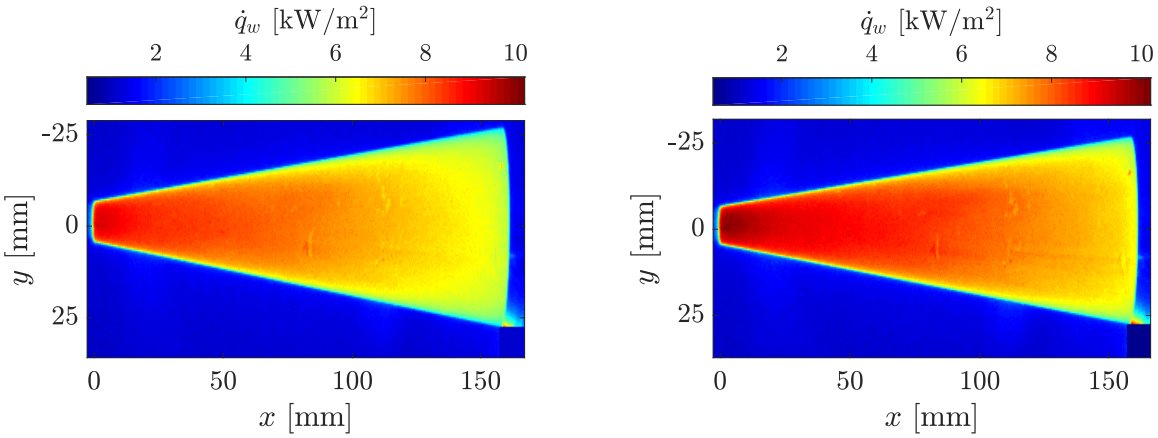

(a) $p_0 = 15$ bar. **(b)** $p_0 = 20$ bar.

Figure 5.4: Heat-flux contours on the 7.4°-half-angle cone with a 3.5-mm nose radius.

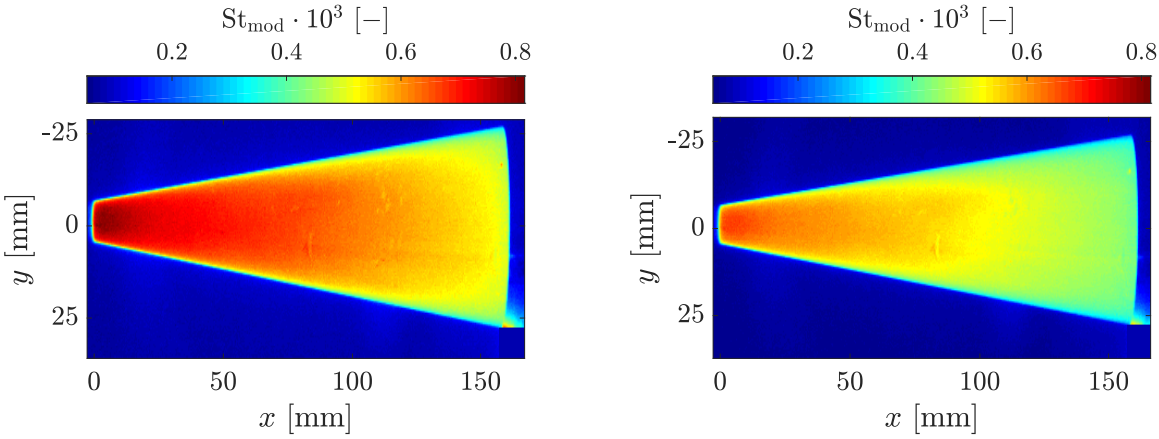

(a) $p_0 = 15$ bar. **(b)** $p_0 = 20$ bar.

Figure 5.5: Modified-Stanton-number contours on the 7.4°-half-angle cone with a 3.5-mm nose radius.

First of all, for both the 15-bar and the 20-bar cases, the axisymmetry of the flow field seems to be well verified. This suggests that the model has been adequately positioned inside the test section at a place where the nozzle jet is rather uniform. Nonetheless, no firm conclusions can be drawn from this qualitative observation. In a previous infrared investigation in the VKI H3 facility, Masutti (2013) observed a region of large St near the trailing edge of the cone model. The schlieren visualizations that he also performed revealed that the hypersonic jet core of the H3 tunnel was slightly overexpanded, so that a shock wave impinging on the rear part of the cone was responsible for the localized heated zone. No such effects have been observed in the present study. Note that the small spots in the present maps are due to model imperfections (e.g., damaged black paint layer) and that the model support has been erased from the lower

right corner of the image.

Secondly, the 20-bar case displays larger values of heat fluxes than the 15-bar case, while the inverse can be said for the Stanton number. Heating rates are proportional to the free-stream Reynolds number (driven by the stagnation pressure) and the normalization into Stanton numbers reverses this dependence. For a flat plate, the theoretical Stanton number is inversely proportional to the square root of the Reynolds number (see Eq. 2.14).

Finally, note the significant difference in heat-flux magnitude compared to the stagnation-point predictions in § 5.1. The heating rate on the conical afterbody is of few kW/m^2, compared to approximately 250 kW/m^2 at the stagnation point.

5.2.2. Centerline profiles

The experimental heating distributions can now be analyzed along with theoretical and numerical predictions along the models' centerline. In addition to temporal filtering, the experimental streamwise profiles have been averaged over 5 spanwise pixels to smooth out the noise in the data. It should be noted that the 10-bar profile is not displayed entirely since the model's nose was not totally cooled down when the test was run.

Regarding the theoretical laminar predictions, the methods of Zoby et al. (1981) for blunt bodies (Eq. 2.27-2.28) and Eckert (1956) (Eq. 2.14) for slender bodies are considered, combined with either the Modified Newtonian Theory (MNT) or Taylor–Maccoll (TM) for the inviscid solution (edge of the boundary layer). The correlation of Lees (1956) (Eq. 2.18-2.19) is not used here since the highly cooled wall assumption is not entirely respected in the H3 facility, where $T_w/T_{aw} \approx 0.6$. Even though the actual flow field is laminar, the turbulent predictions of Crabtree et al. (1970) (Eq. 2.33 - 2.35), van Driest (1956) (Eq. 2.31) and Eckert (1956) (Eq. 2.30) can also be plotted to highlight the difference in orders of magnitude of heating rates.

As a recall, the CFD simulations were run fully laminar.

In Fig. 5.6, the Stanton numbers along the centerline streamwise coordinate x normalized by the nose radius R_n[3] are presented for the 20-bar case. As a first observation, the different predictive tools all provide the same order of magnitude for the laminar $\mathrm{St}_{\mathrm{mod}}$. The turbulent predictions are well above all other results and no transition to turbulence is observed. The engineering correlations, in solid lines, are very close to each other on the downstream part of the cone. As expected, they differ significantly when approaching the nose because of their respective underlying assumptions (sharp or blunt body, evaluation of edge conditions). The numerical solution in dashed line approaches the theoretical curves from below, with better agreement as x/R_n increases. For lower x/R_n and on the nose, larger differences are observed. Regarding the experimental result, for $x/R_n \gtrapprox 18$ the curve seems to be slightly shifted upward compared to the other ones, but qualitatively follows a similar evolution. However, for $x/R_n \lessapprox 18$, the infrared thermography predicts a lower Stanton number. It seems that the experimental curve remains rather linear with x: the expected rise in wall heat flux when approaching the nose (but still on the Plexiglas part) is not experimentally observed.

[3]Different nose radii were supposed to be compared.

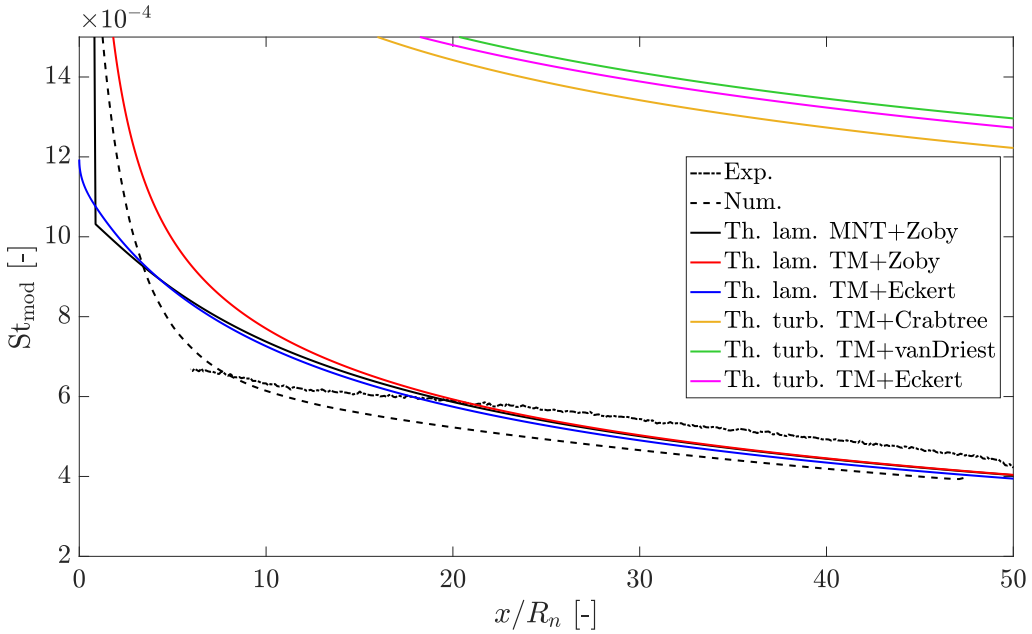

Figure 5.6: Stanton-number streamwise profiles along model's centerline and comparison between theory, CFD and experiments (test at 20 bar).

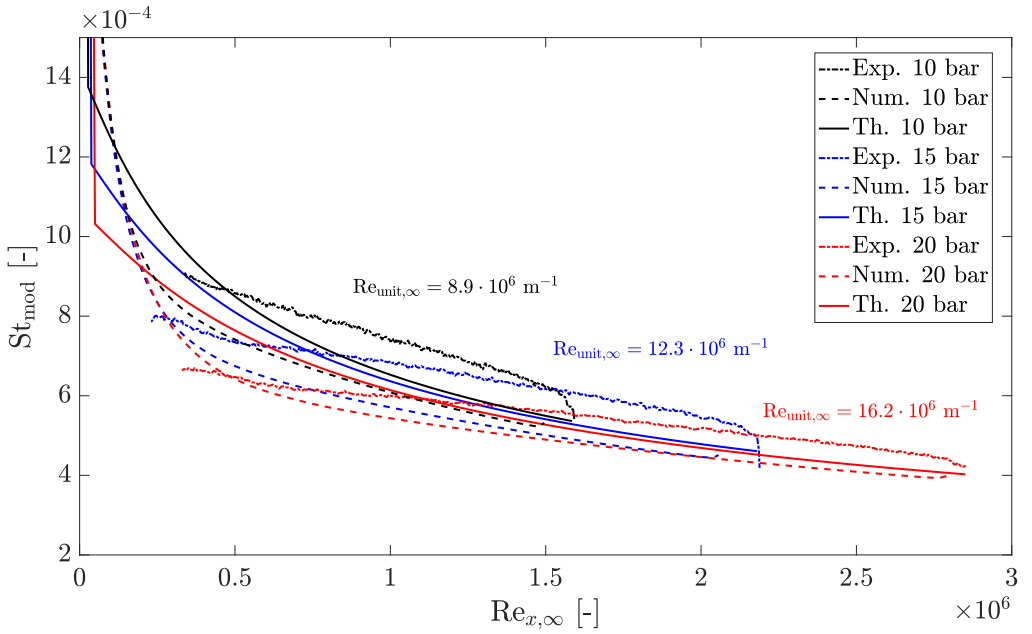

Figure 5.7: Stanton-number streamwise profiles as a function of Reynolds number based on streamwise coordinate x, for different stagnation pressures and comparison between theory (MNT+Zoby et al.), CFD and experiments.

Since different free-stream conditions are tested, results can be plotted as a function of a local Reynolds number $\mathrm{Re}_{x,\infty}$ instead of the streamwise distance from the nose x, as presented in Fig. 5.7. This choice of non-dimensional variables does not fully remove the influence of the free-stream unit Reynolds number since the Stanton number is still lower for larger total pressures. Nonetheless, the ending part of a given experimental, numerical or theoretical curve is well superposed on the corresponding prediction for the next larger unit Reynolds number. Whatever the unit Reynolds number, the experimental results are first under-predicting heating rates compared to theoretical/numerical predictions, before over-predicting them on the remaining portion of the body.

It is also common to normalize the modified Stanton number by the square root of the free-stream local Reynolds number ($\mathrm{St}_{\mathrm{mod}} \cdot \mathrm{Re}_{x,\infty}^{1/2}$) to partially remove the influence of different free-stream conditions. Recall that the theoretical Stanton number for a sharp cone is inversely proportional to the square root of the Reynolds number. In this case, as shown in Fig. 5.8, the results of a same predictive family collapse relatively well onto a single line.

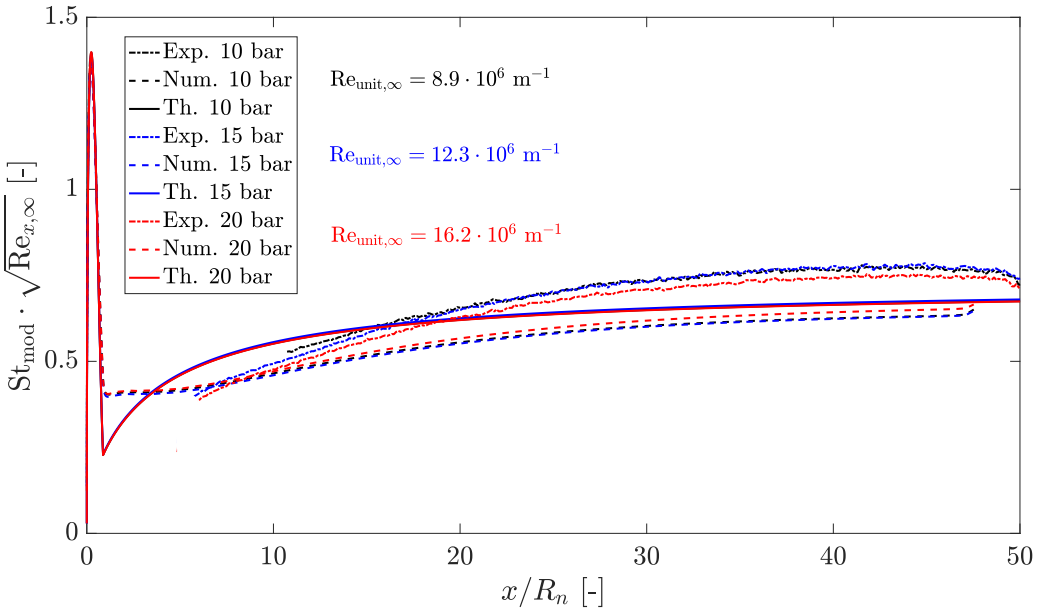

Figure 5.8: Stanton-number streamwise profiles along model's centerline normalized by square root of Reynolds number for different stagnation pressures and comparison between theory (MNT+Zoby et al.), CFD and experiments.

Overall, engineering correlations and CFD solutions reasonably well capture the actual heating rates, though the experimental curves seem to be shifted upward and do not follow the expected rise when approaching the nose. Possible causes for these discrepancies may be

- a wrong estimation of the ρck value (this aspect is quantified in the uncertainty analysis in § 5.3),
- uncertainties on the reference flow conditions, mainly the reservoir temperature,
- the test article does not have the same emissivity as the calibration plate as initially assumed,

- the steel-Plexiglas junction constitutes a heat sink and alters the computed heating rates,
- the flow is not totally uniform (streamwise gradients),
- the model is slightly misaligned with the incoming flow.

The limited experimental data available does not allow to draw firm conclusions. It was initially planned to examine several of these points, especially the effect of model positioning inside the test section.

Other models

Even though the measurements could only be made on one conical geometry, in Chapter 3 a computational mesh has been created for the hemispherical cylinder. Besides, the theoretical correlations allow to compute heating rates over any axisymmetric geometry. Hence, Fig. 5.9 compares the predicted heating rates between the 7.4°-half-angle cone model and the hemispherical cylinder model for a typical medium-Reynolds-number test. In Fig. 5.9(a), the Stanton profiles are displayed along the arc length s (wetted distance along body surface measured from stagnation point), while Fig. 5.9(b) presents the results as a function of the angle θ between the streamwise direction x and the radius vector from the center of curvature of the nose. The y-axis does not extend up to the stagnation-point values since these have already been discussed in § 5.1.

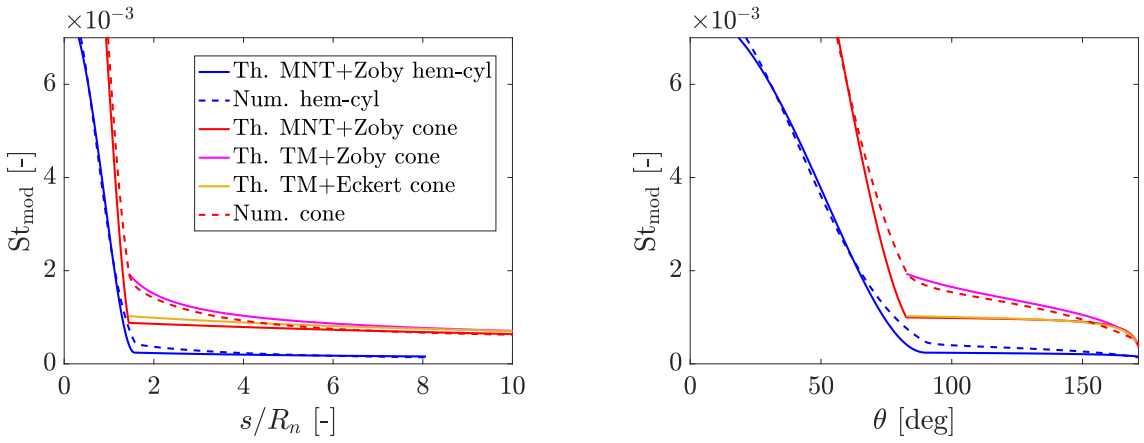

(a) As a function of s/R_n distance.

(b) As a function of θ angle.

Figure 5.9: Comparison between Stanton-number profiles over the 20-mm-nose-radius hemispherical cylinder and the 7.4°-half-angle cone, as predicted by theoretical methods and CFD solutions, for a typical medium-Reynolds-number case (same legend for both subfigures).

It can be seen that the heating rates over the blunt cone are larger than those experienced by the hemispherical cylinder. This is not only due to the nose bluntness, but also to the afterbody which is more exposed to the incoming flow in the case of the conical model. The larger the cone aperture θ_c, the larger the heating rates on the conical skirt. Then, the different approximate methods agree rather well with the CFD solutions, validating the theoretical tools. In particular, the heating equation of Zoby et al. (1981) combined with the MNT provides satisfactory results over the hemispherical cylinder, with very good agreement all over the nose.

The Modified Newtonian Theory is less successful for the cone case, as better seen in Fig. 5.9(b). As already noted in § 2.2.3, the MNT fails to predict the overexpansion around

the shoulder of the blunt cone as well as the subsequent recompression further downstream on the conical skirt. However, using a Taylor–Maccoll solution for a sharp cone over the conical skirt with Zoby et al. formulation yields Stanton profiles in closer agreement with CFD. The predictions of Eckert (1956) for a sharp cone are also shown on the conical skirt. All theories meet on the rear part of the body.

This 7.4°-half-angle, 3.5-mm-nose radius cone is an ambivalent geometry as it is neither a sharp slender body nor a strongly blunted body (such as a sphere or a capsule-shaped geometry). The MNT appears to be efficient on the nose region, but further downstream the geometry meets the equivalent sharp-cone geometry and more suitable inviscid methods should be used.

Lastly, Fig. 5.10 summarizes Stanton-number results obtained by the theoretical method of Zoby et al. (1981) for all the four conical geometries available in the H3 lab (see Fig. 4.15). As expected, the Stanton number increase with increasing cone half-angle and decreasing nose radius. The 15°-half-angle, 1-mm-radius model would have experienced the greatest heating rate, though blockage of the tunnel due to this large object could have happened too.

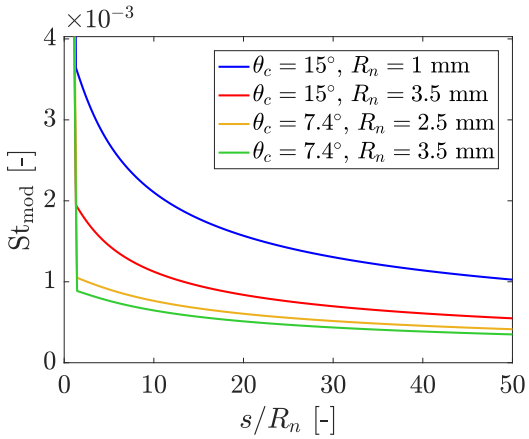

Figure 5.10: Stanton-number predictions from Zoby et al. (1981) with MNT for the four conical models at medium-Reynolds-number condition.

5.3. Uncertainty analysis

This section aims to assess approximately the uncertainties in the experimental measurements and results. A real measurement is always made with some inaccuracies that propagate throughout the whole data-reduction chain to produce (often significant) errors and uncertainties in the final derived results. The approach adopted here to study the propagation of uncertainties is the general uncertainty analysis using the Taylor Series Method, explained in details by Coleman and Steele (2018). The present analysis considers only the combined standard uncertainties in the measured variable without trying to separate the effects of systematic (invariant) and random (varying) errors.

Generally, in an experiment, a data-reduction equation is used to combine n measured vari-

ables X_i into the final test result r, expressed as

$$r = r(X_1, X_2, ..., X_n). \tag{5.1}$$

Assuming independent variables and neglecting higher-order terms, the combined standard uncertainty in the result is given by

$$\delta r^2 = \left(\frac{\partial r}{\partial X_1}\right)^2 \delta {X_1}^2 + \left(\frac{\partial r}{\partial X_2}\right)^2 \delta {X_2}^2 + ... + \left(\frac{\partial r}{\partial X_n}\right)^2 \delta {X_n}^2, \tag{5.2}$$

where δX_i are the standard uncertainties in the measured variables X_i. In this study, all uncertainties have been established for a 95% confidence level. Therefore, the uncertainty δX in variable X is connected to the standard deviation σ_X by: $\delta X = 1.96\ \sigma_X$.

The first step of the uncertainty analysis is to identify potential sources of uncertainties and to select which of them are most relevant and should be considered for the present analysis. The fundamental input quantities from which everything else is derived are listed hereafter.

1. **The stagnation temperature** T_0. The instrument measuring T_0 is the source of this error. The uncertainty related to the thermocouple is $\delta T_0 = \pm 1.2°\text{C}$, as established in § 4.1.2.

2. **The stagnation pressure** p_0. Similarly to T_0, the uncertainty in p_0 directly arises from the pressure transducer, whose uncertainty was given by the manufacturer: $\pm 0.125\%$ at full scale (see § 4.1.2).

3. **The Mach number** M_∞. Its uncertainty is due to flow fluctuations inside the test section (Mach number non-uniformity). The Mach number deviation from its nominal value ($\text{M}_\infty = 6$) is taken to $\delta\text{M}_\infty/\text{M}_\infty = 1.5\%$. This choice is based on recent calibration of the H3 (Agostinelli, 2018) and previous reports (Asma, 2001).

4. **The thermal product of the material** $\sqrt{\rho ck}$. Many past studies have highlighted that the uncertainty in the physical properties of the wall material is the main source of error for the determination of heat transfer (Simeonides, 1990, Yang, 2001). The uncertainty in the thermal product is usually given by the manufacturer. Typical values range from $\delta(\rho ck)/\rho ck \approx 3.5\%$ to $\approx 7\%$ (Simeonides et al., 1993, Boerrigter et al., 1993, Elbay, 1993, Grossir, 2015). In the present work, no information regarding the exact value of $\delta(\rho ck)$ was found, thus a conservative $\pm 7\%$ uncertainty has been assumed.

5. **The wall temperature** T_w. Its uncertainty directly arises from the calibration of the instruments, i.e., the thermocouples (TC) and the IR thermograph (IR) (see § 4.2.2). The error due to the reading on the mercury thermometer (TM) ($\approx 0.05°\text{C}$) should also be taken into account. Therefore, following Coleman and Steele (2018) and Amoiridis et al. (2018),

$$\delta T_w = \sqrt{\delta T_{\text{TM}}^2 + \delta T_{\text{TC}}^2 + \delta T_{\text{IR}}^2}\,. \tag{5.3}$$

The errors δT_{TC} and δT_{IR} are derived by applying Eq. 5.2 on their second-order calibration laws. A dedicated MATLAB routine is used to compute the standard errors (estimates of standard deviation) on the calibration coefficients using the curve-fit informa-

tion. Contrary to the other input variables, δT_{TC} and δT_{IR} depend on T_w. The different sources of uncertainties in T_w are illustrated in Fig. 5.11. To perform the normalization in Fig. 5.11(b), the temperatures had to be expressed in Kelvin. As noted by Simeonides (1990), the uncertainty in the measurement of T_w results mostly from the uncertainty in the calibration law of the camera, stressing the need for an accurate calibration procedure.

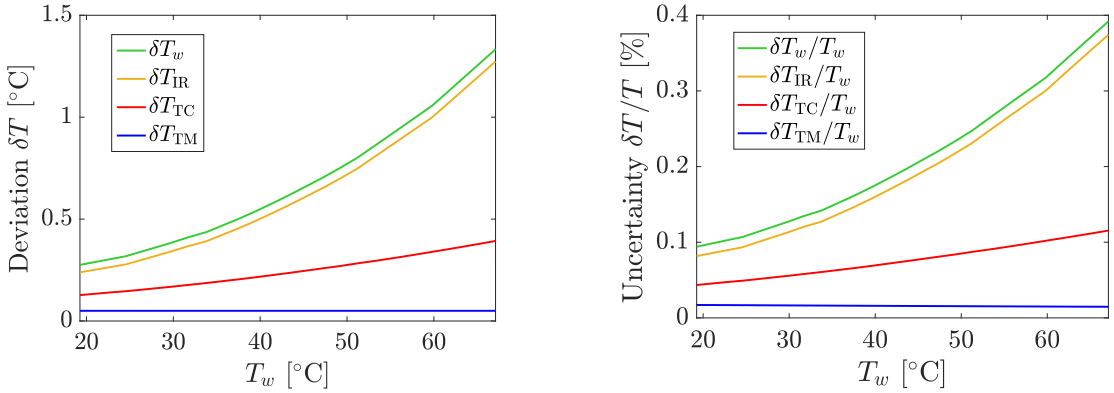

(a) Absolute deviation. **(b)** Normalized uncertainty.

Figure 5.11: Uncertainty analysis for the wall temperature T_w.

Any uncertainty in these inputs will propagate through the data-reduction system. The latter consists of Eq. 4.1 through 4.6 for the derivation of free-stream properties, then Eq. 4.19 for the heat-transfer rebuilding procedure and finally Eq. 4.20 for the modified Stanton number. Hence, Eq. 5.2 can be evaluated analytically for each variable of interest.

However, this procedure disregards the correlations between the different variables. For instance, at the denominator of the Stanton number appear the free-stream velocity and the total temperature. The flow velocity is derived from the total temperature measurement, hence these variables should not rigorously be considered as independent. Yet, this simple uncertainty analysis aims to provide general estimates for the uncertainties in the results. It is not the purpose of this work to perform a rigorous uncertainty quantification and sensitivity analysis relying on more sophisticated stochastic methods (e.g., polynomial chaos). Such approaches can be employed for data-reduction systems involving many variables and highly nonlinear equations, where numerical techniques to automate the determination of partial derivatives are more convenient (e.g., DAKOTA software (Adams et al., 2011) for uncertainty quantification, as used by Masutti (2013) and Carugno (2012)).

The free-stream properties are fully determined from the first three inputs T_0, p_0 and M_∞. Their associated uncertainties are presented in Table 5.2. Even if the input variables uncertainties are relatively small, because of the propagation of uncertainties, large errors can be obtained as outputs, with the largest error for the Reynolds number. These orders of magnitude are similar to those obtained in previous similar studies in VKI (Santarelli and Charbonnier, 1999, Strub, 2006).

Table 5.2: Uncertainties on free-stream flow quantities for a typical experiment at medium-Reynolds-number condition (95% confidence level).

	Variable	Nominal value	Uncertainty [%]
Inputs	T_0	500 K	0.24
	p_0	20 bar	0.25
	M_∞	6	1.5
Outputs	T_∞	60.98 K	2.65
	p_∞	1266.7 Pa	9.22
	μ_∞	$4.05 \cdot 10^{-6}$ kg/(m · s)	4.08
	ρ_∞	0.072 kg/m^3	9.59
	u_∞	939.15 m/s	2.00
	$\mathrm{Re}_{\mathrm{unit},\infty}$	$1.68 \cdot 10^7$ /m	9.80

The uncertainties in heat flux and Stanton number are affected by all five input variables. They depend on the true instantaneous test conditions. Uncertainties have been computed for the experimental test at 20 bar (shown in Fig. 5.6) and were found to be representative of the other test cases. An uncertainty of $\approx 8.3\%$ was obtained for the heat flux all along the model's surface. For the Stanton number, the results are presented in Fig. 5.12. An uncertainty of about $\approx 12.9\%$ is observed for $\mathrm{St}_{\mathrm{mod}}$. This large value is not surprising and is similar to those obtained in internal and external infrared studies (Carugno, 2012, Running et al., 2019). The Stanton number is defined as a function of $\dot{q}_w$, ρ_∞, u_∞, T_w and T_0, all of which having an appreciable amount of uncertainty that propagates and gets amplified through the data-reduction chain. As can be seen in Fig. 5.12, these errors bands are of similar magnitude as the differences between the experimental results and the other results. Even if the present analysis regards the input variables as fully independent which tends to overestimate the uncertainties, it can be expected that the experimental measurements are in reality in better agreement with the other predictive tools results. It is thus important to quantify—even roughly—these uncertainties.

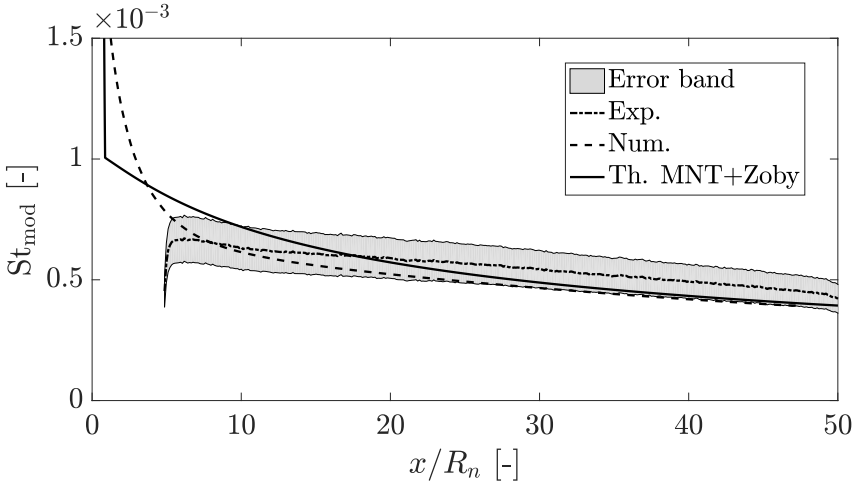

Figure 5.12: Error bandwidth for the experimental Stanton number extracted along the conical model's centerline at 20 bar.

To conclude this section, a brief discussion is made about the former VKI work of Carugno (2012). The latter focused on uncertainty quantification and sensitivity analysis using the DAKOTA toolkit (Adams et al., 2011). The input parameters were the same as in the present study, except for the material emissivity ε which is not taken into account in our calculations (since plate and models were assumed to be covered with the same matte paint and because of the in-situ calibration, see § 4.2.2). Carugno attributed input uncertainties very similar to those presently used, but studied the effect of three different input uncertainties assumed for the material product ρck. As in the present case, no clear tolerances for the parameters ρ, c and k were found. Carugno used a simple error propagation analysis to compute free-stream uncertainties, whereas the DAKOTA code was solely used to derive the uncertainty on $\mathrm{St}_{\mathrm{mod}}$.

The main results of the study led by Carugno (2012) are presented in Table 5.3. Firstly, for the same input uncertainty on ρck[4], the present estimated uncertainty for the Stanton number is larger than the value obtained by Carugno. This certainly results from the conservative and simple approach adopted here neglecting the correlation between the different variables. Secondly, it is clear that the lack of knowledge about the thermal properties of the material induces a significant error in the final result. Then, the sensitivity analysis enabled quantifying by how much the uncertainty in a given input is responsible for the uncertainty in the final result. This relative importance was expressed through sensitivity or Sobol indices. The study demonstrated that the error in the material product had the greatest impact on the final result. The accurate determination of ρck should thus be the focus of future investigations. The uncertainties resulting from the calibration of the instruments also play an important role in causing variance in the results, more than the reservoir properties do.

Table 5.3: Summary of the main results of the uncertainty quantification and sensitivity analysis carried out by Carugno (2012) by considering three different input errors for ρck.

Input error [%]	Output error [%]	Inputs Sobol indices [%]			
ρck	$\mathrm{St}_{\mathrm{mod}}$	ρck	ε	Calib. coeff.	p_0, T_0
5	10.1	26	25	29	20
10	13.3	58	15	16	11
15	17.4	75	9	10	6

[4]If an error of 5% on ρck is assumed, all other things being equal, the present analysis yields about 11.6% error on $\mathrm{St}_{\mathrm{mod}}$.

6. Conclusions and perspectives

6.1. Conclusions of this work

This Master thesis aimed at developing and exploiting a methodology for convective aerodynamic heating predictions over hypersonic vehicles in axisymmetric and two-dimensional configurations. A comparative study has been conducted to investigate the heating rates provided by three different predictive tools: theoretical or engineering methods, numerical simulations and experimental measurements using infrared thermography.

The first part of this work was dedicated to the review and implementation of some approximate methods for the prediction of both stagnation-point and off-stagnation-point heating rates. Laminar boundary layers were of main interest, but semi-empirical correlations for turbulent heating rates were also handled. Contrary to the stagnation-point and slender-body heating for which self-similarity greatly simplifies the analytical treatment, blunt-body heating formulations are less straightforward. The Modified Newtonian Theory combined with isentropic expansion from post-normal-shock conditions was used to infer the boundary-layer edge properties and the method was shown to be reasonably accurate on the forward portion of the body. The present implementation of all methods was validated against higher-fidelity data and the main limitations of each approach were highlighted. This review has uncovered and gathered several useful aerothermodynamic predictive methods to be used in future studies.

Computational Fluid Dynamics was used as a complementary tool to examine centerline heating rates on a hemispherical cylinder and a blunt cone at Mach 6 in VKI H3 test conditions. 2D axisymmetric meshes were created to capture the shock shapes and the gradients in the boundary layer at the wall, where an isothermal condition was prescribed. Perfect-gas laminar viscous-flow numerical simulations were carried out using the CFD++ software. Some preliminary numerical results were presented to verify the adequacy of the numerical modeling. Several CFD heat-transfer results could be exploited throughout the study to validate the theoretical formulations.

The main part of this work was the investigation of heat-transfer measurements over hypersonic vehicles in the VKI H3 wind tunnel using an infrared camera. Emphasis was placed on the development and validation of a suitable experimental setup. The free-stream conditions inside the test section are determined by the measurements of stagnation temperature and pressure, assuming a Mach 6 free jet. Flow-field non-uniformities were quantified by reviewing previous calibrations of the facility. The infrared thermography technique was thoroughly presented as an efficient non-intrusive tool to measure transient surface temperature distribution. The present 50-Hz, 640×480 pixel FLIR A655sc camera was carefully calibrated against thermocouples themselves previously calibrated. The procedure to extract convective heating distribution from the model surface temperature relies on the semi-infinite slab principle meeting three strong assumptions. This idealized heat-conduction model is implemented in the VKI IRDA tool dealing with infrared measurements data processing. The code has been upgraded and validated. Available Plexiglas test models were finally presented.

The results yielded by the different predictive methods could be finally compared and discussed, although an unfortunate technical issue in the facility prevented the experimental campaign from being properly led. Stagnation-point measurements being absent due to material constraints, theoretical and numerical predictions were compared at this location and the agreement was overall rather good. The expected dependencies of stagnation-point heating with nose radius and free-stream Reynolds number were retrieved. Away from the nose, the few experimental results available on a 7.4°-half-angle, 3.5-mm-nose-radius cone suggested good axisymmetry of the problem. Increasing reservoir pressure led to increasing heat flux and decreasing Stanton number. On the centerline, measured heat-flux followed a purely laminar evolution, with orders of magnitude equal to theoretical and numerical predictions. Nonetheless, the trends of the centerline profiles differed, with experimental results first being inferior to theoretical and numerical ones on the forward portion of the body and then slightly exceeding them further downstream. Several possible causes for these disagreements have been suggested but could not be further examined and verified in practice. Normalizing the Stanton number with the square root of the free-stream Reynolds number allowed to partially remove the influence of different free-stream conditions. For the blunt cone, but also other geometries such as a hemispherical cylinder, engineering predictions compared well with CFD results. Specific theories appeared more suitable than others depending on the considered geometry and nose radius.

Lastly, a simple error propagation analysis was conducted to assess the uncertainty of the experimental results. Respective errors of roughly 9.8%, 8.3% and 12.9% were obtained for the free-stream unit Reynolds number, wall heat flux and Stanton number. The thermal product ρck, not perfectly known, is mostly responsible for the large uncertainties in heating predictions.

Despite the lack of experimental data, the present experimental approach could be validated and results judged promising have been obtained. It can safely be concluded that infrared thermography is a powerful and relatively simple technique to assess aerodynamic heating rates in hypersonic facilities. Engineering correlations also demonstrated favorable results in spite of their simplicity. Experimental and theoretical techniques used together constitute an interesting and efficient heat-flux predictive approach for aerothermodynamic preliminary design studies. Nonetheless, the overall work is far from being completed and several improvements can be made, as discussed in the following section.

6.2. Recommendations and perspectives

Throughout the theoretical analysis, a number of hypotheses have been posed and several flow phenomena have been ignored. The present blunt-body heating methods neglected the effects of entropy-layer swallowing. The latter could be accounted for in future work by coupling the boundary-layer solution with an inviscid flow-field solution, from Euler numerical computations for instance. This would allow to more accurately predict heating rates over the whole body surface, especially in the case of turbulent boundary layers (Riley et al., 1990), at the expense of computational time, though.

Besides, the present analysis was restricted to two-dimensional and axisymmetric vehicles at zero angle of attack. It has already been suggested in § 2.5 that an enhancement of the method

would be to handle arbitrary three-dimensional configurations, as done in most engineering-level tools used for preliminary design studies. Such aerothermodynamic predictions constitute a possible future extension for the existing VKI tool ANTARES.

From the experimental point of view, the whole experimental setup has been designed and is ready for effectively carrying out a full and thorough experimental campaign. Different test models and nose radii should be considered to assess the capability of theoretical methods and infrared thermography to accurately predict heating rates on different body shapes. Repeatability of the measurements should be ensured.

A crucial recommendation for future work is to study the effect of model positioning inside the test section, in terms of distance behind the nozzle exit and offset to the centerline, following the recommendations of previous H3 calibrations (Agostinelli, 2018). This investigation would allow to evaluate the potential influence of nozzle flow non-uniformities on the wall heat-flux measurements.

The test models themselves require better surface quality control. Their surfaces get ineluctably damaged over time. The layers of black paint have been locally removed, giving rise to spots of different emissivity and potentially creating roughness effects.

There are several ways to improve the free-stream flow characterization in the H3 tunnel. The present measurements of the stagnation temperature and its temporal variations could be further enhanced by relying on an even more precise acquisition module. A new calibration of the facility ought to be performed to better characterize free-stream noise levels which are known to significantly influence the boundary-layer transition process.

The application of infrared thermography could also be enhanced. Since the present study focused on axisymmetric problems and hence centerline heating, no 3D temperature-field reconstruction has been attempted. In particular, a more robust approach should comprise an image resection technique to account for the distortion introduced by the optical system of the infrared camera, as done by dello Ioio (2008) and Avallone (2015). The variation of surface emissivity with viewing angle should also be accounted for through a point-by-point calibration in order to reconstruct accurate heat-transfer maps.

The founding assumptions of the heat-flux rebuilding model were found to be rather strong and not always representative of reality. In the future, it is necessary to acquire a better knowledge of the material properties and their variations with temperature. This is all the more important as the uncertainties in the thermal product ρck are the main sources of error for the determination of heat transfer. New alternatives regarding material choice should also be considered. Asma et al. (2002) observed that experiments with Vespel give more reliable infrared results due to the lower thermal diffusivity and the better ability of this material to withstand high temperatures with little variation in its properties, compared to Plexiglas. Macor and PEEK, respectively used in the studies of Saravanan et al. (2009) and Juliano et al. (2019), are other very good insulating material candidates. Furthermore, the 1D heat-conduction analysis could be replaced by a 3D heat-flux identification procedure, as initially proposed by Playez (1997). Such an analysis would require more effort and lead to more complexity than the present simple approach, but for enhanced accuracy in inferring the surface heat-flux distribution from an observed temperature-map history.

The experimental determination of the stagnation-point heating with the infrared technique remains very challenging, because of the material constraints and the highly curved surface there. A recommendation is to investigate such potential measurements using small coaxial

thermocouple sensors such as the one developed at VKI by Kovács (2018), at least for models with not too small nose radii. A comparison of these critical peak heating rates could be made with engineering correlations and numerical simulations, hence refining the aerodynamic heating analysis.

In addition to heat-flux identification using the infrared measurement technique, it is recommended to perform schlieren visualizations, as initially planned. This optical technique based on the refraction of light can provide qualitative information about phenomena such as shock waves, boundary-layer separation and transition. Schlieren visualizations could help in better defining the computational domain for CFD simulations. Besides, they would allow to support the flow-field interpretations and verify the results of infrared thermography.

Finally, more rigorous uncertainty quantification and sensitivity analysis could be carried out with dedicated numerical tools to gain better insight into the relative importance of each input variables and the propagation of uncertainties. This would consist in an extension of the work initiated by Carugno (2012) where only the true basic input variables would be accounted for without relying on a linearized error propagation approach.

A. Boundary-layer theory

A.1. Boundary-layer equations

Consider a two-dimensional coordinate system attached to the body surface with the x- and y- components respectively tangential and normal to the wall. The basic assumption of the boundary-layer theory is that, at sufficiently high Reynolds number, the flow can be divided into an outer inviscid region and a very thin layer close to the body where viscous effects are important. The Navier–Stokes equations can then be reduced to the simpler, though still partial differential, boundary-layer equations, given as follows for a steady compressible flow.

$$\text{Continuity:} \quad \frac{\partial(\rho u r_b^k)}{\partial x} + \frac{\partial(\rho v r_b^k)}{\partial y} = 0, \tag{A.1}$$

where $k = 0$ for a planar body and $k = 1$ for an axisymmetric body,

$$x - \text{Momentum:} \quad \rho u \frac{\partial u}{\partial x} + \rho v \frac{\partial u}{\partial y} = -\frac{\mathrm{d}p_e}{\mathrm{d}x} + \frac{\partial}{\partial y}\left(\mu \frac{\partial u}{\partial y}\right), \tag{A.2}$$

$$y - \text{Momentum:} \quad \frac{\partial p}{\partial y} = 0, \tag{A.3}$$

$$\text{Energy:} \quad \rho u \frac{\partial h}{\partial x} + \rho v \frac{\partial h}{\partial y} = \frac{\partial}{\partial y}\left(k \frac{\partial T}{\partial y}\right) + u \frac{\mathrm{d}p_e}{\mathrm{d}x} + \mu \left(\frac{\partial u}{\partial y}\right)^2. \tag{A.4}$$

To complete the system of equations for the unknowns u, v, ρ, T, h, assuming a perfect gas,

$$p = \rho R T \qquad R = \text{gas constant}, \tag{A.5}$$

$$h = c_p T \qquad c_p = c_v + R. \tag{A.6}$$

The boundary conditions are, at the wall ($y = 0$),

$$u = v = 0, \quad T = T_w \tag{A.7}$$

and at the edge of the boundary layer ($y \to \infty$)

$$u \to u_e, \quad T \to T_e. \tag{A.8}$$

A.2. Self-similarity

Self-similar solutions are ones of the few exact solutions to the boundary-layer equations. The idea of self-similarity is to transpose the boundary-layer problem from the (x, y) physical

space into a (ξ, η) space where the flow-field profiles become independent of the location along the surface ξ and collapse onto a universal solution. The goal is to reduce the set of partial differential equations into a set ordinary differential equations.

Let us consider the following coordinates transformation (Lees–Dorodnitsyn):

$$\xi = \int_0^x \rho_e u_e \mu_e r_b^{2k} \, \mathrm{d}x, \qquad \eta = \frac{u_e r_b^k}{\sqrt{2\xi}} \int_0^y \rho \, \mathrm{d}y. \tag{A.9}$$

The continuity equation is automatically satisfied by introducing the stream function ψ such that

$$\frac{\partial \psi}{\partial y} = \rho u r_b^k, \qquad \frac{\partial \psi}{\partial x} = -\rho v r_b^k. \tag{A.10}$$

Let us then define

$$u(\xi, \eta) = u_e(\xi) \frac{\partial f(\eta)}{\partial \eta} = u_e(\xi) f'(\eta), \tag{A.11}$$

$$\psi = \sqrt{2\xi} f, \tag{A.12}$$

$$h(\xi, \eta) = h_e(\xi) g(\eta). \tag{A.13}$$

Denoting the Chapman–Rubesin factor $C = \frac{\rho u}{\rho_e u_e}$ and applying the transformations, the x-momentum equation becomes

$$\left(C f''\right)' + f f'' = \frac{2\xi}{u_e} \left[\left(f'\right)^2 - \frac{\rho_e}{\rho} \right] \frac{\mathrm{d}u_e}{\mathrm{d}\xi}, \tag{A.14}$$

while the energy equation takes the form

$$\left(\frac{C}{\mathrm{Pr}} g' \right)' + f g' = 2\xi \left(\frac{\xi}{h_{t,e}} \frac{\mathrm{d}h_{t,e}}{\mathrm{d}\xi} \right) f' \left(2g + \frac{u_e^2}{h_e} \left(f'\right)^2 \right) - C \frac{u_e^2}{h_e} \left(f''\right)^2. \tag{A.15}$$

The corresponding transformed boundary conditions write, at the wall ($\eta = 0$)

$$f = f^{'} = 0, \quad g = g_w \tag{A.16}$$

and at the boundary-layer edge ($\eta \to \infty$)

$$f^{'} \to 1, \quad g \to 1. \tag{A.17}$$

The conditions for similarity are

- $C =$ cst or is related to f and g;
- $\mathrm{Pr} =$ cst or is related to f and g;
- ρ_e / ρ is related to f and g;
- $\frac{2\xi}{u_e} \frac{\mathrm{d}u_e}{\mathrm{d}\xi} =$ cst;
- $\frac{u_e^2}{h_e} =$ cst or is negligible;
- $\frac{\xi}{h_{t,e}} \frac{\mathrm{d}h_{t,e}}{\mathrm{d}\xi} =$ cst.

B. Infrared camera data sheet

FLIR

LWIR SCIENCE-GRADE CAMERA

FLIR A655sc™

With its uncooled, high-resolution detector and cutting-edge functionality, the FLIR A655sc helps researchers and scientists accurately quantify thermal patterns, leakage, dissipation, and other heat related factors in equipment, products, and processes in real-time.

www.flir.com/science

SUPERIOR IMAGE QUALITY & SENSITIVITY

Record crisp thermal images, even at high speeds

- Produce clearly detailed 640 x 480 thermal images using the maintenance free vanadium oxide (VoX) microbolometer
- Detect temperature differences as small as 50 mK
- Record 14-bit, full-frame data at up to 50 Hz, or 200 Hz with windowing

EASY, FLEXIBLE DATA COLLECTION

True plug and play connectivity simplifies data monitoring and sharing

- Fast image transfer over GigE Vision, using low-cost standard cables up to 100 meters
- Integrate with FLIR ResearchIR or third-party software seamlessly over Gigabit Ethernet connections
- Control the camera with GenICam protocol support

ADVANCED SOFTWARE COMPATIBILITY

Get more out of your data with advanced analysis tools

- Control and capture data directly intoFLIR ResearchIR Max or MathWorks® MATLAB
- Stream data directly to a PC running software for live viewing, recording, analysis, and sharing.
- Integrate with your proprietary software through optional Software Developers Kit (SDK)

Motorcycle break testing.

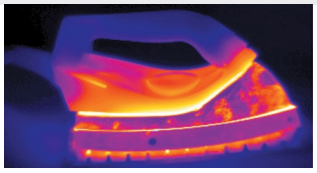

Thermal quality control on domestic appliances.

IMAGING SPECIFICATIONS

System Overview	FLIR A655sc
Detector Type	Uncooled Microbolometer
Spectral Range	7.5 – 14.0 µm
Resolution	640 x 480
Detector Pitch	17 µm
NETD	<30 mK
Imaging	
Time Constant	<8 ms
Frame Rate (Full Window)	50 Hz
Subwindow mode	User-Selected, 640 x 240 or 640 x 120 (Gigabit Ethernet Only)
Maximum Frame Rate (@ Min. Window)	200 Hz (640 × 120)
Dynamic Range	16-bit
Digital Data Streaming	Gigabit Ethernet (50/100/200 Hz) USB(25 Hz)
Command and Control	Gigabit Ethernet, USB
Measurement	
Standard Temperature Range	–40°C to 150°C (–40°F to 302°F) 100°C to 650°C (212°F to 1,202°F)
Optional Temperature Range	Up to 2,000°C (3,632°F)
Accuracy	±2°C or ±2% of Reading
Optics	
Camera f/#	f/1.0
Available Lenses	6.5 mm (80°), 13.1 mm (45°), 24.6 mm (25°), 41.3 mm (15°), 88.9 mm (7°)
Focus	Automatic or Manual (Motorized)
Close-up / Microscopes	Close-up 25 µm, 50 µm, 100 µm
Image Presentation	
Digital Data	Via PC Using ResearchIR Software

General	
Operating Temperature Range	-15°C to 50°C (572°F to 3,632°F)
Storage Temperature Range	-40°C to 70°C (-40°F to 158°F)
Encapsulation	IP 30 (IEC 60529)
Bump / Vibration	25 g (IEC 60068-2-29) / 2 g (IEC 60068-2-6)
Power	12/24 VDC, 24 W Absolute Max.
Weight	0.9 kg (1.98 lb)
Size	216 × 73 × 75 mm (8.5 × 2.9 × 3.0 in)
Mounting	¼"-20 (on three sides), 2 x M4 (on three sides)

MathWorks

CORPORATE HEADQUARTERS
FLIR Systems, Inc.
27700 SW Parkway Ave.
Wilsonville, OR 97070
PH: +1 877.773.3547

SANTA BARBARA
FLIR Systems, Inc.
6769 Hollister Ave.
Goleta, CA 93117
PH: +1 805.690.6600

CANADA
FLIR Systems, Ltd.
920 Sheldon Court
Burlington, ON L7L 5K6
Canada
PH: +1 800.613.0507

LATIN AMERICA
FLIR Systems Brasil
Av. Antonio Bardella,
320 Sorocaba, SP 18085-852
Brasil
PH: +55 15 3238 7080

CHINA
FLIR Systems Co., Ltd
Rm 1613-16, Tower II
Grand Central Plaza
138 Shatin Rural Committee Rd.
Shatin, New Territories
Hong Kong
PH: +852 2792 8955955

EUROPE
FLIR Systems, Inc.
Luxemburgstraat 2
2321 Meer
Belgium
PH: +32 (0) 3665 5100

www.flir.com
NASDAQ: FLIR

17-1683-INS-A655sc Datasheet

FLIR® | The World's Sixth Sense®

Bibliography

Adams, B., Bohnho, W., Dalbeya, K., Eddy, J., Eldred, M., Gay, D., Haskell, K., Hough, P. and Swiler, L., 2011. DAKOTA, A Multilevel Parallel Object-Oriented Framework for Design Optimization, Parameter Estimation, Uncertainty Quantication, and Sensitivity Analysis: Version 5.2 User's Manual. Tech. rep., Sandia National Laboratories.

Agostinelli, P.W., 2018. Experimental study of hypersonic flow in the VKI H3 wind tunnel: from facility characterization to boundary-layer interaction over low-temperature ablators. STP report 2018-24, von Karman Institute for Fluid Dynamics.

Allen, H.J. and Eggers, A.J., 1953. A study of the motion and aerodynamic heating of missiles entering the Earth's atmosphere at high supersonic speeds. NACA Research Memorandum A53D28, National Advisory Committee for Aeronautics.

Ames research staff, 1953. Equations, Tables and Charts for Compressible flow. NACA report 1135, National Advisory Committee for Aeronautics.

Amoiridis, O., Ascione, F. and Comez, Y., 2018. Heat transfer MTLAB Report. Tech. rep., von Karman Institute for Fluid Dynamics.

Anderson, J.D., 2003. *Modern Compressible Flow: with Historical Perspective*. McGraw-Hill Education, New-York, third edn.

Anderson, J.D., 2006. *Hypersonic and high-temperature gas dynamics*. American Institute of Aeronautics and Astronautics.

Ansys, Inc., 2021. Ansys Fluent. Last view May 9th, 2021.
URL `https://www.ansys.com/products/fluids/ansys-fluent`

Asma, C.O., 2001. Transition and shock wave-boundary layer interaction in hypersonic flows. Project Report 2001-01, von Karman Institute for Fluid Dynamics.

Asma, C.O., Barbe, F., Paris, S. and Fletcher, D.G., 2002. Comparison of Plexiglas and Vespel Materials for Heat Flux Measurements by Infrared Thermography at Hypersonic Conditions. In *6th International Conference on Quantitative Infrared Thermography*.

Asma, C.O., Thoemel, J., Paris, S., Tirtey, S. and Chazot, O., 2008. Utilization of infrared thermography to investigate atmospheric entry aerothermodynamics of space vehicles at von Karman Institute. In *9th International Conference on Quantitative InfraRed Thermography*, pp. 2–5.

Avallone, F., 2015. *Application of non-intrusive experimental techniques to roughness-induced transition in hypersonic flows*. Ph.D. thesis, Delft University of Technology.

Bertin, J.J., 1994. *Hypersonic aerothermodynamics*. AIAA Education Series, Washington DC, USA.

Bertin, J.J. and Cummings, R.M., 2003. Fifty years of hypersonics: where we've been, where we're going. *Progress in Aerospace Sciences*, **39**(6-7): pp. 511–536.

Billig, F.S., 1967. Shock-wave shapes around spherical- and cylindrical-nosed bodies. *Journal of Spacecraft and Rockets*, **4**(6): pp. 822–823.

Boerrigter, H.L., 1993. Calibration of the H3 wind tunnel using Pitot probes. Internal Note 94, von Karman Institute for Fluid Dynamics.

Boerrigter, H.L., Charbonnier, J.M. and Elbay, M.K., 1993. Application of quantitative infrared thermography to the study of boundary layer transition in hypersonic flow. Preprint 1993-30, von Karman Institute for Fluid Dynamics.

Boison, J.C. and Curtiss, H.A., 1959. An experimental investigation of blunt body stagnation point velocity gradient. *ARS Journal*, **29**(2): pp. 130–135.

Bonfiglioli, A., Paciorri, R. and Di Mascio, A., 2012. The role of mesh generation, adaptation, and refinement on the computation of flows featuring strong shocks. *Modelling and Simulation in Engineering*, **2012**: p. 15.

Brandis, A.M. and Johnston, C.O., 2014. Characterization of stagnation-point heat flux for earth entry. In *45th AIAA Plasmadynamics and Lasers Conference*, p. 2374.

Candler, G.V., 2018. Nonequilibrium hypersonic flows and hypersonic nozzle flow modeling. STO-AVT-352-VKI Lecture Series, von Karman Institute for Fluid Dynamics.

Carlomagno, G.M. and Cardone, G., 2010. Infrared thermography for convective heat transfer measurements. *Experiments in fluids*, **49**(6): pp. 1187–1218.

Carugno, P., 2012. Quantitative infrared measurements for heat-flux determination in hypersonic regime. STP report 2012-37, von Karman Institute for Fluid Dynamics.

Chapman, D.R., 1959. *An approximate analytical method for studying entry into planetary atmospheres*. US Government Printing Office.

Cohen, N.B., 1961. Boundary-layer similar solutions and correlation equations for laminar heat-transfer distribution in equilibrium air at velocities up to 41,100 feet per second. TR R-118, National Aeronautics and Space Administration.

Coleman, H.W. and Steele, W.G., 2018. *Experimentation, validation, and uncertainty analysis for engineers*. John Wiley & Sons.

Cook, W.J. and Felderman, E.J., 1966. Reduction of data from thin-film heat-transfer gages: a concise numerical technique. *AIAA journal*, **4**(3): pp. 561–562.

Cooke, J.C., 1961. An axially symmetric analogue for general three-dimensional boundary layers. R&M No. 3200, British A.R.C.

Crabtree, L.F., Dommett, R.L. and Woodley, J.G., 1970. Estimation of heat transfer to flat plates, cones and blunt bodies. Reports and Memoranda 3637, Aeronautical Research Council.

Daum, F.L. and Gyarmathy, G., 1968. Condensation of air and nitrogen in hypersonic wind tunnels. *AIAA Journal*, **6**(3): pp. 458–465.

DeJarnette, F.R. and Hamilton, H.H., 1973. Inviscid surface streamlines and heat transfer on shuttle-type configurations. *Journal of Spacecraft and Rockets*, **10**(5): pp. 314–321.

DeJarnette, F.R., Hamilton, H.H., Weilmuenster, K.J. and Cheatwood, F.M., 1987. A review of some approximate methods used in aerodynamic heating analyses. *Journal of Thermophysics and Heat Transfer*, **1**(1): pp. 5–12.

Desai, P.S., 2014. *An Analytical Method to Evaluate Laminar Convective Heating Rates for Paraboloids with Perfect Gas Chemistry.* Master's thesis, North Carolina State University.

Dieudonne, W., Boerrigter, H.L. and Charbonnier, J.M., 1997. Hypersonic Flow on a Blunted Cone-Flare and in the VKI-H3 Mach 6 wind tunnel. Tech. rep., von Karman Institute for Fluid Dynamics.

Durbin, T., Grossir, G. and Chazot, O., 2020. Hypersonic aerodynamic predictions for arbitrary geometries using ANTARES. In *HiSST: 2nd International Conference onHigh-Speed Vehicle Science & Technology.*

Eckert, E., 1956. Engineering relations for heat transfer and friction in high-velocity laminar and turbulent boundary-layer flow over surfaces with constant pressure and temperature. *Transactions of the ASME*, **78**(6): pp. 1273–1283.

Elbay, M.K., 1993. Axisymmetric shock wave / boundary layer interaction over conical flared bodies in hypersonic flow. PR 1993-20, von Karman Institute for Fluid Dynamics.

Fay, J.A. and Riddell, F.R., 1958. Theory of stagnation point heat transfer in dissociated air. *Journal of the Aerospace Sciences*, **25**(2): pp. 73–85.

FLIR, 2016. *User's manual FLIR A6xx series.* Available `here.` Last view May 9th, 2021.

French, J.R. and Griffin, M.D., 1991. Space vehicle design. *AIAA Education Series, Washington, DC*, pp. 231–236.

Grossir, G., 2015. *Longshot hypersonic wind tunnel flow characterization and boundary layer stability investigations.* Ph.D. thesis, von Karman Institute for Fluid Dynamics - Université Libre de Bruxelles.

Grossir, G., Masutti, D. and Chazot, O., 2015. Flow characterization and boundary layer transition studies in VKI hypersonic facilities. In *53rd AIAA Aerospace Sciences Meeting*, p. 0578.

Grünberg, T., 2008. The measurement of disturbance levels in the VKI H3 Mach 6 hypersonic wind tunnel. STP report 2008-20, von Karman Institute for Fluid Dynamics.

Hender, D.R., 1970. A Miniature Version of the JA70 Aerodynamic Heating ComputerProgram, H800 (MINIVER). Report MCD G0462, McDonnell-Douglas Astronautics Co.

Higgins, K., 2008. Comparison of engineering correlations for predicting heat transfer in zero-pressure-gradient compressible boundary layers with CFD and experimental data. Tech. rep., Defence Science and Technology Organisation, Victoria (Australia).

Hirsch, C., 2007. *Numerical computation of internal and external flows: The fundamentals of computational fluid dynamics.* Elsevier, second edn.

Hopkins, E.J. and Inouye, M., 1971. An evaluation of theories for predicting turbulent skin friction and heat transfer on flat plates at supersonic and hypersonic Mach numbers. *AIAA Journal*, **9**(6): pp. 993–1003.

Hoshizaki, H., Chou, Y.S., Kulgein, N.G. and Meyer, J.W., 1975. Critical Review of Stagnation Point Heat Transfer Theory. AFFDL-TR-75-85, Lockheed Palo Alto Research Laboratory.

Ilich, Z., Grossir, G. and Chazot, O., 2017. Evaluation of the Stagnation-Point Velocity Gradient in Low-Enthalpy Hypersonic Flows. In *33rd AIAA Aerodynamic Measurement Technology and Ground Testing Conference*, p. 3984. von Karman Institute for Fluid Dynamics.

Incropera, F.P., DeWitt, D.P., Bergman, T.L. and Lavine, A.S., 2012. *Foundations of heat transfer*. Wiley Textbooks.

dello Ioio, G., 2008. *An improved data reduction technique for heat transfer measurements in hypersonic flows*. Ph.D. thesis, Universit Federico II, Naples, Italy.

Juliano, T.J., Paquin, L.A. and Borg, M.P., 2019. HIFiRE-5 boundary-layer transition measured in a Mach-6 quiet tunnel with infrared thermography. *AIAA Journal*, **57**(5): pp. 2001–2010.

Kemp, N.H., Rose, P.H. and Detra, R.W., 1959. Laminar heat transfer around blunt bodies in dissociated air. *Journal of Aeronautical Sciences*, **26**(7): pp. 421–430.

Kinney, D., 2004. Aero-thermodynamics for conceptual design. In *42nd AIAA Aerospace Sciences Meeting and Exhibit*, p. 31.

Kinney, D., Garcia, J. and Huynh, L., 2006. Predicted convective and radiative aerothermodynamic environments for various reentry vehicles using CBAERO. In *44th AIAA Aerospace Sciences Meeting and Exhibit*, p. 659.

Knight, D., Chazot, O., Austin, J., Badr, M.A., Candler, G., Celik, B., de Rosa, D., Donelli, R., Komives, J., Lani, A., Levin, D., Nompelis, I., Panesi, M., Pezzella, G., Reimann, B., Tumuklu, O. and Yuceil, K., 2017. Assessment of predictive capabilities for aerodynamic heating in hypersonic flow. *Progress in Aerospace Sciences*, **90**: pp. 39–53.

Koppenwallner, G., 1984. Fundamentals of hypersonics: aerodynamics and heat transfer. In *Hypersonic aerothermodynamics*, VKI Lecture Series 1984-01. von Karman Institute for Fluid Dynamics.

Kordulla, W., 1970. Calibration of the hypersonic wind tunnel H3. Project Report 70-264, von Karman Insitute for Fluid Dynamics.

Kovács, D.G., 2018. Development of a coaxial thermocouple and its calibration method. STP report 2019-07, von Karman Institute for Fluid Dynamics.

Laufer, J., 1961. Aerodynamic noise in supersonic wind tunnels. *Journal of the Aerospace Sciences*, **28**(9): pp. 685–692.

Lees, L., 1956. Laminar heat transfer over blunt-nosed bodies at hypersonic flight speeds. *Jet Propulsion*, **26**(4): pp. 259–269.

Lees, L., 1955. Hypersonic flow. In *Fifth International Aeronautical Conference*, pp. 241–276. Institute of Aeronautical Sciences, Los Angeles.

Liang, Z., Zhi, C., Jian, G. and Xuejun, Z., 2015. Effects of Nose and Corner Radius on Heat Transfer Rates over Axisymmetric Blunt Body. *Procedia Engineering*, **99**: pp. 428–432.

Mack, L.M., 1984. Boundary layer linear stability theory. In *Special course on stability and transition of laminar flows*, AGARD Report 709. NATO.

Martinelli, S.K. and Braun, R., 2010. Centerline Heating Methodology for use in Preliminary-Design Studies. Tech. rep., Georgia Institute of Technology, Atlanta, Georgia, 30313.

Masutti, D., 2013. *Ground Testing Investigationof Hypersonic Transition Phenomenafor a Re-Entry Vehicle*. Ph.D. thesis, von Karman Institutefor Fluid Dynamics - Technische Universiteit Delft.

Masutti, D., Spinosa, E., Chazot, O. and Carbonaro, M., 2012. Disturbance level characterization of a hypersonic blowdown facility. *AIAA journal*, **50**(12): pp. 2720–2730.

MathWorks, Inc., 2021. Matlab. Last view May 9th, 2021.
URL `https://nl.mathworks.com/products/matlab.html`

Metacomp Technologies, Inc., 2021. CFD++. Last view May 9th, 2021.
URL `https://www.metacomptech.com/index.php/features/icfd`

Miró Miró, F., 2020. Boundary-Layer Stability and Transition. Technical Memorandum 58, von Karman Institute for Fluid Dynamics.

Morkovin, M.V., 1994. Transition in open flow systems - a reassessment. *Bulletin of the American Physical Society*, **39**(9): p. 1882.

National Institute of Standards and Technology, 2018. NIST ITS-90 Thermocouple Database. Last view May 9th, 2021.
URL `https://srdata.nist.gov/its90/main/`

National Instruments, Inc., 2015. *NI 9211 Data sheet*. Available `here.` Last view May 9th, 2021.

National Instruments, Inc., 2021. LabVIEW official website. Last view May 9th, 2021.
URL `https://www.ni.com/fr-be/shop/labview.html`

Noori, S., Hossein, S.A. and Ebrahimi, M., 2012. An approximate engineering method for aerodynamic heating solution around blunt body nose. *International Journal of Aerospace and Mechanical Engineering*, **6**(10): pp. 2221–2225.

Olivier, H., 1993. An improved method to determine free stream conditions in hypersonic facilities. *Shock Waves*, **3**(2): pp. 129–139.

Pate, S.R., 1978. Dominance of Radiated Aerodynamic Noise on Boundary-Layer Transition in Supersonic-Hypersonic Wind Tunnels. Technical report AEDC-TR-77, Arnold Engineering Development Center.

Playez, M., 1997. Transient heat flux identification over models with 3D heat conduction from infrared measurement. Project Report 1999-27, von Karman Institute for Fluid Dynamics.

Reshotko, E., 2007. Is Re_θ/M_e a Meaningful Transition Criterion? *AIAA journal*, **45**(7): pp. 1441–1443.

Richards, B.E., 1979. Kinetic heating of high-speed missiles. Preprint 1979-5, von Karman Institute for Fluid Dynamics.

Riley, C.J., DeJarnette, F.R. and Zoby, E.V., 1990. Surface pressure and streamline effects on laminar heating calculations. *Journal of Spacecraft and Rockets*, **27**(1): pp. 9–14.

Rotta, N.R., 1966. Effects of nose bluntness on the boundary layer characteristics of conical bodies at hypersonic speeds. Tech. Rep. NYU-AA-66-66, New York University.

Running, C.L., Juliano, T.J., Jewell, J.S., Borg, M.P. and Kimmel, R.L., 2019. Hypersonic shock-wave/boundary-layer interactions on a cone/flare. *Experimental Thermal and Fluid Science*, **109**: p. 109911.

Sagnier, P. and Verant, J.L., 1998. Flow characterization in the ONERA F4 high-enthalpy wind tunnel. *AIAA journal*, **36**(4): pp. 522–531.

Sakraker, I., 2016. *Aerothermodynamics of pre-flight and in-flight testing methodologies for atmospheric entry probes*. Ph.D. thesis, Université de Liège, Belgium.

Santarelli, P. and Charbonnier, J.M., 1999. Heat transfer data reduction user guide for the VKI-H3 wind tunnel. Internal Note 115, von Karman Institute for Fluid Dynamics.

Saravanan, S., Jagadeesh, G. and Reddy, K.P.J., 2009. Convective heat-transfer rate distribution over a missile shaped body flying at hypersonic speeds. *Experimental Thermal and Fluid Science*, **33**(4): pp. 782–790.

Schneider, S.P., 2008. Development of hypersonic quiet tunnels. *Journal of Spacecraft and Rockets*, **45**(4): pp. 641–664.

Schultz, D.L. and Jones, T.V., 1973. Heat-Transfer Measurements in Short-Duration Hypersonic Facilities. Tech. rep., Advisory group for Aerospace Research and Development, Paris, France.

Silvestri, D.F., 2003. Acoustic influence on transition in the VKI H3 hypersonic wind tunnel. Project Report 2003-11, von Karman Institute for Fluid Dynamics.

Simeonides, G., 1990. The VKI hypersonic wind tunnels and associated measurement techniques. Technical Memorandum 46, von Karman Institute for Fluid Dynamics.

Simeonides, G., Vermeulen, J.P., Boerrigter, H.L. and Wendt, J.F., 1993. Quantitative heat transfer measurements in hypersonic wind tunnels by means of infrared thermography. *IEEE Transactions on Aerospace and Electronic Systems*, **29**(3): pp. 878–893.

Smith, A.M.O. and Gamberoni, N., 1956. Transition, pressure gradient andstability theory. Tech. Rep. ES-26388, Douglas Aircraft Co., El Segundo, California.

Spinosa, E., 2010. Experimental characterization of the freestream disturbance level of the VKI H-3 wind tunnel. Project Report 2010-32, von Karman Institute for Fluid Dynamics.

Stetson, K.F., 1987. On predicting hypersonic boundary layer transition. Technical Memorandum AFWAL-TM-87-160-FIMG, Air Force WrightAeronautical Laboratories.

Strub, A., 2006. Roughness induced transition in hypersonic boundary layer flows. STP report 2006-08, von Karman Institute for Fluid Dynamics.

Sutton, K. and Graves, R.A., 1971. A general stagnation-point convective-heating equation for arbitrary gas mixtures. NASA TR R-376, NASA Langley Research Center.

Tauber, M.E., 1989. A review of high-speed, convective, heat-transfer computation methods. NASA Technical paper 2914, Ames Research Center.

Tauber, M.E., Menees, G.P. and Adelman, H.G., 1987. Aerothermodynamics of transatmospheric vehicles. *Journal of Aircraft*, **24**(9): pp. 594–602.

Tecplot, Inc., 2021. Tecplot 360. Last view May 9th, 2021.
URL `https://www.tecplot.com/products/tecplot-360/`

van den Abbeele, W., 1996. Unsteady pressure measurements on a flat plate at Mach 6. Project Report 1996-28, von Karman Institute for Fluid Dynamics.

van Driest, E.R., 1956. The problem of aerodynamic heating. *Aeronautical Engineering Review*, **15**(10): pp. 26–41.

van Dyke, M.D., 1958. The supersonic blunt-body problem: review and extension. *Journal of the Aerospace Sciences*, **25**(8): pp. 485–496.

van Ingen, J., 1956. A suggested semi-empirical method for the calculation of the boundary layer transition region. Tech. Rep. V.T.H.-74, Technische Hogeschool Delft, Vliegtuigbouwkunde.

Vanhée, J.L., 1988. Feasability of heat transfer measurements in hypersonic wind tunnels using infrared thermography. Project Report 1988-30, von Karman Institute for Fluid Dynamics.

Vanhée, J.L., 1989. The H3 hypersonic wind tunnel: new implementation and calibration. Internal Note 86, von Karman Institute for Fluid Dynamics.

Wen, C., 1994. *Hypervelocity flow over spheres*. Ph.D. thesis, California Institute of Technology.

White, F.M., 2006. *Viscous Fluid Flow*, vol. 3. McGraw-Hill.

WIKA, 2014. *Pressure transducer model S-20 data sheet*. Available `here.` Last view May 9th, 2021.

Yang, W.J., 2001. *Handbook of Flow Visualization*. Routledge, second edn.

Zoby, E.V. and Simmonds, A.L., 1985. Engineering flowfield method with angle-of-attack applications. *Journal of spacecraft and rockets*, **22**(4): pp. 398–404.

Zoby, E., Moss, J. and Sutton, K., 1981. Approximate convective-heating equations for hypersonic flows. *Journal of Spacecraft and Rockets*, **18**(1): pp. 64–70.